Ultra-Wideband Phased Array Radar for Short-Range Imaging Applications

Pei-Yu Chao

A thesis submitted to the Department of Electrical Engineering,
University of Cape Town, in fulfillment of the requirements
for the degree of Master of Science in Engineering.

Cape Town, June 2009

Contents

List of Figures

List of Tables

List of Symbols

B	—	Signal bandwidth
B_{eff}	—	Effective bandwidth
$B_{instant}$	—	Instantaneous bandwidth
c	—	Speed of electromagnetic propagation within the sensing medium
ε_0	—	Permittivity of free space
ε_r	—	Relative dielectric constant
θ	—	Azimuth angle
f_H	—	Highest frequency component
f_L	—	Lowest frequency component
f_s	—	Effective sampling frequency of the receiver
f_t	—	Transmitted frequency
$f_{Nyquist}$	—	Nyquist sampling frequency
f_{PRF}	—	Pulse repetition frequency
Δf	—	Frequency step size
λ	—	Wavelength
R	—	Range of interest
R_{max}	—	Maximum unambiguous range
ΔR	—	Range Resolution
Δt	–	Step size of delay line
t_{bin}	—	Integrating time for a range bin
t_{PRI}	—	Pulse repetition interval
τ_{pulse}	—	Pulse width
τ_{delay}	—	Delay Time
τ	—	Pulse duration
Z_0	—	Characteristic impedance
ζ	—	Impulse response of the scene

Nomenclature

ADC—Analog to digital converter.

AGC—Automatic gain control.

DAC—Digital to analog converter.

DSO—Digital storage oscilloscope.

Fractional bandwidth—A ratio between the bandwidth and centre frequency of a signal. It is defined as $\frac{2(f_H - f_L)}{(f_H + f_L)}$.

HF—High frequency.

LF—Low frequency.

IDC—Interdigital capacitor.

LNA—Low noise amplifier.

NDE—Non-destructive evaluation system.

PA—Power amplifier.

PLL—Phase-locked loop.

PRF—Pulse repetition frequency.

PRI—Pulse repetition interval.

PSD—Power spectral density.

RF—Radio frequency.

SNR—Signal-to-noise ratio. A ratio between the signal power and the variance of the noise.

Ultra-wideband(UWB)—A term to describe a signal or a system whose fractional bandwidth is ≥ 0.2 or the total bandwidth is $\geq$500 MHz.

uC—Micro-controller.

uP—Micro-processor.

Chapter 1

Introduction

1.1 Introduction to Ultra-Wideband Radar

Ultra-wideband (UWB) technology, as defined by the Federal Communication Commission (FCC) on February 2002, refers to signals or systems that have bandwidth $\geq$ 500 MHz or instantaneous fractional bandwidth ≥ 0.20 [2]. Compared to the conventional narrowband radar that operates with the same centre frequency, UWB radar offers many advantages, including high spatial resolution, for detecting closely-spaced target; and lower probability of interception, for stealth-like military application [36].

There are many types of UWB waveform. The most obvious and simplest-to-generate UWB waveform is the impulse or short pulse [25]. The pulse width of these impulses is usually sub-nanosecond, which enable a range resolution of 15 cm or less, when it is being transmitted in free space.

A UWB impulse system can be designed as such that it transmits, receives and samples the RF signal directly. This approach eliminates the use of components such as high quality oscillators, mixers and tuned circuits that are commonly used by narrowband systems to modulate a high frequency RF carrier wave to transmit and receive information [32]. However, if the conventional receiver design is to be used, the receiver will require a high speed sampling architecture, in order to sample large bandwidth signals [19]. Therefore, a programmable delay line receiver design is proposed and implemented to overcome this issue, which will be discussed in the later chapter. Consequently, the complexity and cost of the proposed UWB system hardware is significantly reduced when compared to the conventional narrowband system.

A UWB impulse system not only has an advantage of simple and low cost hardware design, the signal itself has a wide frequency spectrum compared to the narrowband signal with the same centre frequency. A bandlimited impulse signal (in practice, the antenna used to transmit and receive the impulse signal tends to bandlimit the signal) with a pulse

width of 0.5 ns, has frequency components that cover from low frequency (close to DC) to high frequency (3 dB point at approximately 2 GHz). The lower spectral components tend to penetrate through various materials more efficiently than the high spectral components. However, the higher spectral components can utilize smaller antenna designs. Although there is a trade-off between the size of the radar system and the efficiency in detecting target through obstructions, the overall system performance for through-wall detection has been found satisfying. There are number of UWB impulse array systems available commercially for through-wall imaging. These UWB array system can be used to create an image behind a wall, which is a great tool for firefighters looking for people trapped in a smoke-filled building..

UWB radar was used initially in military applications [36, 53], as the range resolution is much shorter than the length of typical military target, e.g. aircraft and missile. The fine range resolution enhances the accuracy in locating and recognizing of the targets. Nowadays, UWB radar can be found in many other commercial applications, such as ground penetrating radar and medical imaging radar.

1.2 Background

The fundamental advantage of using a wide bandwidth radar is it offers fine range resolution, which enhances the information concerning the location and characteristics of the target. In order to obtain high range resolution, the absolute bandwidth, which is the signal bandwidth, need to be wide; whereas the fractional bandwidth, which is defined as the absolute bandwidth divided by its centre frequency, is not necessary wide [27]. However, when an application requires a system that operates in a relatively low centre frequency and has wide bandwidth of several hundred MHz, a UWB system is required.

A previous MSc student from University of Cape Town, Mr. A. Chang, has built a single-channel UWB impulse radar for short-range application based on the designs found in [30, 39, 50, 51, 52]. This UWB radar system consists of radar circuitry, the data-acquisition subsystem, the signal processing subsystem and the graphical user interface (GUI) [57]. Based on the results shown in [57], it was concluded that the system was not sensitive enough to detect objects through brick walls, due to certain deficiencies in its circuits. Furthermore, the system was not portable, as it used a PCI data acquisition card with a mains powered PC. Hence, improvements on the UWB impulse system, such as the circuit design and system integration, are necessary before forming an array system.

1.3 Objectives

The objectives of this thesis are:

1. Revise the existing single-channel UWB radar [57], which was constructed by a previous MSc student from University of Cape Town. This revision is aimed at improving the system performance in terms of stability, portability and signal strength.
2. Use the revised circuits to build a multi-channel UWB phased array radar.
3. Design and implement an graphical-user-interface (GUI) using the Python programming language. This GUI should enable the user to
   (a) Initiate data acquisition.
   (b) Process the raw data to form a down-range profile and later, a beamformed image.
4. Explore the potential of the system for through-wall imaging.

1.4 Limitations and scope of thesis

The scope of this thesis is to improve the existing UWB radar in terms of signal strength, stability and portability. Hence, the original circuit design for the pulse generator and the UWB receiver will be revised and modified. In terms of system integration, usage of a microcontroller and construction of a user-interface are required to control the radar system, performing operations such as initiating data acquisition.

A printed circuit board prototype of the pulse generator and the UWB receivers will be used to formed a proof-of-principle UWB impulse array system. Experiments will be carried out to demonstrate the performance and capability of this array system. These experiments will be used to justify the improvements made on the circuit design, as well as the capability of the radar system for detecting the presence and the movement of the target.

Due to the time availability for this thesis, several aspects of this UWB phased array system have not been investigated thoroughly or have had to be compromised. These aspects should be considered as topics for future research:

- Designing UWB antenna for the phased array system. The broad-band antennas used in this thesis were 'off the shelf' L-band antennas that were available in the department at the time.
- The image update rate was limited by the serial RS-232 data transmission interface between the microcontroller data acquisition board and the PC. The usage of a USB interface is recommended for future work.

- UWB beamforming is another extensive field of knowledge, which have not been investigated fully in this thesis. This thesis merely noted on the differences between the properties of conventional and UWB beamforming. There are no simlated results that were generated in this thesis to prove those differences, e.g. difference in the beampattern of UWB and conventional narrowband phased array.

1.5 Thesis Outline

This thesis is organized into the following sections:

- Chapter 2 is a literature review on UWB technology, which briefly describes different types of UWB waveform, the historical background on UWB technology, the UWB impulse array system and UWB applications in radar .
- Chapter 3 presents an overview of the UWB radar system. This overview includes the design specification for this thesis, which is then followed by a discussion on the UWB radar operation. Lastly, a discussion on the necessary signal processing techniques required to process the received raw data is presented.
- Chapter 4 investigates the design of the pulse generator. The limitations from the previous designs are analyzed and improvements made in this thesis, are discussed in this chapter.
- Chapter 5 introduces the receiver circuitry required for the UWB radar. The receiver circuit is separated into modules. A detailed analysis on the receiver circuit will be presented in this chapter.
- Chapter 6 describes the simulation of the UWB phased array radar system.
- Chapter 7 presents and analyzes the system performance and various target detection results under different testing conditions.
- Chapter 8 concludes this thesis and recommendations for future research are made.

Chapter 2

Literature Review

A narrowband system is defined as a system with fractional bandwidth ≤ 0.01 [32]. One of the common ways to transmit and receive information in a narrowband system, is to modulate the signal to a higher frequency by mixing the signal with a high frequency RF carrier signal [32]. Since a narrowband system only operates within a specific frequency band, a large number of narrowband systems, which operate at different frequency bands, can co-exist in a common environment without interfering with each other. Hence, most conventional radars are bandlimited narrowband systems.

Ultra-wideband (UWB) technology, as defined by the Federal Communications Commission (FCC), refers to signals or systems that have bandwidth ≥ 500 MHz or instantaneous fractional bandwidth ≥ 0.20 [2]. Compared to the narrowband radar that operates with the same centre frequency, UWB radar offers finer range resolution. For example, a narrowband system, centred on 1.5 GHz, that has a bandwidth of 15 MHz (equivalent to a fractional bandwidth of 0.01) has a range resolution of 10 m; whereas a UWB system, also centred on 1.5 GHz, that has a bandwidth of 300 MHz (equivalent to a fractional bandwidth of 0.2) has a range resolution of 0.50 m. With finer range resolution, UWB system is able to reduce the amount of clutter within the resolution cell, resolve closely-spaced targets in range, and provide high-resolution range profile, which enhances in locating and classifying the targets [37].

Figure 2.1 shows a comparison between a typical narrowband and a UWB impulse transceiver architecture and Table 2.1 compares each module of both transceivers in detail [26].

A UWB impulse system directly transmits, receives and processes the RF signal, which eliminates the usage of components such as high quality oscillators and tuned circuits. This significantly reduces the complexity and cost of the system hardware. However, UWB receivers require a more complex sampling architecture, as a high sampling rate is required for sampling large bandwidth signals [19].

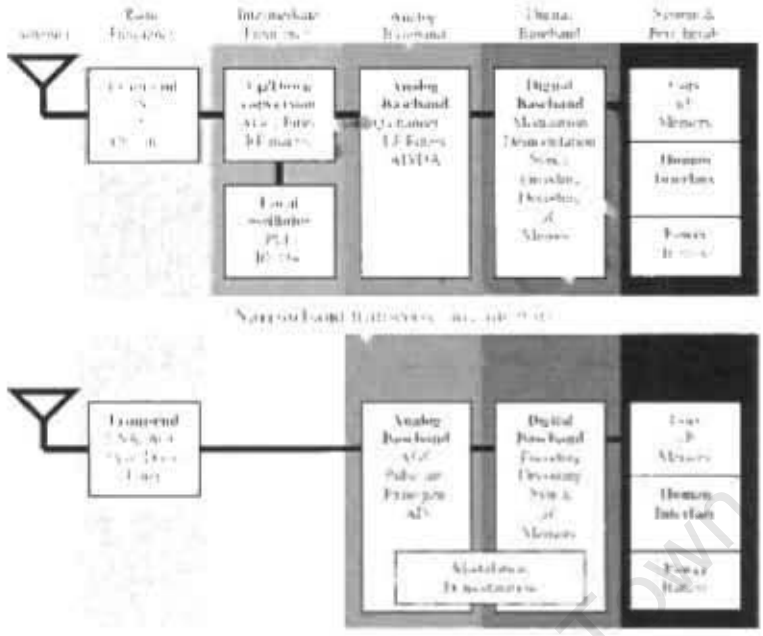

Figure 2.1: Comparison between narrowband and UWB transceiver architecture [26].

	Narrowband	Ultra-wideband
Antenna	Good gain response is easily achievable over the operating bandwidth	Good gain response is difficult to achieve over the operating bandwidth.
Front-end amplifier	Commercial-off-the-shelf narrowband LNA are easy to match	Commercial-off-the-shelf wideband LNA are power consuming and hard to match.
Intermediate frequency	Requires RF mixers and RF oscillator.	No need.
Analog baseband	High frequency narrowband signal is often translated to a lower frequency via heterodyning before it is digitized. Hence, the narrowband receiver only requires ADC with moderate resolution and bandwidth.	Requires a relatively high bandwidth ADC or sampling with channelized receiver.
Digital baseband	Non-coherent detection (in terms of time reference accuracy).	Coherent detection with precise time references is required.

Table 2.1: Comparison between narrowband and UWB transceiver design. The comparison is done under an assumption that both transceiver operated on same centre frequency (1.5 GHz) [26].

Another key advantage of a UWB system is that it offers lower probability of interception. UWB signals have a lower PSD (power spectral density) than a narrowband system radiating the same average power. The PSD of a UWB signal looks like that of Gaussian distributed noise to most narrowband detection systems [37, 43].

The rest of this chapter will present a literature review on UWB systems, including an introduction to different types of UWB waveform and a brief description on the past work on UWB impulse radar system. A discussion on the UWB impulse array system will be present, which is then followed by its applications in the industry. Lastly, an analysis on the system performance of the existing signal-channel UWB radar at the University of Cape Town will be present.

2.1 Ultra-Wideband Waveforms

UWB waveforms can be divided into three main categories: impulse, linear frequency modulation and step-frequency waveform. Although the effective bandwidth is achieved differently with different type of waveform, the range resolution ΔR, for all three categories is given by

$$\Delta R \approx \frac{c}{2B_{eff}}$$

where B_{eff} is the effective bandwidth and c is the speed of electromagnetic propagation within the sensing medium [37].

2.1.1 Impulse (Short Pulse)

An impulse signal, which is a pulse with pulse width typically less than 1 ns [25], as shown in Figure 2.2(a), has a 3 dB bandwidth B of

$$B \approx \frac{1}{2\tau}$$

where τ is the pulse duration. However, in practice, the antenna used to transmit and receive the impulse signal tends to bandlimit the signal. Hence, the 3 dB bandwidth B of a bandlimited impulse signal, as shown in Figure 2.2(b), is determined as

$$B \approx \frac{1}{\tau}$$

A bandlimited sub-nanosecond impulse has spectrum components from close-to-DC to several GHz. Hence, large effective bandwidth, which implies high range resolution, can be achieved with a single impulse.

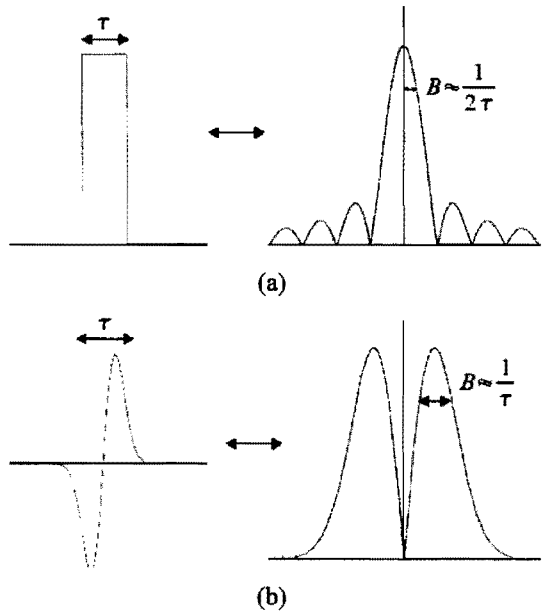

Figure 2.2: Plots illustrate 3 dB bandwidth of (a) an impulse signal and (b) a bandlimited impulse signal.

Another advantage of using an impulse signal is that it provides an accurate time delay estimate between the target and the radar system. This is done by measuring the time elapsed between transmitted and received signal. This time delay is dependent on the range of the target [19], i.e.

$$\tau_{delay} = \frac{2R}{c}$$

where R is the distance between the target and the radar system.

The hardware design of an impulse generator is relatively simple and low cost if only a moderate signal power is required. However, the pulse energy is relatively low as the pulse length of an impulse is very short, i.e. typically sub-nanosecond. This sets a limitation on the system performance in terms of maximum range for detection, especially when it is used to detect a human target.

Another issue with using impulse waveform is that an analog-to-digital converter with a high sampling rate is required for digitizing the received impulse echo, if the conventional receiver design is to use. High bandwidth and high resolution ADCs are expensive. Hence, researches have been conducted to investigate suitable low cost design for UWB impulse receiver [51, 52].

2.1.2 Chirp (Linear Frequency Modulation)

The linear frequency modulated, or linear FM chirp, is widely used in high-resolution radar applications [25, 37]. A linear FM chirp waveform is a sine wave in which the fre-

quency increases or decreases with time. Figure 2.3 shows the time and frequency domain of a 100-400 MHz chirp with a chirp length of 1 μs.

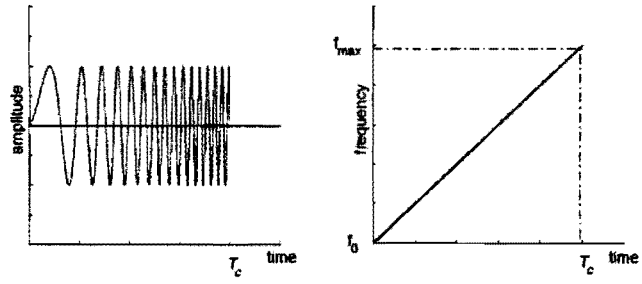

(a) Time (left) and time-frequency (right) domain

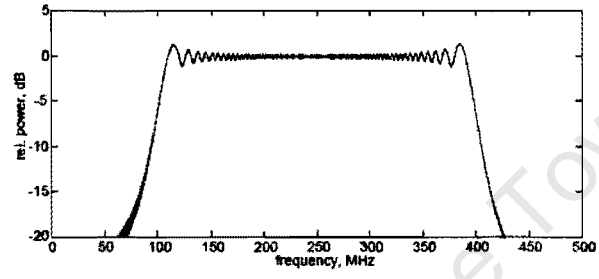

(b) Frequency domain of a 100-400 MHz chirp signal

Figure 2.3: Chirp signal in (a) time domain and (b) frequency domain [25].

A chirp waveform attaines large bandwidth by increasing its frequency with time, instead of by decreasing its signal length. This has an advantage of increase the signal energy while maintaining the high resolution of a radar [25].

2.1.3 Step-Frequency Waveform

A step-frequency waveform is a sequence of coherent pulses whose frequencies are increased from pulse to pulse by a fixed frequency increment Δf [37]. Figure 2.4 illustrates a step-frequency waveform.

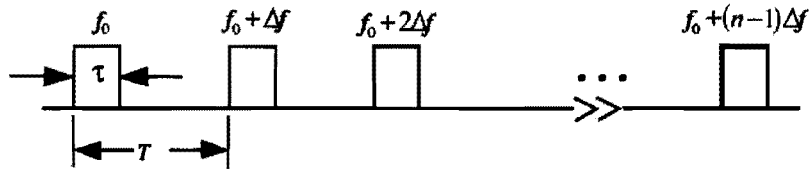

Figure 2.4: A step-frequency waveform, which consists of a group of pulses with pulse width τ and spaced in T second. The frequency of the pulses is increased linearly by Δf hertz [37].

The pulses in a step-frequency waveform have same pulse width. Pulses used to construct step-frequency signal is typically narrow in bandwidth. Hence, narrowband equipment

(except for the antenna and transmitter) can be used to implement step-frequency radar [37].

As mentioned at the start of this section, the range resolution is determined by the effective bandwidth of the waveform. The effective bandwidth of a step-frequency waveform is given by

$$B_{eff} = N\Delta f$$

where N is the number of pulses in the waveform. Hence, large effective bandwidth can be achieved by increasing the number of pulses in the waveform.

Since each pulse situated in a different band of frequency spectrum, the radar receiving echoes are usually recorded separately for the different bands. The recorded data is then combined and reconstructed to form a larger portion of the scene spectrum. However, if not designed properly, i.e. $B_{instant} < \Delta f$, where $B_{instant}$ is the instantaneous bandwidth of the step-frequency signal, the processed data will contain gaps in the spectrum, and possibly yielding ghosting artifacts [56]. Hence, researches have been conducted to investigate methods to process step-frequency waveforms to reduce these artifacts [23].

2.2 Past Work in UWB Impulse Radar

UWB technology can be dated back into the late 1800s, as Hertz generated a short electromagnetic pulse using a spark-gap generator [24]. Later in 1901, Guglielmo Marconi developed the first spark-gap radio, which he used it to transmit Morse code sequences [32]. However, at the beginning of 1900s, the idea of a large number of radio links, where each operate at a specific frequency, sharing a frequency spectrum, become popular in the communication and radar industry. Hence, narrowband systems were widely adopted [37]. By 1924, spark-gap radios were forbidden in most applications due to their unregulated RF emissions that were disruptive to narrow-band radios [19].

However, the low signal bandwidth limits the ability in radar applications to detect closely spaced targets. Hence in 1960s, UWB impulse systems were revived, with the pioneering contribution of Harmuth, from Catholic University of America, who did much of the important early theoretical work in non-sinusoidal impulse technology; Ross and Robbins, from Sperry Rand Corporation; Paul van Etten, from the US Air Force's (USAF) Rome Air Development Center; and Russian investigators [37, 53, 54].

These pioneers investigated the UWB applications in communication and radar, and the basic design for UWB impulse system, including the transmitter, receiver and antennas, were developed [53]. Table 2.2 summarizes the major milestones in UWB impulse system

development after early 1960s.

Year	Milestone
Late 1960s	The development of commercial sample and hold receiver (Tektronix Inc.). This receiver architecture uses a sampling circuit with a short term integrator. This approach enables UWB signal averaging, which lower the requirement of the receiver's sampling rate for a UWB signal.
1974	UWB ground penetrating radar (GPR) system is developed by Morey, which is commercialized Geophysical Survey Systems, Inc. (GSSI)
Early 1970s	The development in avalanche transistor & tunnel diode detector
1994	T.E. McEwan, at Lawrence Livermore National Laboratory (LLNL), invented the Micropower Impulse Radar (MIR). This is the first UWB radar to operate on microwatts power, and the system offers extremely sensitive signal detection. This technology have been licensed for various commercial applications. The MIR devices are estimated to cost about $10 in sufficient production quantities.

Table 2.2: Milestones in UWB system development [53, 55, 37].

2.3 Ultra-Wideband Impulse Array System

A single channel UWB impulse radar can offer high-resolution range profile and resolve closely-spaced targets in range. However, it does not provide angular information of the target location. In order to obtain an image of the scene, an array system is required. In addition of using an array system, the signal-to-noise ratio (SNR) of an impulse system can be increased. A N-element array system can increase the SNR of a single-element system by N factor.

A UWB impulse array system for 2-D imaging, usually consist of a pulse transmitter and N elements of receiver. A UWB array system has several advantages over a narrowband array system, such as high range resolution, grating lobe cancellation, permitting the design of sparse array and inter-element coupling reduction [40].

In conventional narrowband array system, the inter-element spacing is constrained to be less than half of wavelength to avoid spatial aliasing, i.e. grating lobe effect (refer to Section 3.4.3). This creates a practical limit in the size of the antenna aperture of conventional phased arrays. The size of the aperture affects the angular resolution of the array. Hence, high angular resolution narrowband phased array system usually consists of large number of array elements, which is not a cost-effective solution for some application. Furthermore, as the inter-element spacing decreases, the inter-element coupling effect increases [41]. The effect of coupling consists of distortion in the main part of the direct signal or, more often, in the addition of extra-ringing in the signal tail [41].

Researchers [33, 45] have shown that grating lobes are suppressed in UWB impulse array beamforming. A brief explanation and illustration is presented in Section 3.4.3. This unique property of UWB impulse array allows sparse array design and achieves high angular resolution with only a few array elements.

In terms of inter-element coupling, studies [40, 41] have shown that the coupling phenomena in UWB arrays is less effective than in the case of narrowband arrays, and the phenomena is negligible when the UWB arrays are configured in a sparse array formation.

Recently, UWB impulses array systems have been proposed for many applications, including communications, radar, remote sensing and indoor positioning [40].

2.4 Applications of UWB Impulse Array in Radar

In recent years, UWB radars have become very popular for military and medical application. UWB impulse systems are mainly used for short-range target locating and imaging applications. Vehicle collision-avoidance radar is a well known commercial UWB target locating system [34, 47]. There are many imaging systems that use UWB impulse technology. Two types of UWB imaging applications that will be discuss in this section are non-destructive evaluation systems and through-wall imaging systems.

2.4.1 Non-Destructive Evaluation

Non-destructive evaluation (NDE) systems are used to evaluate the condition and the property of a material, such as walls, roads and bridge decks [35]. The ability to detect and assess the condition of the structure is important to decide whether to repair or to replace the current structure. Ground penetrating radar is a form of NDE. Figure 2.5 shows an experiment setup for a ground penetrating imaging radar (GPIR), which is developed by Lawrence Livermore National Laboratory used to evaluate the structure of bridge decks [35].

Figure 2.5 shows a UWB impulse radar system, which is mounted on top of a test bed. The test bed is made of a concrete slab that contains reinforcing bars. By moving the radar system over the test bed, it simulates the motion of an inspection vehicle, with a fixed linear array of receiving antennas, over a bridge deck [35].

This system used step-recovery diodes to generate the UWB pulse. This pulse generator can generate pulses with peak power at least of 100 W, with pulse width of 100 to 300 ps. The bandwidth of this signal is approximately 8 GHz. The pulse repetition frequency is

Figure 2.5: A experiment setup for a ground-penetrating imaging radar (GPIR) [35].

set up to 5 MHz.

2.4.2 Through-Wall Imaging

Through-wall imaging systems are a relatively new application for UWB technology. They can be used to observe the layout and motion inside a building. Through-wall imaging can be used by police and firefighters to locate the people inside a building, in the case of a hostage crisis or a fire accident [29].

Two commercially available through-wall imaging system are found, namely Xaver™ system by Camero, Inc. [5], shown in Figure 2.6(a), and Prism 200 by Cambridge Consultants Ltd [6], shown in Figure 2.6(b). Both systems can see through most commonly used wall materials, such as brick, concrete, wood and stone. Table 2.3 compares these two systems in terms of physical structure and the system design.

(a) (b)

Figure 2.6: (a) Xaver™ 800 by Camero, Inc. [5] and (b) Prism 200 by Cambridge Consultants Ltd [6].

	Xaver™ 800	Prism 200
Imaging	2-dimensional and 3-dimensional	2-dimensional and 3-dimensional
maximum detection range	20 m for 2-dimensional imaging and 8 m for 3-dimensional imaging	20 m
Weight	15 kg (including batteries)	5.7 kg (including battery)
Size	84 cm × 84 cm × 15 cm	21 cm × 30 cm × 45 cm
Power	(1) Rechargeable batteries (2) Mains power source.	Lithium-ion battery pack
field of view	80° in both azimuth and elevation	120° in azimuth and 90° in elevation.
System PRF	Not specified.	100 Hz
Frequency range	3GHz to 10GHz	1.7 GHz to 2.2 GHz
Range resolution	Less than 0.2 m.	30 cm

Table 2.3. Comparing Xaver™ 800 and Prism 200 through-wall imaging system. [5, 6].

2.5 Existing Signal-Channel UWB radar at University of Cape Town

A previous MSc student from University of Cape Town, Mr. A. Chang, designed and built a single-channel UWB impulse radar for short-range application. This UWB radar system consists of radar circuitry, the data-acquisition subsystem, the signal processing subsystem and the graphical user interface [57].

Part of this thesis's objective is to revise and identify the deficiencies of this system and hence, improve the system performance. The detailed analysis on the transceiver circuit design, i.e. the pulse generator and UWB receiver, will be presented in Chapter 4 and Chapter 5 respectively. The main focus of this section is to analyze the system performance for this single-channel UWB radar system. Figure 2.7 shows the system layout and Figure 2.8 shows the radar circuit board of this radar system.

During the radar operation, the pulse generator is triggered by the square wave, which is generated by the pulse train generator. The receiving signal is sampled by the fast sampler, as shown in Figure 2.7. The fast sampler is triggered by the delayed pulse, which is generated by the pulse train generator and passed through a delay line. The delay is set by the delay line, which each time delay corresponds to a particular range from the radar. The delay is set to be unchanged for a number of pulses, therefore the sampler will sample the return echo at a time delay for a number of times. An integrator is used to integrate the sampled echo. By increasing the delay time generated by the delay line, it is effectively sampling the receiving signal at various ranges from the radar. Hence, a range profile can be obtained.

Following are the system parameters

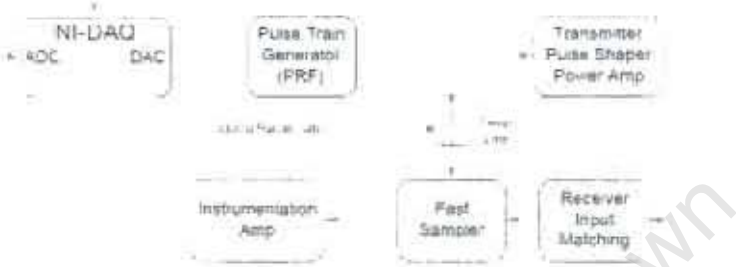

Figure 2.7: Mono-static radar architecture used by [57].

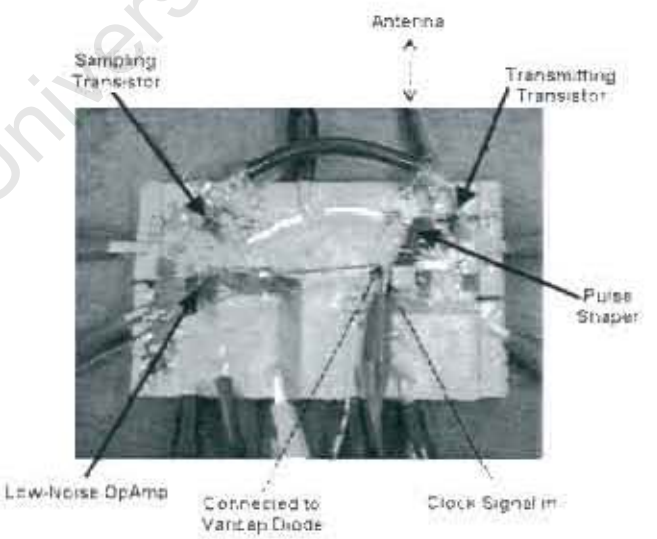

Figure 2.8: Single-channel UWB impulse radar prototype [57].

- The pulse-repetition-rate (PRF) of the pulse generator = 2.0 MHz
- The measured peak voltage of the transmitted pulse ≈ 1.2 V
- The calculated processed bandwidth ≈ 917 MHz (without application of Hanning window).
- The calculated range resolution is $\delta R \approx 0.16$ m.

Experiments were carried out using two bow-tie antennas which operate between 1 GHz and 2 GHz. Grid reflectors and a metal ball were used as targets. A typical experimental setup is shown in Figure 2.9.

Figure 2.9: A typical experiment setup in [57].

A National Instrument Data Acquisition (NI-DAQ) card (PCI-6070E) is used to provide an interface between the computer and the radar circuit [57]. After the radar circuit samples the target response, the DAQ card is used to digitize the received signal, and transmit it back to the computer, where signal processing is performed. The DAQ card provide 16 (multiplexed) 12-bits ADC channels, with maximum sampling rate of 1.25MS/s (mega-sample-per-second). This DAQ card uses the PCI bus , i.e. it requires to fitted onto the motherboard directly. Therefore, this system is difficult to be carried around.

Experiments were carried out using the the following procedure

- At start of each experiment, a background profile is captured. This background profile contains echoes from the stationary objects in the scene, such as tables and chairs.
- After the background profile has been taken, targets are placed in the scene. Another down-range profile is captured.

- The second captured profile contains the echo from the target, as well as the echoes from the stationary objects in the scene. Hence, the background profile that was captured earlier, can be used to remove the background clutter from the later profile, to reveal the true target response.
- The background-removed target response is processed with an inverse filter, defined between 1 GHz and 2 GHz. A Hanning window is applied to reduce the side-lobes of the filtered signal.

Figure 2.10 shows a range profile obtained using this single-channel UWB radar without its front-end amplifier. The target, a small metal grid (dimension: 550x390 mm), is placed 50 cm in front of the radar. Figure 2.10 shows that the received and sampled voltage of a small metal grid target is approximately 9.3 mV.

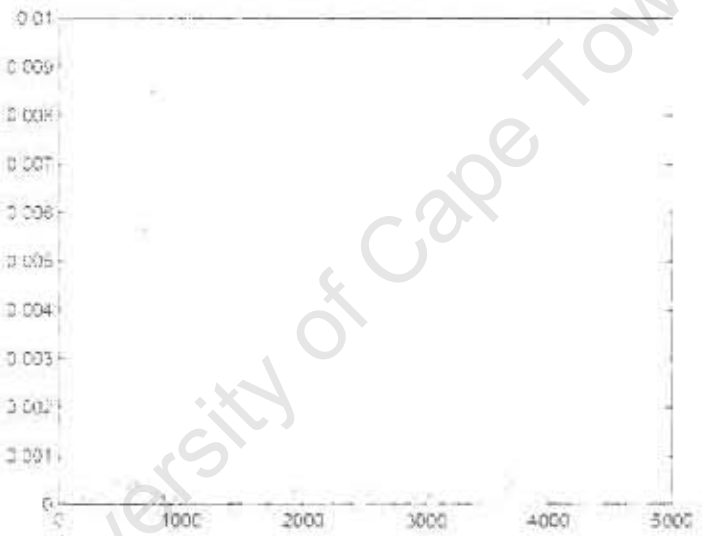

Figure 2.10: An example of the range profile captured by the radar system (without the RF amplifier) constructed in [57]. A small metal grid target is placed 50 cm in front of the radar. X-axis is number of range bin (spans from -2.33 m to 9.35 m) and y-axis is voltage(V).

Table 2.4 summarizes the results obtained from [57].

Experiment	Experiment setup	System gain setting	Results
Maximum range detection	A small grid reflector (550 mm × 390 mm) is used as the target. The target is slowly moved away from the radar. At each position, a target response profile is captured.	(1) Without RF front-end amplifier. (1) With RF front-end amplifier	(1) In the target response profile, the target is visible up to a range of 1 m. (2) In the target response profile, the target is visible up to a range of 5 m.
Detecting multiple targets	Two targets were used: a metal ball, which is placed at 1 m away from the radar, and the small grid reflector, which is placed at 2.5 m away from the radar.	With RF front-end amplifier	Two target can be resolved from the target response profile.
Detection through wooden partition	• A wooden partition with dimensions $120\,(W) \times 2\,(B) \times 180\,(H)$ cm is placed at 1 m away from the radar. • A small grid reflector (550 mm × 390 mm) is used as the target. The target is slowly moved away from the radar. At each position, a target response profile is captured.	With RF front-end amplifier	• Target detections were performed from 1 m (the distance between the target and the radar) up to 3 m. At 3 m, the peak voltage of the return echo (after background profile has been removed) is 0.338 V. The gain of the front-end amplifier used is ≈25 dB. However, the gain of the post-amplifier is unknown. • Comparing to the target response of a small grid reflector positioned at 3m (without obstructed by wooden partition), approximately 20.5% of signal voltage is attenuated by wooden partition.
Detection through concrete partition	• The radar system is placed against a 23 cm thick cement wall. • A large grid reflector (830 mm × 485 mm) is used as the target. The target is slowly moved away from the radar. At each position, a target response profile is captured.	With RF front-end amplifier	Target is only visible when the target is placed next to the 23 cm thick cement wall.
Signal-to-Noise (SNR) Ratio	• 10 noise profiles are captured and averaged. The noise profile is captured without target in the scene. • A unspecified target is placed in the scene after the noise profiles have been taken. The target is slowly moved away from the radar. At each position, a target response profile is captured.	With RF front-end amplifier	• The averaged noise profile has a peak value of 4.28 μV. • As the target moved away from the radar, the peak value of the return echo dropped from 3.28 mV to 0.425 mV, with target moved from 1 m to 3 m. The SNR is reduced from 57.7 dB to 39.9 dB respectively.

Table 2.4: Summary of the experiment results shown in [57].

Chapter 3

Ultra-wideband System Overview

In this chapter, the UWB phased array system architecture will be presented. Firstly, the design specifications of the UWB system will be introduced, which is then followed by a brief explanation on the radar operation. The signal processing techniques that will be used in processing the raw data will be discussed the last.

3.1 Design Specifications

3.1.1 Frequency Selection

As discussed in Section 2.1.1, the bandwidth of a bandpass-type (i.e. spectrum similar to Figure 2.2(b)) is determined by

$$B \approx 1/\tau$$

where B is the 3 dB bandwidth of the pulse and τ is the 3 dB pulse width.

A bandlimited impulse with pulse width $\tau \approx 0.5\,\text{ns}$ has a bandwidth of 2 GHz, which has significant frequency components from very low frequency (close to DC) to approximately 2 GHz.

In order to perform through-wall imaging effectively, the system frequency selection is important. Although the low frequency components (below 1 GHz) have better penetration through solid material than the high frequency components, antennas which operate at low frequency tend to have a large structure. Hence, one is required to select a frequency spectrum, which has moderately low frequency, for good material penetration, and still works efficiently with moderately small structure antennas.

Hence, this UWB system is designed to operate between 1 GHz to 2 GHz. With 2 GHz being the highest frequency component, the minimum sampling frequency required is 4 GHz according to the standard Nyquist theorem. If however the signal is bandlimited

to occupy a range between 1 GHz and 2 GHz prior to sampling, according to the Nyquist theorem for bandlimited signal (refer to Appendix B), it is actually possible to sample at twice the bandwidth in this case, i.e. at a rate of 2 GHz. To retain flexibility, it was decided to design the system with an effective sample rate of at least 4 GHz.

3.1.2 Range Resolution

The range resolution, ΔR, is measured between the 3 dB points or half power width of the point target response in the range direction [22]. This also indicates the shortest distance between two adjacent targets at which the radar system can distinguish the targets separately. The range resolution is related to the bandwidth by [22]

$$\Delta R \approx \frac{c}{2B}$$

where c is the speed of electromagnetic propagation within a sensing medium and B is the bandwidth of the transmitted pulse.

One of this project's intention is to detect the presence and movement of a person behind a wall. It was noted that a person's dimension is normally greater than 15 cm, and under normal circumstance, people tend to stand at least half a metre or more apart, to avoid feeling uncomfortable. Furthermore, a step-size of an adult is usually greater than 15 cm. Hence, it is concluded that a range resolution of 15 cm should be adequate to detect human presence and movement. This sets the required process bandwidth for this this UWB system, which is 1 GHz.

3.1.3 Pulse Repetition Frequency (PRF)

The pulse repetition frequency is defined as number of pulses transmitted per second. Consider a radar system transmitting pulses at a frequency f_{PRF}. The time interval between the two successive pulses is known as pulse repetition interval (PRI), which is given by $t_{\mathrm{PRI}} = 1/f_{\mathrm{PRF}}$. If the total time taken by the transmitted pulse to reach the target, and return to the receiver, is longer than t_{PRI}, one cannot distinguish whether the echo is return from the first transmitted pulse or the second transmitted pulse. Hence, in order to accurately determine the range of the target, the pulse must be transmitted and the echo must be received before the next pulse is transmitted. The PRF determines the maximum unambiguous range,

$$R_{\max} = \frac{c\,t_{\mathrm{PRI}}}{2} = \frac{c}{2\,f_{\mathrm{PRF}}}$$

The PRF of this UWB system is set to 2.5 MHz, which allows a maximum range of $R_{\max} = 60\,\mathrm{m}$. This maximum range is well adequate for an indoor application (allowing for multiple echoes to die down). Since the room used in experiment is approximately

5 m long (across the room), the maximum range for the sampled down-range profile was set to 5 m.

3.1.4 Image Update Rate

In order to keep the through wall image update as in real-time, a sweep rate of 10 frames per second is desired. The maximum sample spacing, according to Nyquist theorem, is $\frac{c}{2(f_H)} = \frac{3\times10^8}{2(2\times10^9)} = 0.075\,\text{m}$, as the system is operating in the range of 1 to 2 GHz. Since there are 4 channel receivers used in this system, the total number of samples per second is $\frac{R_{max}}{samplespace} \times 4 \div 0.1 = 2667\,\text{sample/sec}$. This is equivalent to the maximum allowed time that one can spend integrating for a range bin (refer to Section 3.2) $t_{bin} = 1/2667 = 0.375\,\text{ms}$. For a PRF of 2.5 MHz ($PRI = 0.4\,\mu s$), the maximum number of integrated samples for each range bin is $\frac{t_{bin}}{t_{PRI}} = \frac{0.375\,ms}{0.4\,us} = 9375$. This objective will be reviewed in Chapter 5.

3.2 System Overview

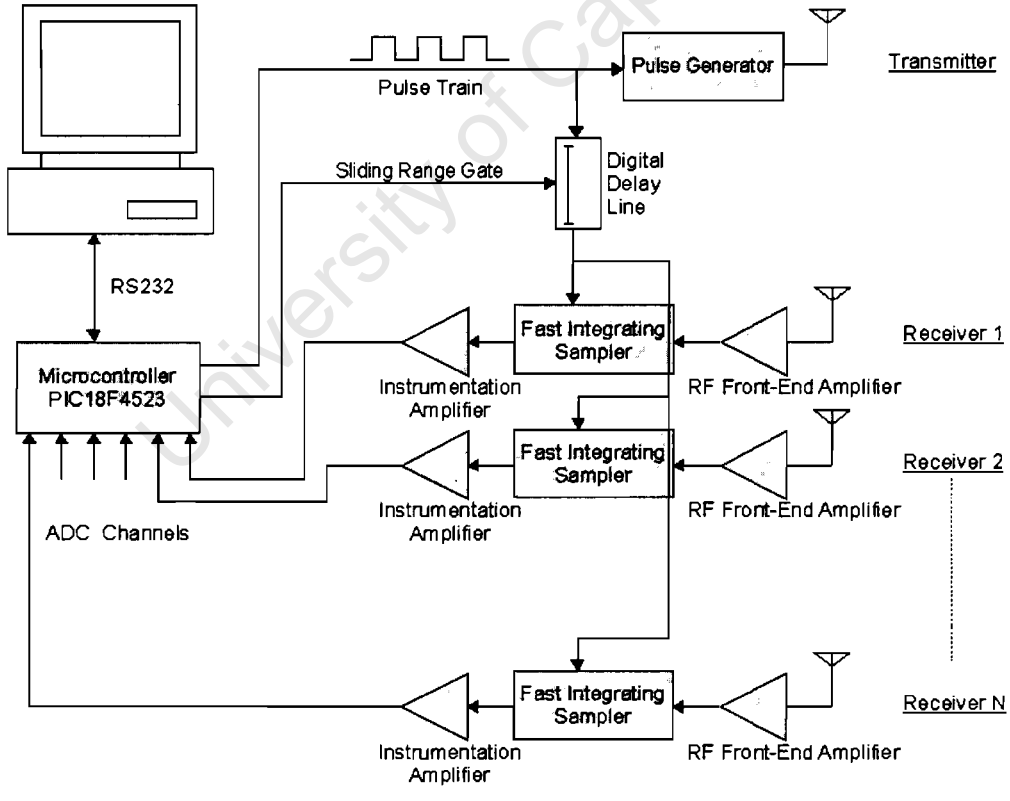

Figure 3.1: UWB phased array system overview

Figure 3.1 shows the UWB array system block diagram. The UWB array system consists of a single transmitter and multiple receivers. A microcontroller, PIC18F4523 from Microchip Technology Inc., is used as a centre piece of this design. It was chosen to

provide various controls and portability to the UWB array system. The functions of the PIC18F4523 are briefly listed below:

- It generates a square wave train, using the timer and the pulse width modulation (PWM) modules [1]. The square wave is used to drive the transmitter and receiver.
- It provides the controls to the programmable digital delay line, which is used in conjunction with the fast-integrating sampler for sampling the received signal.
- It provides control to the analog switches that are used in the fast-integrating sampler.
- It provides 13 (multiplexed) 12-bits analog-to-digital converter (ADC) channels, which are used to digitize the sampled signal.
- It transmits the digitized result from the ADC, via RS-232, to the computer, where the signal processing is performed.

During the radar operation, the pulse generator is triggered by the square wave, which is generated by the microcontroller. The output waveform of the generator is a pulse with pulse width τ_{pulse} typically less than 1 ns. The bandwidth of the pulse is determined by $1/\tau_{pulse}$. Hence the bandwidth of the generated pulse is typically greater than 1 GHz.

If a conventional radar receiver, i.e. receiver that samples of the return signal directly, is used to sample the 1 GHz bandwidth return signal, it will require an ADC with a sampling frequency of at least 2 GHz (Nyquist sampling theorem). In order to lower the requirement of the ADC, a fast-integrating sampler with a digitally-controlled delay line is used for sampling the received signal. Figure 3.2 illustrates the receiver operation.

The blue waveform indicates the transmitted signal, which is produced periodically at a rate of 2.5 MHz. The green waveform indicates the return echoes. The sampler is triggered by the delayed square wave. The delay is set by the delay line, which corresponds to a particular range from the radar. When the delay line is set to T_A, the sampler will sample the voltage that appears on the receiving antenna. The delay is set to be unchanged for a number of pulses, therefore the sampler will sample the return echo at T_A for a number of times. An integrator is used to integrate the sampled echo, and it is reset when the delay is changed to the next value. The output of the integrator is connected to an instrumentation amplifier, which is used to amplify the difference signal between the output of the integrator (integrating sampler) and a reference sampler[2]. Later, by sliding the delay line

[1] The microcontroller is operated with a master clock frequency of 40 MHz. The frequency of the driving waveform to the transmitter and receiver is set by the timer module by scale down the master clock frequency. The PWM module is used to set the duty cycle of the driving waveform [4]. In this design, the frequency of the output waveform is set to 2.5 MHz and duty cycle is set to 50 %.

[2] The input to the reference sampler is a 50 Ω resistor connected to the ground. Hence the reference sampler integrates any noise and temperature drift seen by the 50 Ω load. Since temperature drift is present in both samplers, hence by taking the difference signal between the sampler, the common temperature related drift presented to both sampler can be subtracted, so the amplified signal is less temperature dependent.

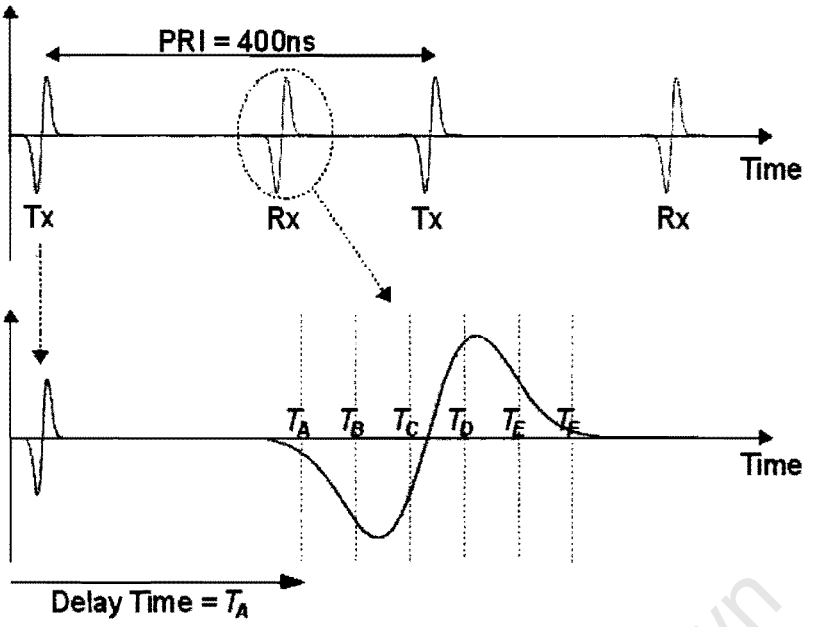

Figure 3.2: The UWB receiver operation

to different value, i.e., T_B, T_C etc., a range profile can be obtained.

The effective sampling rate of the receiver is determined by the step size of the delay line, i.e. the time difference between T_A and T_B. Hence a high sampling rate can be achieved by using a delay line with sub-nanosecond step size. With this implementation, a moderate speed ADC will be sufficient for the application. Furthermore, since many received signals are integrated, the signal-to-noise-ratio (SNR) of the sampled signal is improved.

Finally, a user interface, written in Python, is used to display and process the received signal. It also allows the user to change the settings of the system and initiates data acquisition. Figure 3.3 shows the interface.

3.3 UWB Radar Signal Modeling

The material presented in this section was adapted from [57].

For a single transmitter and receiver UWB radar system, the transmitting signal is sent by the transmitter and reflected from the target in the scene. Since the radar system can be modeled as a linear system, and the practical antenna has a certain bandwidth, the signal received at the receiver is a bandlimited, delayed and scaled version of the transmitted

Figure 3.3: Graphical user interface designed

signal. Assume a point target is placed in the scene, the received signal is expressed as

$$\begin{aligned} V_{rx}(t) &= [V_{tx}(t)]_{bandlimited} \otimes \zeta(t) \\ &= \int_{-\infty}^{\infty} [V_{tx}(t-\tau)]_{bandlimited}\, \zeta(\tau)\, d\tau \end{aligned}$$

where $\zeta(t)$ is the impulse response of the scene, $V_{tx}(t)$ is the transmitted waveform.

Since a convolution in the time domain becomes a product in the frequency domain, the radar model can be expressed as

$$V_{rx}(f) = \zeta(f)\,[V_{tx}(f)]_{bandlimited}$$

Let $H_{tx}(f)$ and $H_{rx}(f)$ be the transfer functions of the transmitting and receiving antenna respectively, and $H_{amp}(f)$ be the impulse response of the front-end amplifier. The signal seen by the fast-integrating sampler is given by

$$V_{rx}(f) = V_{tx}(f)\, H_{tx}(f)\, \zeta(f)\, H_{rx}(f)\, H_{amp}(f)$$

which is valid for a given directions, i.e. $H_{tx}(f)$ and $H_{rx}(f)$ are a function of the direction of arrival of an echo.

Since the transfer function $H_{tx}(f)$, $H_{rx}(f)$ and $H_{amp}(f)$ also represent the gain response of antenna and amplifier respectively, and the gain of the antenna and amplifier change over frequency. Hence, for a UWB system, the antenna and amplifier's transfer function, i.e. $H_{tx}(f)$, $H_{rx}(f)$ and $H_{amp}(f)$, are frequency dependent functions.

3.4 Signal Processing

When targets are placed in the scene, the signal received by the receiver consists of the echoes from the targets and the background clutter, i.e. echoes from objects of no interest in the scene. In order to extract the location of the targets from the clutter, signal processing is required. In this section, the signal processing techniques used will be discussed, namely background subtraction, signal filtering and beamforming.

3.4.1 Background subtraction

In an indoor environment, there are often a lot of reflective objects, other than the target-of-interest, located in the scene, i.e. tables, chairs. Since these objects are stationary, i.e. they will not change its position unless someone moves them. The profile contains these stationary objects, which can be seen as the constant background clutter. When a

profile is captured with a target-of-interest placed in the scene, the background profile, that was captured earlier, can be used to remove the background clutter, i.e. the echoes of the stationary objects, from the later profile. Hence, the target response of the target-of-interest can be revealed.

3.4.2 Linear Signal Filtering

The signal correlation technique can be used to improve the SNR of the received signal. This is achieved by correlating the received signal with a reference signal. In a narrow-band system, the reference signal is a replica of the transmitted signal, as the shape of the signal is normally unchanged during the radar operation. However, for a UWB signal, the shape of the signal is changed many times during the radar operation. These changes are due to the fact that the antenna band-limits the signal, and multiple reflection occurs when the length of the target is greater than the pulse width, i.e. $L_{\text{target}} > c\tau_{\text{pulse}}$. Hence, the reference signal used in the UWB radar is a response of a target recorded by the receiving element.

Two linear signal filtering methods are discussed in this section, namely matched filtering and inverse filtering.

In the matched filtering method, the received signal is correlated with the conjugate of the reference signal. This process is identical to cross-correlation. Let the received waveform be $x(t)$. In white noise case, the matched filter is defined as [22]

$$\begin{aligned} H_{MF}(f) &= X^*(f)e^{-j\pi f\tau} \\ h_{MF}(t) &= x^*(-t-\tau) \end{aligned}$$

where τ is a constant which can be used to shift the location of the output peak. The output of the matched filter is given by

$$y(t) = x^*(-t+\tau) \ast x(t)$$

In the frequency domain,

$$\begin{aligned} Y(f) &= X^*(f)e^{-j\pi f\tau}X(f) \\ &= |X(f)|^2 e^{-j\pi f\tau} \end{aligned}$$

The transfer function of the inverse filter is defined as the inverse of the Fourier Transformed reference signal over a defined bandwidth B. For a basebanded signal[3], the inverse

[3]Baseband signal refers to signal whose spectrum component centred on zero hertz [22]

filter is expressed mathematically as [21]

$$H_{IF}(f) = \begin{cases} \frac{1}{X(f)} e^{-j\omega\tau} & -\frac{B}{2} \leq f \leq \frac{B}{2} \\ 0 & elsewhere \end{cases}$$

where B is the bandwidth of the signal, which is inverse of the pulse length τ

The transfer function of the inverse filter can be expressed in terms of matched filter by multiplying $\frac{X^*(f)}{X^*(f)}$.

$$H_{IF}(f) = \begin{cases} \frac{X^*(f)}{|X(f)|^2} e^{-j\omega\tau} & -\frac{B}{2} \leq f \leq \frac{B}{2} \\ 0 & elsewhere \end{cases}$$

From above equation it is noted that, the inverse filter and matched filter have same phase response over a passband, i.e. $-\frac{B}{2} \leq f \leq \frac{B}{2}$, and the magnitude is differs by the factor $\frac{1}{|X(f)|^2}$ [22, 21]. In the frequency domain, the output of the inverse filter is a *rect* function, and in time domain, this is translated to a $\frac{sin(x)}{x}$ function.

The $\frac{sin(x)}{x}$ function has large sidelobes. In order to reduce the sidelobes, the output of the inverse filter in the frequency domain, the *rect* function, is tapered with window [22, 21]. The weighting function (the 'window') smooths the edges of the band in the frequency domain, which reduces the sidelobes of the time domain response. However, the mainlobe of the time domain response is broaden during the windowing process. Table 3.1 shows the properties of some commonly used weighting functions.

Weighting Function	Peak Sidelobe (dB)	3dB Mainlobe width (relative)	Sidelobe decay
Uniform			
Taylor			
Dolph-Chebyshev			

Table 3.1: Weighting functions for sidelobe suppression [22].

The antenna response and the receiver transfer function of UWB radar system tend to bandlimit the transmitting impulse signal. Hence the signal processing technique described in this section can be applied to the current UWB radar system, as the received signal is bandlimited to a passband, i.e. $-\frac{B}{2} \leq f \leq \frac{B}{2}$. The simulated results using matched filtering and inverse filtering are shown in Chapter 6.

3.4.3 Beamforming / Array Theory

When a linear array of receivers is used, it is possible to resolve both range R and angle of arrival θ of a target in the scene. Figure 3.4 illustrates the geometry of a linear array of receiving elements.

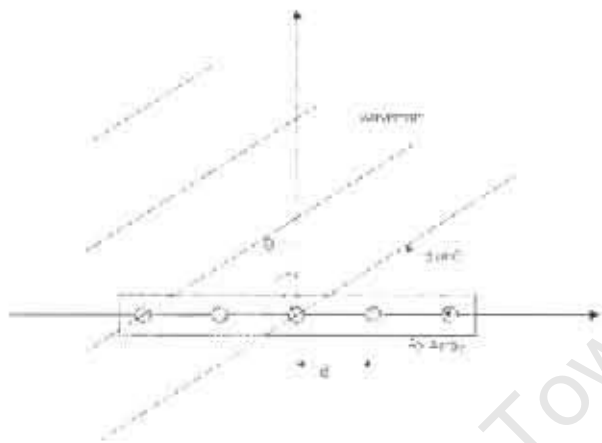

Figure 3.4: Geometry of a linear array

Assuming a point target is situated sufficiently far from the radar, the wavefront reflected from the point target can be approximated as a planar wave when it reaches the receiving elements. From Figure 3.4, it shows that the wavefront arrives at each receiver at a different time delay. The time difference between two adjacent receiving element can be calculated by $\tau = \frac{d\cos(\theta)}{c}$, where d is the distance between the adjacent receiving element, θ is the angle of arrival of the wavefront and c is the speed of light ($\approx 3 \times 10^8$ m/s). This time difference can also be expressed as a phase shift between the array element as $\psi = \frac{2\pi d \sin(\theta)}{\lambda}$, where λ is the wavelength. By summing the received signal from all the receiving elements with appropriate delay and phase compensation, a beam may be found in a particular direction.

Since the angle of arrival of the return echo from the point target is unknown, a beam steering algorithm is used to focus the image. Figure 3.5 illustrates the beam focusing operation. The beam will be steered from $-\theta_{max}$ to θ_{max}, where all points along a particular angle θ_i will be evaluated by 'delay and sum' beamforming, with appropriate phase compensation as the processing will be done on basebanded data (i.e. spectrum of the range compressed data is first translated to baseband). The focused signal at point 'a' at angle θ_i is expressed as [22]

$$Output_{\theta,a} = \sum_{n=0}^{N-1} x_n(t = \tau_{a,\theta_i}) e^{j2\pi n d \sin(\theta_i)/\lambda}$$

where n is the element index in the array, N is the number of receiving element in the

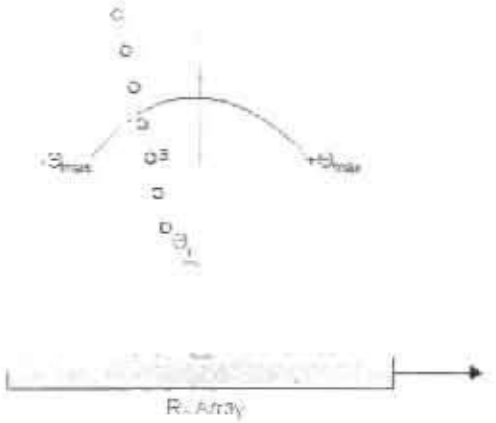

Figure 3.5: Beam focusing operation

array. $x_n(t)$ is the basebanded signal for receiver n and $\tau_{a\,\theta_i}$ is the time delay from focused point a at angle θ_i to the receiving element.

Since the signal is sampled at discrete points along the array, the spacing between the array elements needs to be small enough to avoid spatial aliasing [22]. The result of spatial aliasing is known as the 'grating lobe effect', where the lobes are repeated at several angles, with the same amplitude as the main lobe. To avoid completely spatial aliasing, the array elements are required to be spaced at less than $\lambda/2$. If the requirement is not met, the first grating lobe occurs (with respect to a beam on boresight) when the phase shift between the array element is 2π [22]. Solving for $\frac{2\pi d sin\theta}{\lambda} = 2\pi$, it yields

$$\theta_{\text{grating lobe}} = arcsin(\frac{\lambda}{d})$$

Hence, the maximum steering angle is limited to where the phase shift between the array element is π [22]. Solving for $\frac{2\pi d sin\theta}{\lambda} = \pi$, it yields

$$\theta_{\max} = arcsin(\frac{\lambda}{2d})$$

In the UWB impulse array, the grating lobes effect is absent. Since the spectral components of a wideband signal is spread over a large range of frequencies, the grating lobes occur at different angle for a different frequency. While the mainlobes are added coherently, the grating lobes are averaged over the frequency spectrum. Hence, the grating lobes are suppressed [45]. Figure 3.6 illustrate this phenomenon, where f_{HIGH} and f_{LOW} are the array focused beam for high frequency component and low frequency component of the impulse respectively. As illustrated in Figure 3.6, the mainlobes for different frequencies are located at the same angle and are being added constructively; whereas the grating lobes are occurred at different angles for different signal frequencies. The misalignment of the grating lobe averaged the lobes over the frequency spectrum.

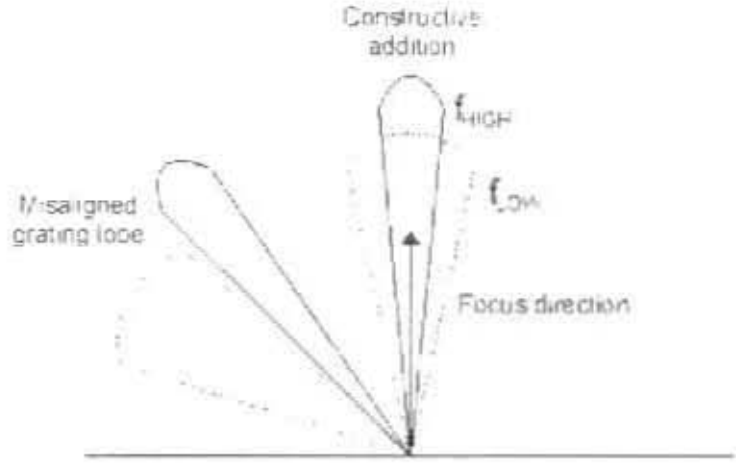

Figure 3.6: Plot illustrate misalignment of the grating lobes in the case of UWB impulse array system.

Another way to look at this is in the time domain. The delay and sum beamformer aligns echoes from a particular direction (or position (R, θ)). Even if the phase shift is an integer multiple of 2π at the grating lobe angles, the data will not be perfectly time aligned for the grating lobe direction if the range resolution is sufficiently fine.

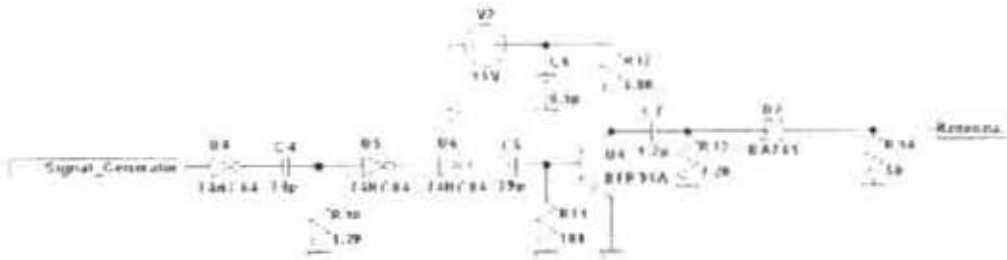

Figure 4.2: Pulse generator circuit design described in [57]

of Q4 rise to 15 V, and C7 is charged through the loop V2—R12—C7—R13—Ground. Figure 4.3(a) shows the simulated waveform at node C5-R11-Q4 and Figure 4.3(b) shows the simulated waveform at node R12-Q4-C7. The square waveform shown Figure 4.3(a) and (b) is the simulated 2 MHz driving signal. Micro-Cap simulator is used for this circuit simulation and plots generation.

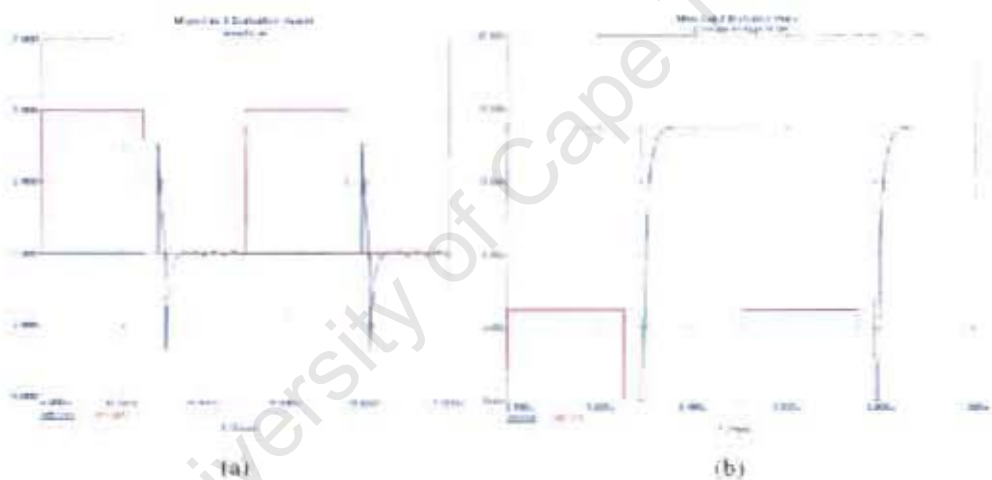

Figure 4.3: Simulated waveform at (a) node C5-R11-Q4, and (b) node R12-Q4-C7.

At the instance when the transistor Q4 is triggered, the collector voltage is drops from approximately 15 V to 0 V, which results in a -15 V drop on node C7-R13-D2. This causes the Schottky diode D2 to conduct, and discharges C7 via R13, R14 and impedance of the antenna, Ra, toward 0 V. The charging time constant of C7 is approximately $\tau_{Discharge} = C2 \times (R14//R13//Ra) \approx 30\,\text{ps}$. Thus a negative pulse is generated across the antenna feed. Figure 4.4 shows the generated pulse and Figure 4.5 shows the DFT analysis reproduced from [57]. The measurements and the DFT analysis was performed using Agilent Infinium 54833A DSO (digital storage oscilloscope). From Figure 4.5, it shows that the measure pulse bandwidth is approximately 1 GHz. However, this analysis is band-limited by the DSO used. Hence, the bandwidth of the generated pulse could be wider.

In this thesis, the pulse generator is further modified from [57]. Figure 4.6 shows the

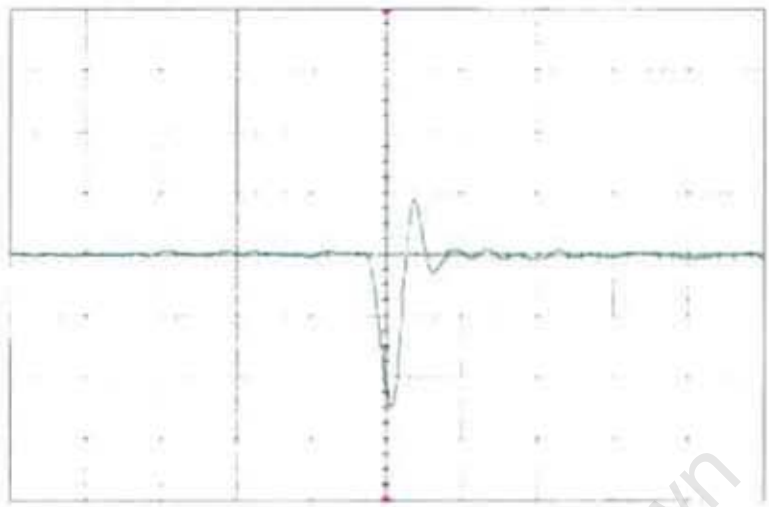

Figure 4.4: The output waveform from [57].
Vertical scale: 500 mV/div (with 0 V offset)
Horizontal scale: 2 ns/div

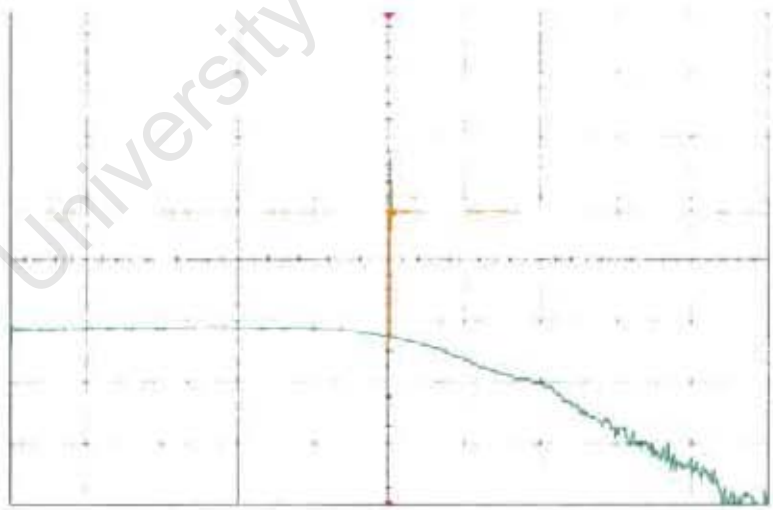

Figure 4.5: The output waveform from [57] with DFT analysis beneath.
Time-domain vertical scale: 500 mV/div (with -379 mV offset)
Time-domain horizontal scale: 50 ns
DFT vertical scale: 20 dBm/div
DFT horizontal scale: 200 MHz/div (range 0 to 2 GHz, centre position corresponds to 1 GHz)

revised circuit diagram, which is produced using Kicad. R5 and C6 are used to generate a time delay which is used to match with the initial delay set by the digital delay line in the fast-integrating sampler (described in Section 5.1). The other changes are aimed to generate a similar but shorter pulse, with a higher peak-to-peak voltage.

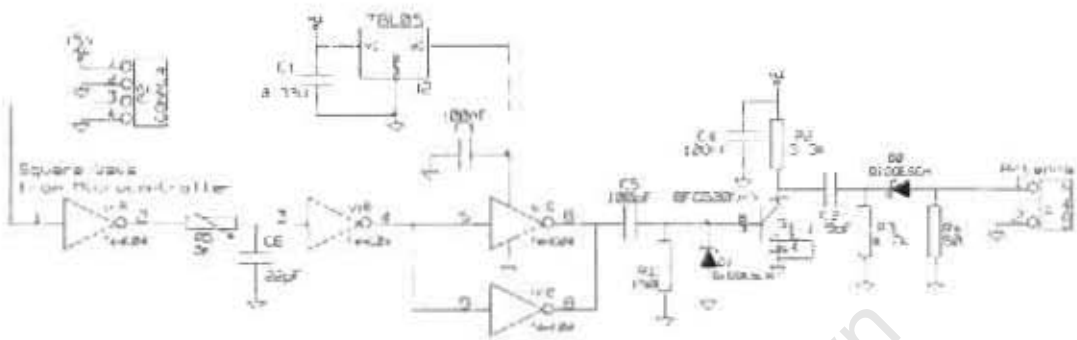

Figure 4.6: UWB pulse generator circuit diagram.

The bandwidth of the pulse generated is determined by the sharpness (risetime) of the triggering square wave driving C5 and R1 and the transistor base impedance. The sharpness of the square wave, together with the characteristic of the transistor used, will determine the speed of switching action, which leads to the charging and discharging of the output waveform. The amplitude of the generated pulse is affected by the response of the charging capacitor C2 in the high frequency spectrum.

In the following sections, the improvements that are performed on the pulse generator will be discussed, and results will be presented.

4.2 Triggering Edge of the Square Waveform

In this design, two inverters, U1C and U1D, are used in parallel to shorten the rise- and fall-time of the square waveform. The Agilent Infinium 54833A DSO is used to measure the transition time. The averaging function on the DSO is set to average many pulses, in which the mean transition time is obtained. Figure 4.7 and Figure 4.8 show the observed rise- and fall-times for the case of a single inverter and a two parallel inverters.

For a single inverter, the 10% - 90% rise-time and fall-time are approximately 2.25 ns and 2.00 ns respectively. In the case of two parallel inverters, the rise-time and fall-time are approximately 0.91 ns and 0.88 ns respectively. This shows that the edge of the square wave in sharpened through this modification, which is due to the increase in current drive into the capacitor C5, when two parallel inverters are used.

(a) Rise-time (b) Fall-time

Figure 4.7 Transition time measure at the output of a single inverter

(a) Rise-time (b) Fall-time

Figure 4.8: Transition time measure at the output of two-parallel inverters

The BFG520W/X RF transistor was used to replace the transistor BFR91A, that was used in [57]. Table 4.1 is constructed to compare the performances between these two RF transistor. Table 4.1 shows that BFG520W/X has a lower feedback capacitance (between collector and base of the transistor), which enables a faster switching action than the BFR91A RF transistor. The output wave observed on the DSO, shows a marginally increase in its peak amplitude. There are many other RF transistors which have lower feedback capacitance, however, it is at the expense of low collector-emitter breakdown voltage, i.e. typically less than 10 V, which is not suitable for this design.

	BFR520W/X	BFR91A
Collector-emitter breakdown voltage	15 V	12 V
Collector current (maximum)	70 mA	50 mA
Transition frequency (unity current gain frequency)	9 GHz	6 GHz
Feedback capacitance	0.35 pF ($V_{CB} = 6$ V)	0.4 pF ($V_{CB} = 5$ V)
Noise Figure	1.1 dB (at 900MHz)	1.6dB (at 800 MHz))

Table 4.1: Comparing the performance of BFG520W/X and BFR91A [16, 17]

4.3 Interdigital Capacitor

The charging capacitor C2 in Figure 4.6 is responsible for the pulse amplitude and pulse shape of the generated waveform. All capacitors have an inductive component in series with the capacitance component. The inductive component causes an increase in transmission loss when a higher frequency signal is applied to the capacitor [42]. Hence a capacitive element with less inductive component will be more suitable for generating very short pulses.

Two capacitive elements were investigated, (1) the surface mount chip capacitor, which is widely used in printed circuit board assembly (PCB), and (2) the interdigital capacitor (IDC).

The IDC is a microstrip line element, which is used for producing small capacitances. Figure 4.9 illustrates the geometry of an IDC. The capacitance of the IDC is determined by the thickness, length (L) and width (W) of the conductors (the microstrip line). Generally, when the characteristic impedance (Z_0) of the conductor increases, the effective capacitance decreases. Furthermore, the capacitance is also increased as the gaps between the conductors decrease. Finally, as the conductors are mounted on a substrate, the thickness and the dielectric constant (ε_r) of the substrate affect the effective capacitance of the conductors [3].

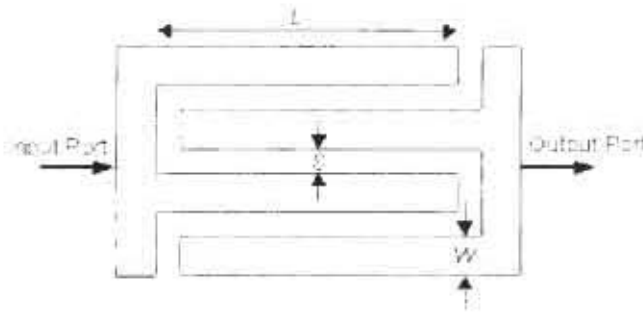

Figure 4.9: Interdigital capacitor geometry

The capacitance of the IDC can be calculated using following equations obtained from [42]

$$C = (n-1)C_0L$$

$$C_0 = \varepsilon_0(1+\varepsilon_r)\frac{K(k)}{K(k')}$$

$$k = \tan^2(\frac{\pi}{4}\frac{W}{W+S})$$

$$k' = \sqrt{1-k^2}$$

where n is the number of conductors, L is the length of each conductor, W is the width of each conductor, S is the spacing between the conductor and ε_0 is the permittivity of free space ($\approx 8.854 \times 10^{-12}$ F/m). These equations assume that the thickness of the conductors are zero. $K(k)$ is a complete elliptic integral which can be approximated with following equation with an error of 3% or less [42].

$$\frac{K(k)}{K(k')} = \begin{cases} \pi/ln(2\frac{1+\sqrt{k'}}{1-\sqrt{k'}}) & 0 \leq k^2 \leq 0.5 \\ \frac{1}{\pi}ln(2\frac{1+\sqrt{k}}{1-\sqrt{k}}) & 0.5 \leq k^2 \leq 1 \end{cases}$$

The difference between the calculated capacitance and the actual capacitance could result from:

- The conductors have a non-zeros thickness. Hence the actual capacitance could be higher.
- A small amount of substrate is removed during the milling process[2], which results in a smaller capacitance than the calculated value.

Testing boards are made to compare the performance between a multi-layer ceramic chip capacitor and an IDC. Figure 4.10 shows the testing board made for the IDC. The testing

[2]PCB milling machine is used for rapid development of prototypes.

board for a 1.5 pF ceramic chip capacitor has a similar layout. The IDC that is made consists of 14 conductors (fingers), which are formed on a FR4 board ($\varepsilon_r \approx 4.34$). The dimensions of the IDC are listed below

- Width of the conductor = 0.508 mm
- Length of the conductor = 3.937 mm
- Space between the conductors = 0.254 mm

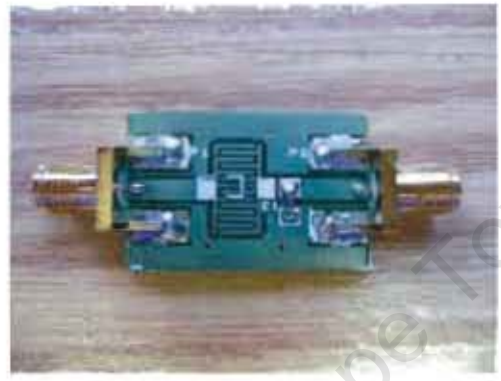

Figure 4.10: Testing board for the interdigital capacitor

The calculated capacitance, using the above equations, is approximately 1.55 pF.

In order to compare IDC with the chip capacitor, an S21 measurement for both boards was performed with Agilent E5071B network analyzer. Figure 4.11 shows the circuit diagram and depicts the S21 measurement condition. Port 1 of the network analyzer is represented by a signal source with 50 Ω resistor, and port 2 is represented by a 50 Ω resistor to ground. This configuration is a high pass filter with a theoretical 3 dB cut-off at $\frac{1}{2\pi(R_1+R_2)C} \approx 1$ GHz.

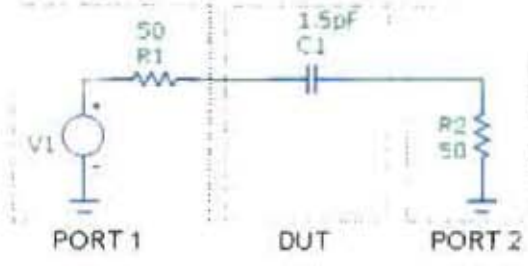

Figure 4.11: The circuit diagram for S21 measurement of the high pass filter

The loss in the passband of the high pass filter, formed by the chip capacitor and input impedance of Port 1 and Port 2 of the network analyzer, is approximately 8.16 dB at 1.35 GHz, as shown in Figure 4.12(a). Comparing to the 4.36 dB at 1.36 GHz loss due

to the high pass filter formed with an IDC, shown in Figure 4.12(b), proves that the interdigital capacitor improves the efficiency in passing high frequency signals. Furthermore, the passband shown in Figure 4.12(a) is not flat, and there is an unwanted resonance at 1.52 GHz, which makes it unsuitable for our application.

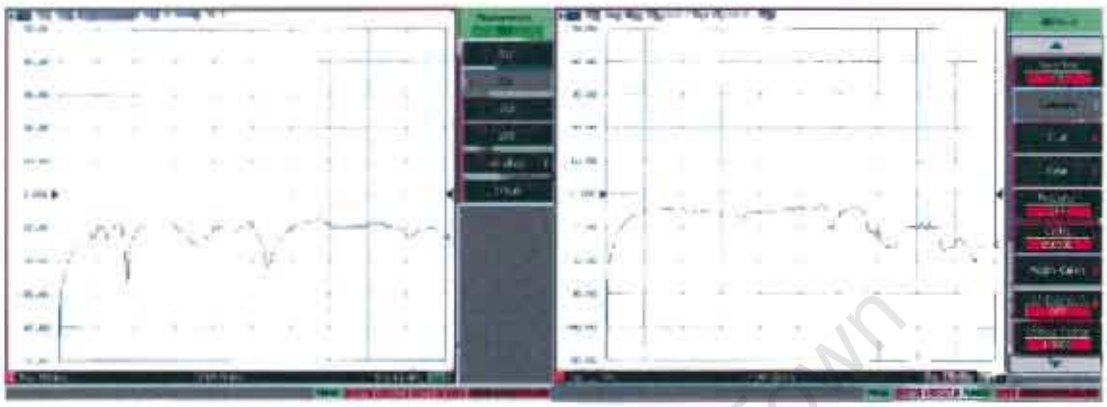

(a) Chip capacitor (b) Interdigital capacitor

Figure 4.12: Comparing the S21 measurement for the high pass filter, using different capacitor element. The x-axis spans from 300 KHz to 8.5 GHz. The y-axis is 10dB/div.

The capacitance of the interdigital capacitor can be estimated from Figure 4.12(b). The cut-off frequency of the high pass filter, formed with IDC and input impedance of Port 1 and Port 2 of the network analyzer, is approximately 1 GHz (observed on the network analyzer). The capacitance of the IDC can be calculate using the setup shown in Figure 4.11 as

$$C_{IDC} = \frac{1}{2\pi f_{cut\text{-}off}(R1 + R2)} \approx 1.59\,\text{pF}$$

The measured capacitance of the IDC is approximately 2.6% higher than the calculated value.

Figure 4.13 shows the UWB pulse generator board that was made, which is based on the circuit design shown in Figure 4.6. Figure 4.14 shows the generated pulse observed on the DSO. Comparing to Figure 4.4, it shows an approximately 450 mV increase in the pulse amplitude, while maintain the same pulse width. The DFT analysis (Figure 4.15) shows a signal bandwidth of 1 GHz is achieved with the new pulse generator. However, the true pulse width is shorter and the true pulse amplitude is greater than that observed on the oscilloscope.

Figure 4.13: UWB pulse generator PCB

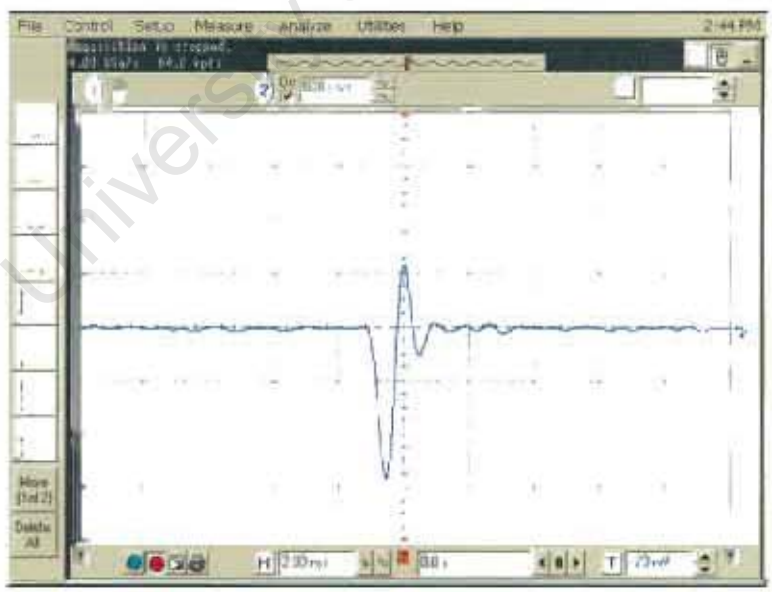

Figure 4.14: The measured waveform at the output of the new pulse generator
Vertical scale: 500 mV/div (with 0 V offset)
Horizontal scale: 2 ns/div

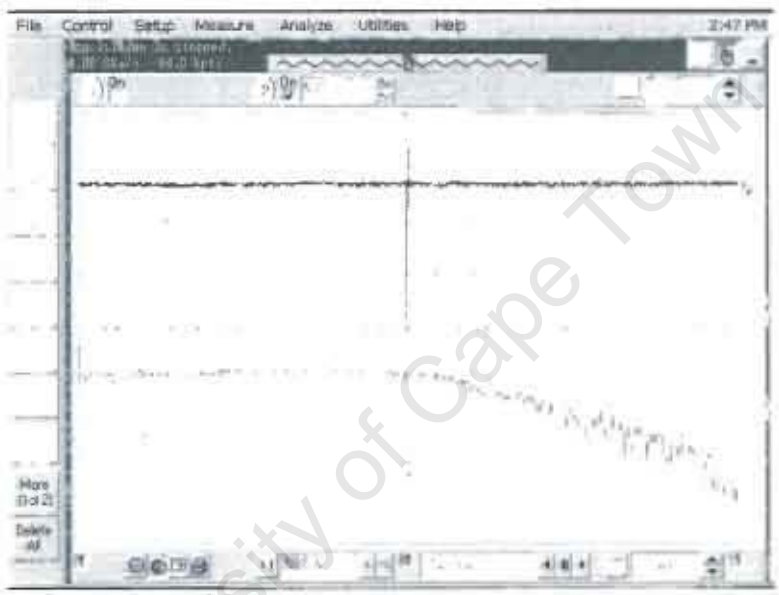

Figure 4.15: The measured waveform at the output of the new pulse generator with DFT analysis
Time-domain vertical scale: 500 mV/div (with 1.180 mV offset)
Time-domain horizontal scale: 50 ns/div
DFT vertical scale: 20 dBm/div (with -15 dBm offset)
DFT horizontal scale: 200 MHz/div (range 0 to 2GHz, centre position corresponds to 1 GHz)

Chapter 5

Multi-Channel Ultra-Wideband Receiver

In order to record and digitize the receiving waveform accurately, the sampling rate of the receiver must be at least twice the bandwidth of the received signal. for a band-limited signal. For an impulse radar system that uses signal with 1 ns pulse width, a minimum of about 2 GHz sampling frequency is required for adequate processing and digitizing of the received signal. If a conventional receiver design is used, this would impose a very high sampling rate requirement for the analog to digital converter (ADC).

One of many ways to sample a wideband signal without using a high sampling rate ADC, is to channelize the receiving signal into several parts and use multiple ADC thereafter [37]. This can be done either in the frequency domain or time domain.

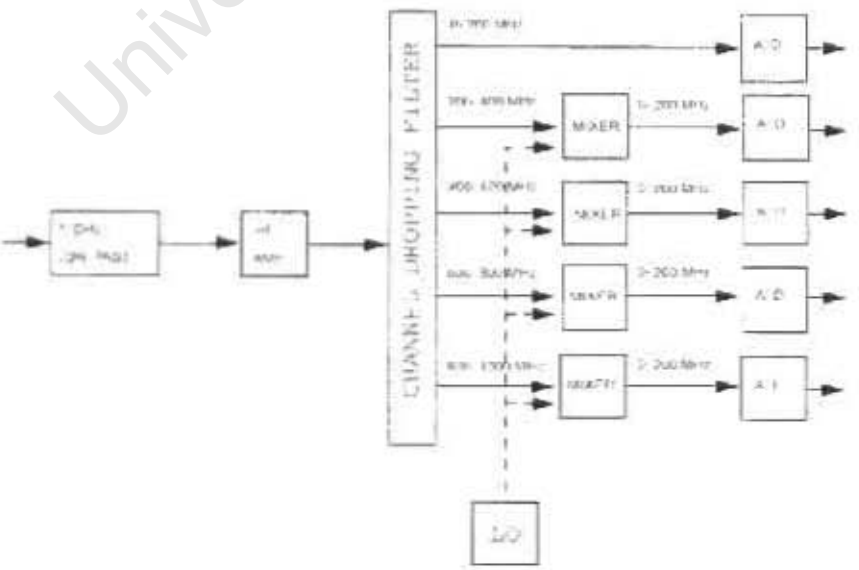

Figure 5.1: The frequency domain channelized receiver for 0-1 GHz signals [37].

Figure 5.1 shows a typical frequency domain channelized receiver architecture for a 0 to

1 GHz receiver. The duplexer, or the channel dropping filter, separates the signal into sections which fit into the sub-channel bandwidths of 0-200 MHz, 200-400 MHz, etc. The requirement for ADC is determined by the sub-channel bandwidth. The problem of using a frequency domain channelized receiver is that the duplexers are expensive. In addition, the duplexer used needs to have a good impulse response and sharp cutoffs to avoid signal distortion [37].

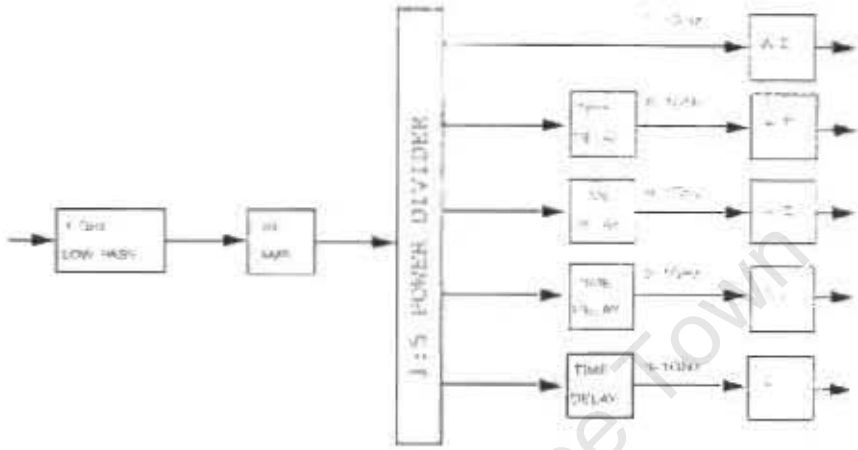

Figure 5.2: The time domain channelized receiver for 0-1 GHz signals [37].

Figure 5.2 shows the time domain channelized receiver architecture for a 0 to 1 GHz receiver. This architecture uses multiple time delay elements. The time delay element provides a time delay between its output and its input. Each time delay element has a different value $T_{\text{delay element}}$, i.e. 0.5 ns, 1.0 ns, 1.5 ns etc., and each of the time delay corresponds to a range value of $R_{\text{delay element}} = \frac{c * T_{\text{delay element}}}{2}$. The return signal is sampled by the receiver at discrete time intervals, i.e. the output of the 0.5 ns time delay element is the sampled voltage of the return signal at time of 0.5 ns, and so forth. By summing the output of samplers, i.e. ADCs, a range profile is obtained.

The architecture shown in Figure 5.2 samples the return signal directly, which minimizes the possible distortion of the signal that could occur before the sampling process. Furthermore, this receiver preserves the instantaneous 1 GHz signal bandwidth.

The sampling rate of this receiver is the inverse of the difference in time-delay between two adjacent delay element, i.e. $\Delta T_{\text{delay element}}$, e.g. 0.5 ns time-difference between delay elements is equivalent to a sampling rate of 2 GHz. Furthermore, the number of time delay elements used, determines the maximum range that the receiver can detect. For a 2 GHz sampling frequency receiver, a total of 14 time delay elements, with $\Delta T_{\text{delay element}}$= 0.5 ns, and ADCs are required for detecting a maximum range of 1 m.

Therefore, UWB receivers using adjustable delay lines have been developed [51, 30, 57].

Figure 5.3 shows a receiver circuit [30] which consists of a manual delay structure, using a potentiometer with a capacitor, and Figure 5.4 shows the receiver circuit with a varicap diode delay line [57] added to make an electronically adjustable delay. Only one sample is taken per pulse transmitted at the time set by the delay line. The 10 nF capacitors are charged via a 'sample and integrate' approach explained in more detail in Section 5.3.

The delays are generated by varying the RC time constant in both designs. The capacitance of the varicap diode can be varied by changing the voltage across the varicap diode. Together with a resistor, a computer-controlled (a DAC is used to control the voltage across the varicap diode) delay line was developed [57]. This provides a more robust solution to a radar range profiling system than the manual delay line described in [30].

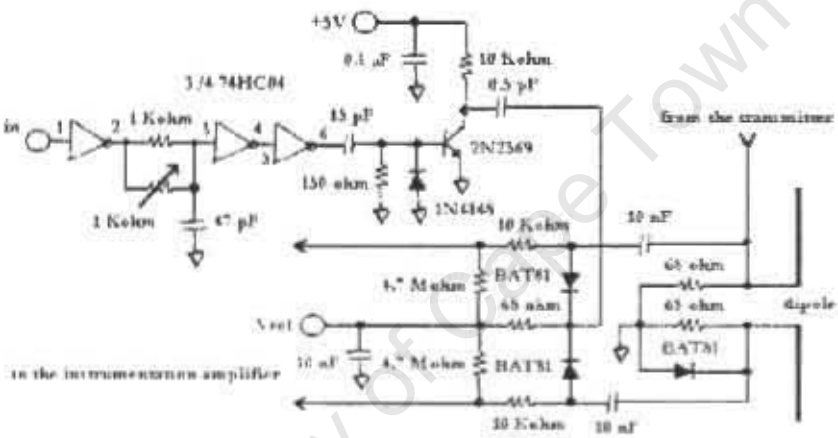

Figure 5.3: The delay line and the fast sampler averager [30].

In this thesis, a programmable digital delay line is used with a revised fast-integrating-sampler. Figure 5.5 shows the block diagram of the new receiver. In the following sections, the function of each module in the receiver will be explained.

5.1 Programmable Digital Delay Line

The range profile is obtained by changing the time delay produced by the delay line, in discrete steps. Several hundred pulses are typically transmitted. The echoes sampled and integrated at the particular delay corresponding to a specific range. Hence the accuracy and stability of the delay element is very important. In addition, the step size of the delay element determines the effective sampling frequency fs of the receiver ($f_s = \frac{1}{\Delta t}$, where Δt is the step size of the delay line), therefore it should be small enough to provide a sufficient sampling rate. The varicap diode delay line in Figure 5.4 is found not well suited to this application as the response of the varicap diode is not linear. In addition, the capacitance is temperature dependent. Figure 5.6 shows the time delay generated by a varicap

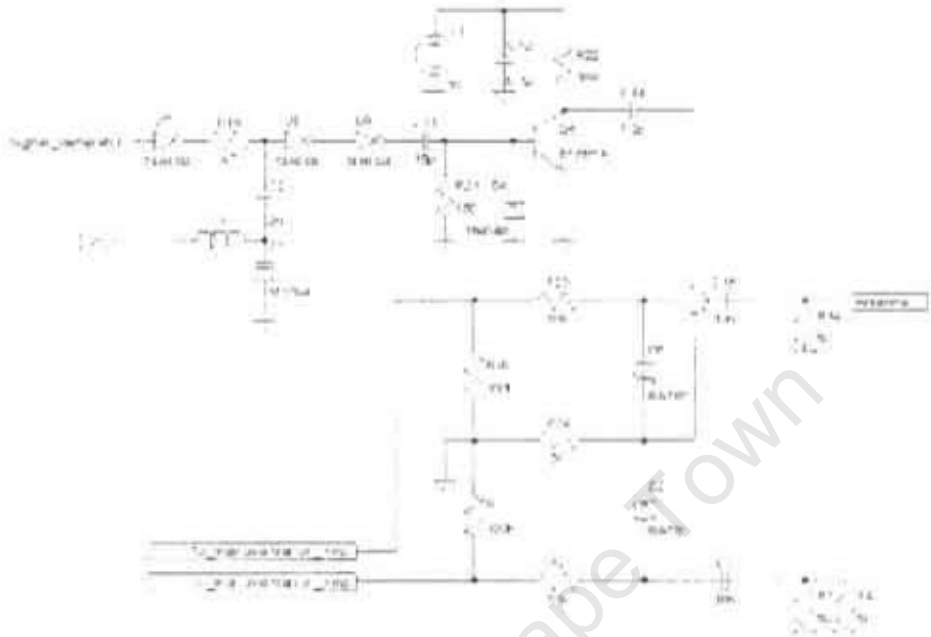

Figure 5.4: The computer-controlled delay line and the fast sampler averager [57].

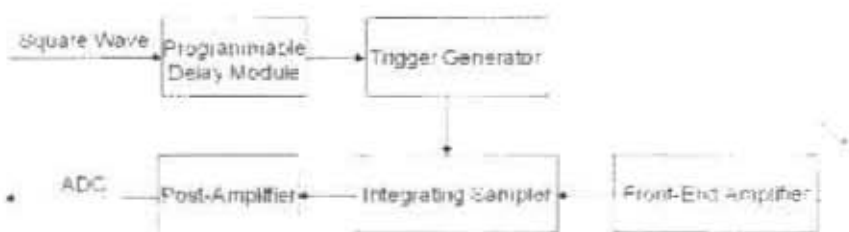

Figure 5.5: Block diagram of the UWB receiver.

diode MV104, a 2 nF capacitor and a 47 Ω resistor, over a range of voltage that is applied across the varicap diode [57].

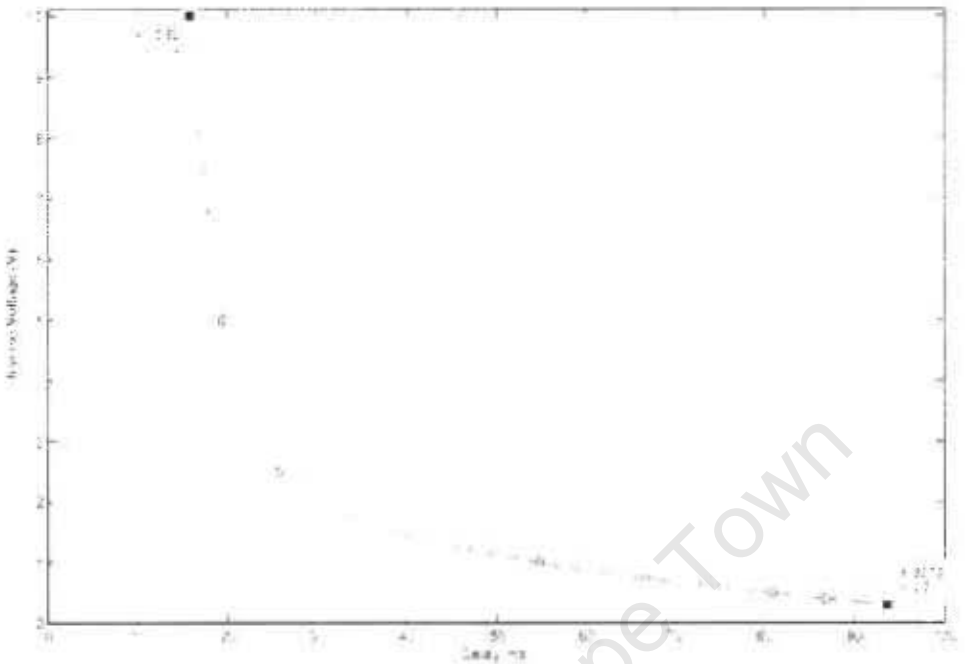

Figure 5.6: The time delay generated by varicap diode circuit v.s. reverse voltage [57].

The programmable digital delay line, DS1020 series [1, 8], was chosen to replace the varicap diode delay structure. The DS1020 series is an 8-bit programmable delay line, with delay step size as small as 0.15 ns. In addition, it allows an option between programming on its serial port or parallel port. The DS1020-015 (0.15 ns step size) was chosen for the application, as it provides an effective sampling frequency of 6.67 GHz for the UWB receiver. This sampling frequency is slightly higher than the minimum sampling requirement calculated in Section 3.1.1. A finer-step-size delay line is commercially available from [7], with the step-size as small as 50 ps (PDH6050). However, the cost of this component is much higher than DS1020 series (PDH6050 costs approximately $130, whereas DS1020-015 costs $47), therefore, PDH6050 is not chosen for this project.

With DS1020-015 delay line, a total of 255 delay steps is allowed, hence, the maximum range of detection is approximately 5.76 m. A second delay line, DS1020-050 (0.5 ns step size) can be used in series with the DS1020-015 to provide a longer range profile. However, by increasing the length of the range profile, it decreases the maximum profiling rate of the system. Furthermore, each delay line produces time delay with a certain deviation. Therefore, if two delay lines were used, calibration is required for delay time alignment. Calibration is used to ensure that the combined delay time is increased without missing or repeat a delay step. To demonstrate that using programmable delay line improves the radar stability and accuracy, when compared to the varicap diode delay line, it was decided that the use one delay line, DS1020-015, will be sufficient, as it met the requirement

for maximum range detection calculated in Section 3.1.3. Figure 5.7 illustrate the basic operation of the DS1020 delay line.

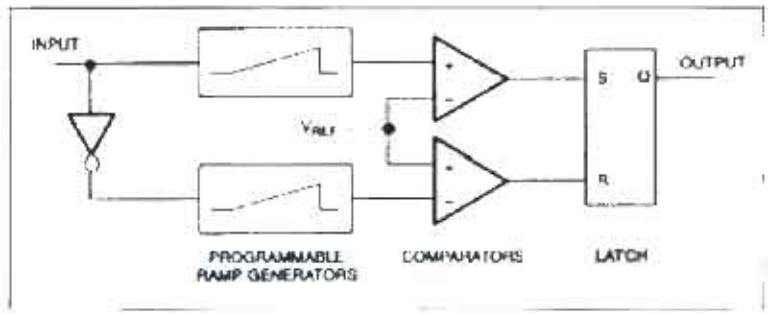

Figure 5.7: Block diagram of the DS1020 architecture [8].

The rising-edge of the input signal initiates the top ramp generator. When the output of the ramp generator exceeds the reference voltage, the output of the comparator will set the latch, and produce a high level output voltage ($\approx 5V$). The falling-edge of the input signal will trigger the second ramp generator, which will reset the latch when the output of ramp generator is higher than the reference voltage. The time taken for the ramp generators to reach the reference voltage is equivalent to the delay time that is programmed by the user.

The ramp generator contains capacitors and a programmable current source. The magnitude of the current source determines the rate at which the capacitor is charged, which is equivalent to the rate at which the ramp generator is increased. The current source is generated by an internally derived reference voltage through an array of resistors. The binary codes that are programed by the user, determine the selection of the resistor from the array, which changes the magnitude of the current source [8]. The microcontroller, PIC18F4523, is used to provide the 8-bit parallel programming bits to the delay line. Figure 5.8 shows the delay line module and Figure 5.9 shows the microcontroller demo board (supplied by Microchip Technology Inc.) used in this thesis.

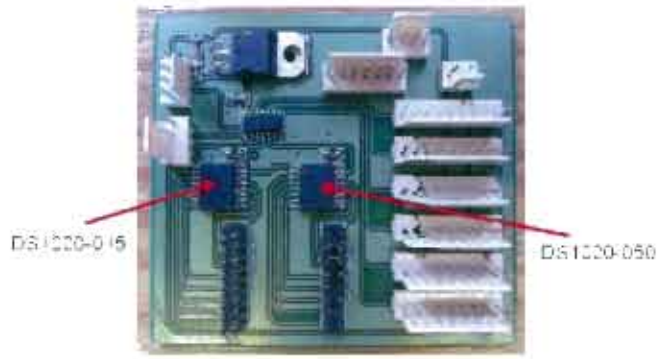

Figure 5.8: Programmable delay line DS1020-015 and DS1020-050.

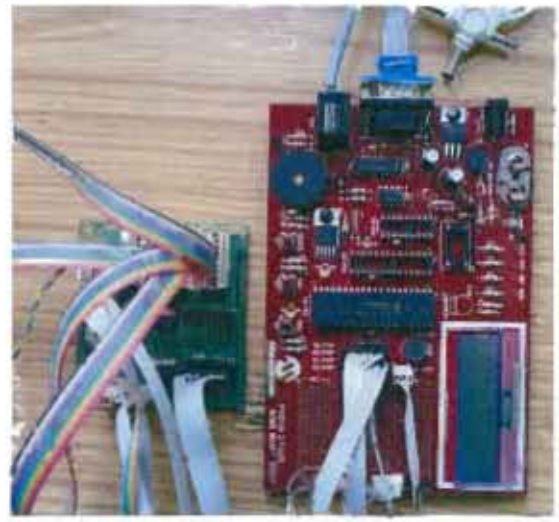

Figure 5.9: Microcontroller demo board and the programmable delay module.

Although the resistor array inside the DS-1020 is laser trimmed to match the designed values, there will still be a variation of the generated delay time from the nominal delay time, i.e. the delay programmed into the delay line. A set of measurements were done using an accurate digital oscilloscope (Agilent Infinium 54833A DSO) to characterize the observed (measured) delay as a function of the programmed (nominal) delay. Figure 5.10 and Figure 5.11 compares the measured accumulated delay with nominal accumulated delay for DS1020-015 and DS1020-050 respectively.

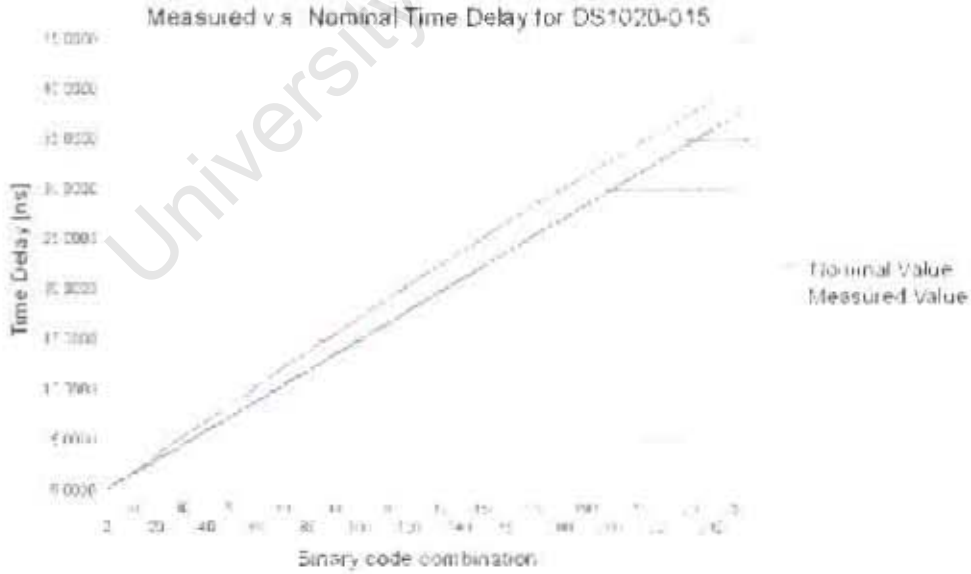

Figure 5.10: Delay time v.s. programmed code for DS1020-015 [1].

The delay time was measured with the DSO by finding the time difference between the input and output of the delay line. The averaged time difference is obtained using the averaging function on the DSO, over 2,000,000 pulses. There is an initial delay of 10 ns for each of the delay element, which is not shown in Figure 5.10 and Figure 5.11. The

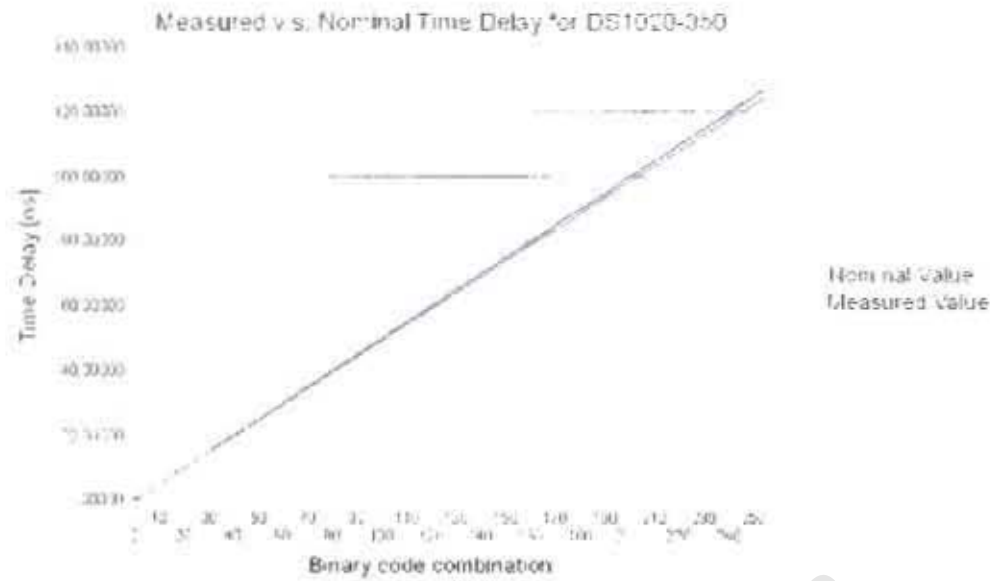

Figure 5.11: Delay time v.s. programmed code for DS1020-050 [1].

measured delay is relatively close to the nominal delay value, with a constant error in each step. Since the slope of the graph shown in Figure 5.10 is fairly smooth, it suggests that each delay step size is constant. The time delays represent the sampling points on the return echoes. Hence, the constant delay step size ensures the return echoes are uniformly sampled. However, since actual delay step size is slightly larger than 0.5 ns (the slope is steeper), it suggests that the sampling frequency slightly lower than 6.67 GHz.

5.2 Trigger generator

The trigger generator is responsible for switching on the sampler module for a short duration (typically $\leq$ 1ps), which defines the sample 'window'. The input of the trigger generator is a delayed square wave, in which the time delay is set by the delay line module. Figure 5.12 illustrates the basic operation of the sampler module. Samples are taken at discrete times T_A, T_B, T_c etc. As illustrated in Figure 5.12, the switched-on time of the sampler module (i.e. the sample 'window') needs to be significantly smaller than the pulse width of the transmitted signal and the delay step size (0.15 ns). This is to ensure that, when the delay is set to T_A, the sampled signal at T_A reflects the true return echo at T_A, and not the averaged signal of the return echo between T_A and T_B.

Figure 5.13 shows the circuit for the trigger generator. This circuit is similar to the circuit design used for the UWB pulse generator. The pulse generated by the transistor is used to switch the sampler module.

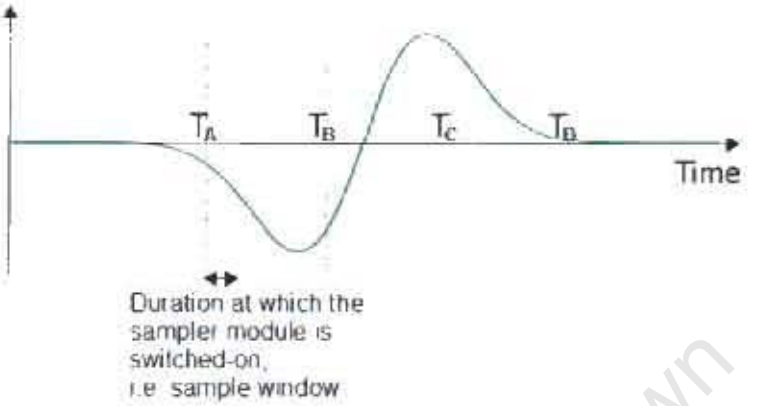

Figure 5.12: The simplified integrating sampler operation.

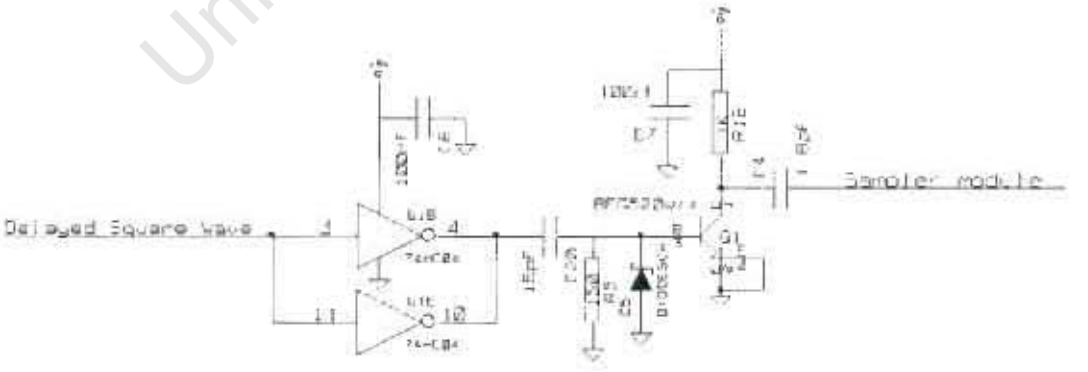

Figure 5.13: Trigger generator circuit.

the discharging time for C21 to reach the new V_{diff}, where $V_{diff} = V_{rx}(t = t_2) + 4.51$ V, is shorter than $\tau_{discharging}$. Figure 5.15 illustrates this operation.

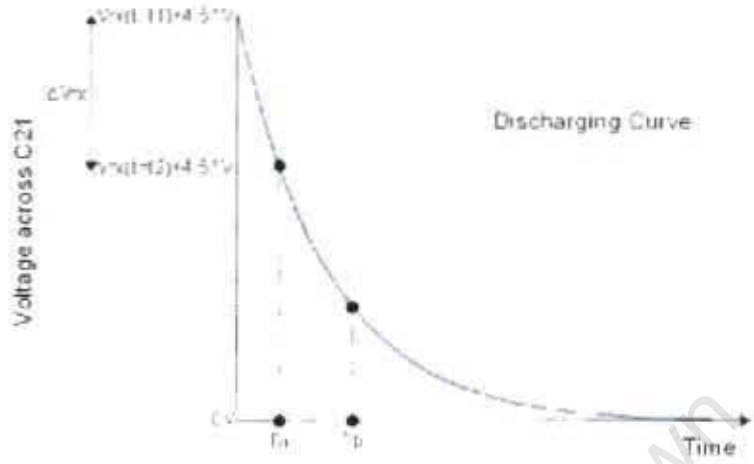

Figure 5.15: Passive discharging curve.

The discharging curve can be expressed as

$$V_{capacitor}(t) = V_{rx}(t = t_1)e^{(-t/RC)}$$

where $V_{capacitor}(t)$ is the voltage across the capacitor, $V_{rx}(t = t_1)$ is the initial voltage across the capacitor and RC is the discharging time constant $\tau_{discharging}$. When V_{rx} is decreased by ΔV_{rx}, the time it takes for the capacitor to discharge to the new value can be calculated as following:

$$V_{rx}(t = t_1) - \Delta V_{rx} = V_{rx}(t - t_1)e^{(-t/RC)} = -\frac{1}{RC}ln(1 - \frac{\Delta V_{rx}}{V_{rx}(t = t_1)})$$

From above equation, it shows that the time requires for C21 to discharge to a new value is related to the ratio between ΔV_{rx}, the change in received voltage, and $V_{rx}(t = t_1)$, the initial voltage across C21. Hence there is no fixed discharge time that can be used to describe the passive discharging time in the case of $\Delta V_{rx} < 0$. Nevertheless, from Figure 5.15, it is clear that the discharging time for C21 is less than the passive discharging time.

Simulations were done using Micro-Cap [48] to confirm the above explanation. Figure 5.16 shows the integrator circuit diagram that is used in the simulation. The trigger pulse is represented by the pulse generator V1. The value for the resistors, capacitors and triggering pulse width are scaled from the actual value that are used in the hardware, due to the limitation of the simulator. Figure 5.17 shows the simulation result. The red waveform represent the V2, the received signal, and blue waveform is the voltage at node R6-R8 and node R7-R9. The simulated results verify the above explanation on the circuit operation.

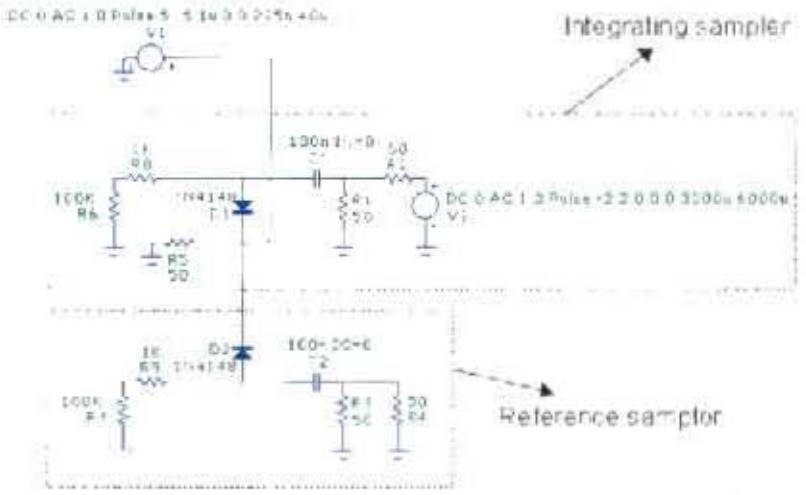

Figure 5.16: Integrating sampler module circuit used in simulation.

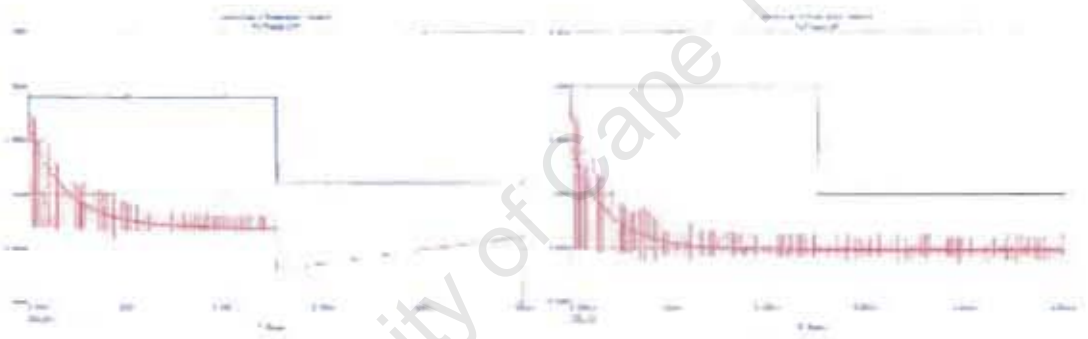

(a) Integrating sampler (b) Reference sampler

Figure 5.17: The simulated output waveform at (a) node R6-R8 (b) R7-R9, and V2, using simulation circuit shown in Figure 5.16.

Since the active charging time is less than the passive discharging time, by resetting the integrating capacitor C21 and C22, the sampler module will always undergo active charging process for both condition of ΔV_{ex}. This is effectively shortening the "discharge" time required for C21 to reach the new V_{ex} when ΔV_{ex} is negative. Analog switch ADG601 is chosen for this application. The two analog switches are placed across C21 and C22. When the delay line slides to a new value, the analog switch will be turned on by the microcontroller, and the capacitor will be discharged through the on-resistance of the analog switch. ADG601 is a dual supply, 2 Ω on-resistance analog switch [18]. Hence the reset time required to discharge the capacitor through the analog switch, is determined by the time constant $\tau_{reset} = C \times R_{analog\ switch} = 2\text{ns}$.

To verify the reset action, that using analog switch will rapidly discharge the integrating capacitors, experiments are conducted by connecting the transmitter directly to the receiver via a coaxial cable and suitable attenuators and acquiring the sampled received

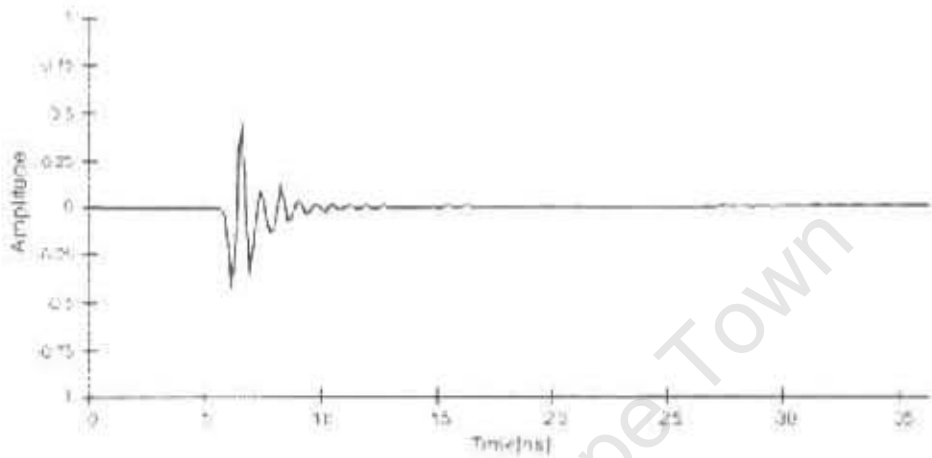

(a) Without reset function

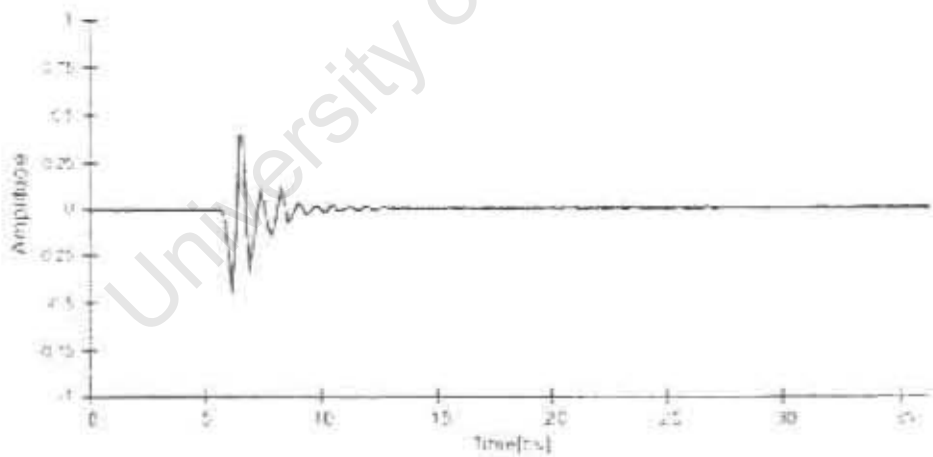

(b) With reset function

Figure 5.18: The transmitted waveform that is sampled by the receiver with (a) no reset (b) reset function, using the analog switches. The integration time is 1250 μs.

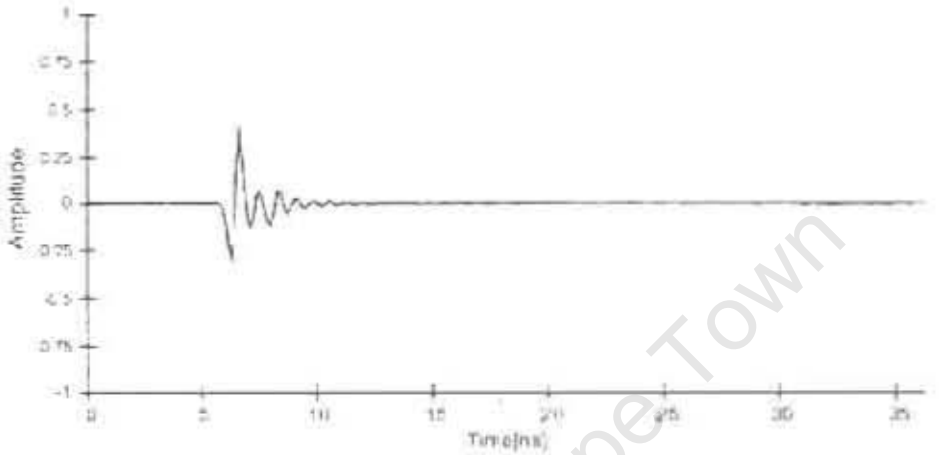

(a) Without reset function

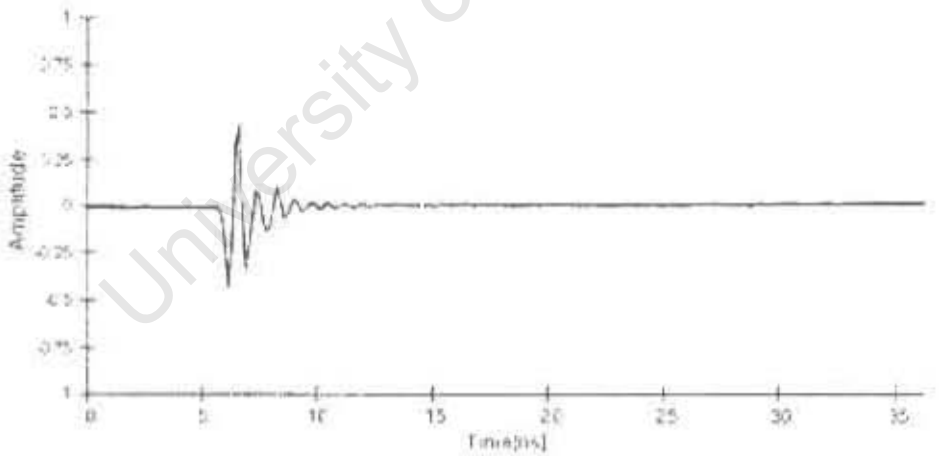

(b) With reset function

Figure 5.19: The transmitted waveform that is sampled by the receiver with (a) no reset (b) reset function, using the analog switches. The integration time is 125 μs.

waveform. Figure 5.18 shows the sampled waveform when the integrating time is set to 1250 μs, i.e. the delay line slides to the next value every 1250 μs. This integrating time is chosen, so that the integrating capacitor will charged to a point where more sampled signal will not increase the charged voltage any further. Hence, Figure 5.18 shows the 'true' received waveform. In this experiment, the sampled waveform for both cases (with/without reset function) are virtually identical - as they should be.

Figure 5.19 shows the sampled waveform when the integrating time is set to 125 μs. From Figure 5.19(a), it shows that the the integrating capacitor is not charged sufficiently to the received signal when the waveform changes rapidly in the negative direction (i.e. $\Delta V_{rx} < 0$). The new sampler with reset function produces Figure 5.19(b), which resemble the sampled waveform in Figure 5.18(b). Thus the new sampler with reset function will allow much faster range profiling than the original circuit. In practice, 500 μs dwell time was used per step.

5.4 Post-amplifier module

The post-amplifier module contains two stages of amplification: instrumentation amplifier AD620 and operation amplifier TL092.

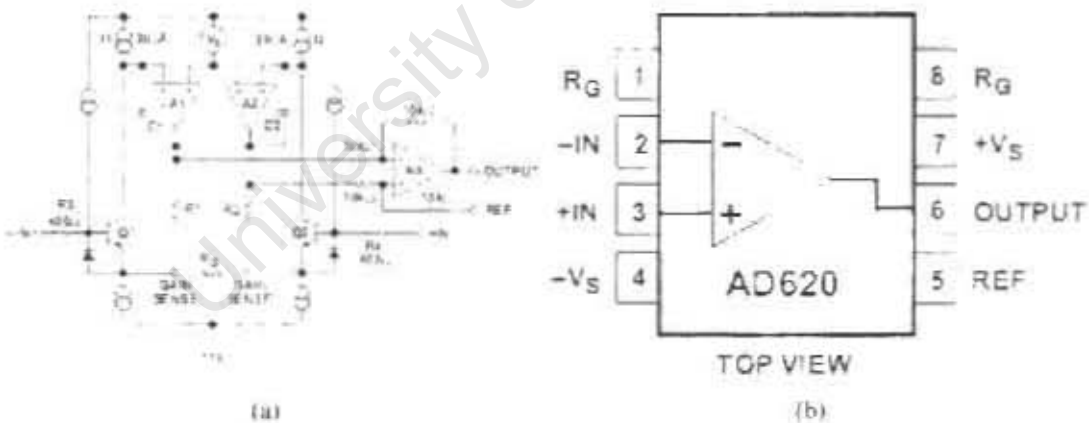

Figure 5.20: (a) Simplified circuit diagram (b) Block diagram of AD620 [12].

The two branches of sampler module, the integrating sampler and the reference sampler, are connected to +IN and -IN pins of the instrumentation amplifier AD620, where the voltage difference between the two pins is amplified and rectified to appear as a DC offset at the output. Figure 5.20 shows the simplified circuit diagram and the connection block diagram for AD620, which is reproduced from [12]. A low pass filter structure is required to place in front of +IN and -IN pin to minimize the RF interference from being amplified. Figure 5.21 shows the circuit diagram for the low pass filter, which is suggest by [12]. The

filter cut-off frequency is determined by

$$f_{\text{cutoff}} = \frac{1}{2\pi R(2C_D + C_C)}$$

where the value for C_D needs to be at least 10 times larger than C_C , to ensure that the common-mode rejection performance that is designed for AD620 is not diminished [12]. Since the delay line is slid at rate of 500 μs per step, the minimum cut-off frequency of the low pass filter is 2 KHz. The cut-off frequency of the low pass filter is set to 23 kHz. This allows a choice of faster sweeping rate to be used for future development. The component value used in the filter are $R = 150\text{k}\Omega$, $C_D = 22\text{pF}$ and $C_C = 1.5\text{pF}$.

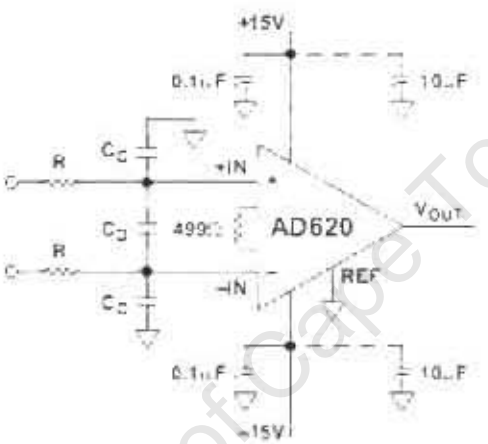

Figure 5.21: Circuit diagram for filtering RF signal [12].

The gain of AD620 is determined by ratio of the internal gain resistors and R_G, where R_G is the external resistor connected between the two R_G pins. The gain of the amplifier is calculated by:

$$G = \frac{49.4k\Omega}{R_G} + 1$$

Figure 5.22 shows the gain v.s. frequency graph for AD620. In this thesis, the gain of AD620 is set to 16. Figure 5.23 shows the circuit diagram for the post-amplifier module.

TL092 (U9A) is used for level shifting and adjusting the signal amplitude before the sampled signal is digitized by the ADC. As the input range to the ADC is limited between 0 and 5 V, the output signal of the AD620 needs to be level shifted to 2.5 V. The gain of TL092 is adjusted by turning the potentiometer R16.

5.5 Front-End Amplifier

A 'front-end' amplifier is required to amplify the return signal before the sampling process. Through pre-amplification, the overall SNR of the sampled signal is increased.

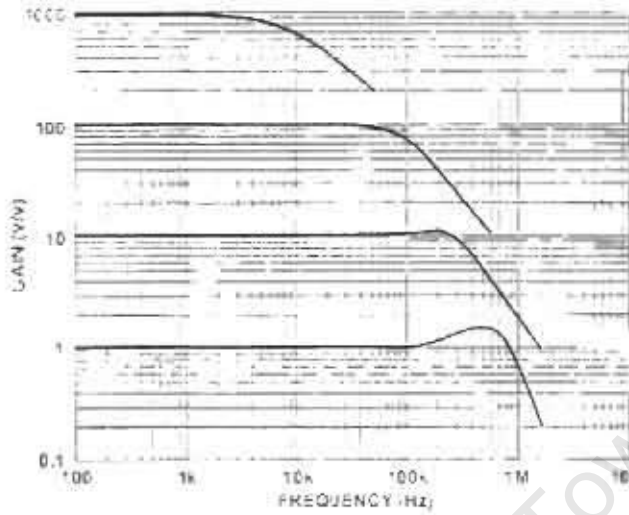

Figure 5.22: Gain v.s. frequency graph for AD620 [12].

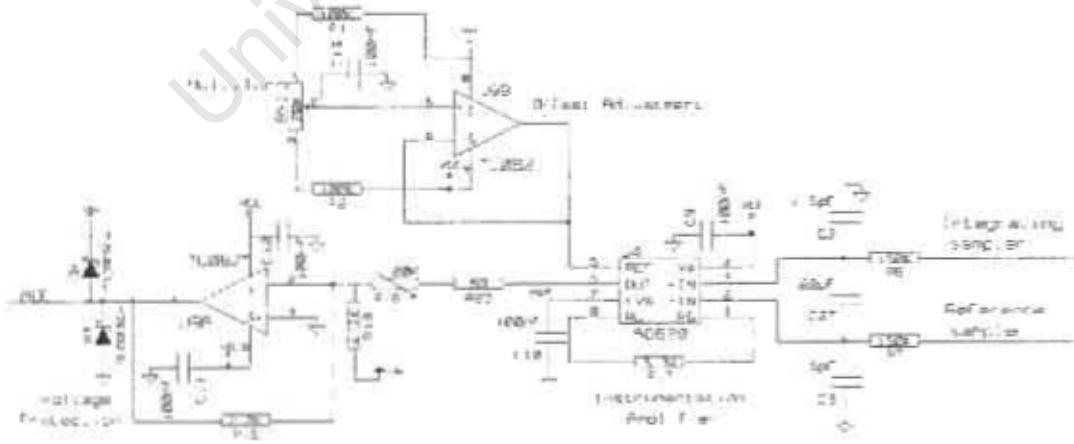

Figure 5.23: Circuit diagram for the post-amplifier module.

which increases the chance of detecting a weak target response. Furthermore, the amplified signal is less susceptible to the noise and distortion from the later sampling stages. For the UWB system, the front-end amplifier needs to be low noise and have a flat gain response over a large bandwidth.

Gali-39+ from Mini-Circuits was chosen for this application, as it operates from DC to 7 GHz, with 19.7 dB gain at 2 GHz. Gali-39+ has a low noise figure of 2.4 dB (noise temperature of 214 kelvin) at 2 GHz, which is lower than the room noise of around 290 kelvin. Figure 5.24 shows the noise figure and gain of the amplifier over the operating frequencies.

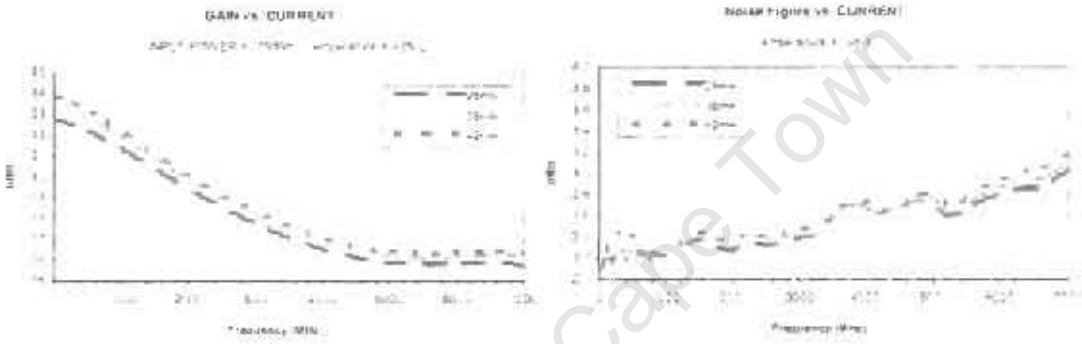

(a) Gain (b) Noise figure

Figure 5.24: Graph shows (a) gain (b) noise figure over the operating frequency [15].

Figure 5.25 show the connection for Gali-39+ amplifier. Gali-39+ is designed to operate at 3.5 V with 35 mA, for a optimal performance of high gain and moderately low noise. Therefore, resistors are required for biasing the 15 V supply to 3.5 V. The biasing resistance needed is approximately $\frac{15-3.5}{0.035} \approx 340\,\Omega$. The power dissipated in the bias resistors is approximately 0.39 W. Hence two 0.25 W resistors, 160 Ω and 180 Ω, are used in series to overcome the power dissipation limit. The AC coupling capacitors, 2.4 nF [14], are placed at the input and output of the amplifier, which are used to block the DC component from entering the device. A biasing choke inductor is required to place between the output of the amplifier and the bias resistor, to prevent the RF signal from interfering with the supply source [13]. The inductor used in Figure 5.25 is a 68 nH from Coilcraft 0603CS series. The measured inductance at 1.7 GHz is approximately 168 nH [9].

Figure 5.26 shows the front-end amplifier test board. Five vias are placed around the amplifier to connect the top and bottom ground place, which ensures the RF signal would be properly guided in and out of the device [11]. Figure 5.27 shows the output waveform of the amplifier when a -10 dBm sinusoidal signal, at 1 GHz, is input to the amplifier. The sinusoidal signal is generated by Agilent E4400B signal generator. The -10 dBm signal is measured on the DSO, with the input impedance of the DSO set to 50 Ω. The measured

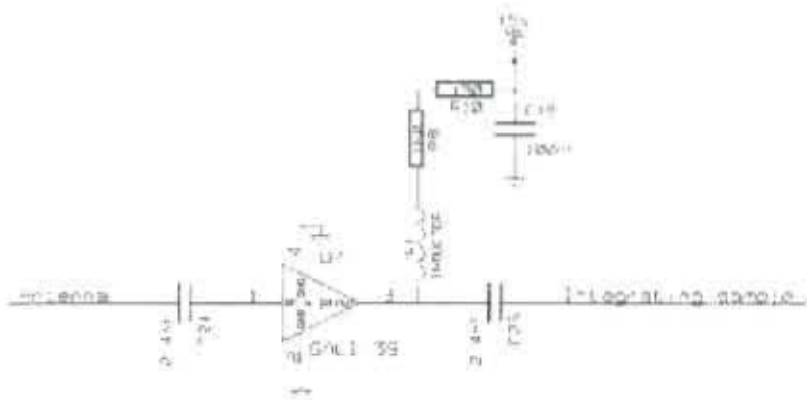

Figure 5.25: Front-end amplifier connection circuit diagram.

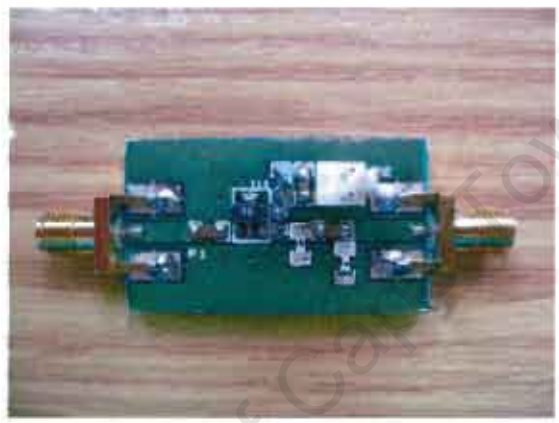

Figure 5.26: Front-end amplifier test board.

peak-to-peak voltage is approximately 147 mV. The output signal, shown in Figure 5.27, is approximately 1.67 V. Hence the gain of the amplifier, at 1 GHz, is approximately 21.1 dB. This agrees with the result shown in Figure 5.24(a). In this thesis, two Gali-39+ are cascaded to provide 40 dB gain at 1.5 GHz.

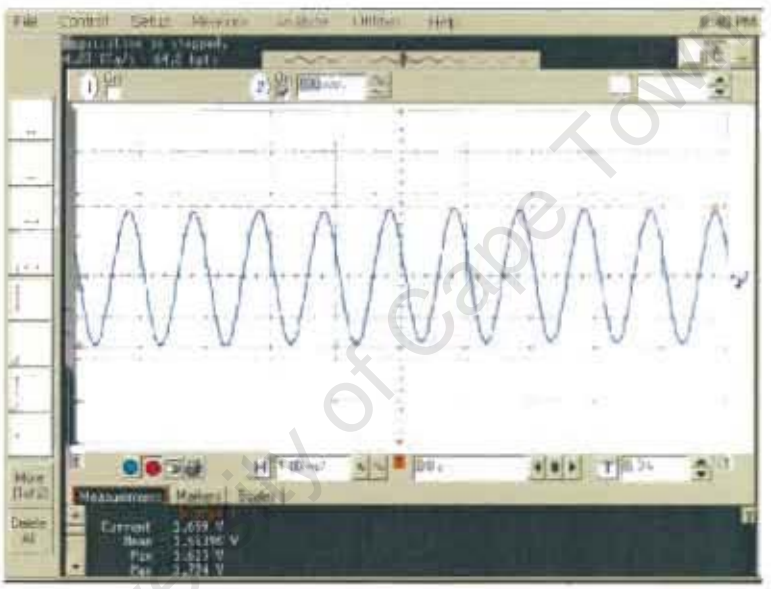

Figure 5.27: Signal measured at the output of Gali-39+. A 1 GHz sinusoidal is inject into the amplifier.
Vertical scale: 500 mV/div (with 0 V offset)
Horizontal scale: 1 ns/div

Chapter 6

Simulation

Simulation of the UWB array and the image formation algorithms were implement using Python. In this chapter, the result from each stage of signal processing will be presented. Finally, a simulation of imaging multiple targets will be performed.

The transmitted signal is simulated using the first derivative of a Gaussian pulse [49], which is expressed as

$$V_{Tx}(t) = A\frac{t}{\tau}e^{-(\frac{t}{\tau})^2}$$

where τ is the pulse width and A is a amplitude scaling factor. In the simulation, the pulse width is set to $\tau = 0.5$ ns and $A = 1$. The 3 dB bandwidth of the pulse is approximately $B = \frac{1}{\tau}$, which is equivalent to 2 GHz. Figure 6.1 shows the simulated pulse in time domain and frequency domain.

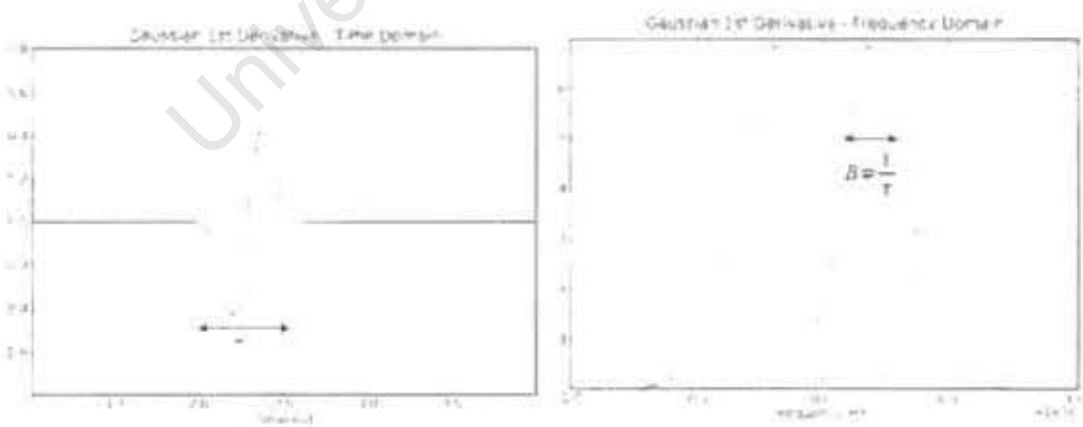

(a) Time domain (b) Frequency domain

Figure 6.1: Simulate transmitted waveform.

In Chapter 7, the experiments were conducted using two bow-tie antennas, which operate between 1 to 2 GHz. In order to simulate the real received data, the simulated signal is band-limited to 1 GHz (frequency component from 1 GHz to 2 GHz). Furthermore, most

of the system parameters used in this simulation are the same as the real system hardware condition.

The parameters used in the simulation are summarized at below

- Centre frequency $f_c = 1.5\,\text{GHz}$
- Bandwidth = 1 GHz (frequency component from 1 GHz to 2 GHz)
- Sampling frequency $f_s = 24\,\text{GHz}$. Figure 6.1 shows that an impulse with pulse width = 0.5 ns has frequency components up to 6 GHz. Hence, a sampling frequency of 24 GHz is required to sample the highest frequency component of the impulse. In the real system, the received signal is bandlimited by the antennas that were used to transmit and receive the signal, before it is sampled by the receiver. Hence a lower sampling frequency (≈ 6.67 GHz) is sufficient.
- Spacing between the receiver elements $d = 0.15\,\text{m}$
- Number of receiving elements $N = 8$.
- Maximum detection range $R_{\max} = 19.2\,\text{m}$
- Angular field of view $2\theta_{\max} = 2arcsin(\frac{\lambda}{2d}) = 83.6^{\circ}$
- Angular resolution $\theta_{3dB} \approx \frac{\lambda}{Nd} = 9.6^{\circ}$ (without aperture weighting)

6.1 Effect of Signal Processing

Figure 6.2 shows the position of the transducer elements and the target. A single target is placed 10 m away from the radar. Figure 6.3 shows the transmitted and received waveform for the first receiving element in the array. The received signal is a time delay version of the transmitted signal. The time delay for each received signal is equivalent to the time required for the transmitted signal to reach the target and return to the receiving element. The amplitude of the received signal is compensated with r^2 algorithm. Therefore, the received signal has same amplitude as the transmitted signal.

Signal processing, using either a matched filter and an inverse filter, is performed on the received signal. Both filter suppress the out-of-band noise and boost the in-band signal, which improves SNR. The magnitude of the FFT's of both filters are shown in Figure 6.4. The FFT of the matched filter is the conjugate of the FFT of the transmit waveform, and the FFT of the inverse filter is the inverse of the FFT of the transmitted waveform. Since the inverse filter is only defined over a bandwidth (refer to Section 3.4.2), a *rect* function

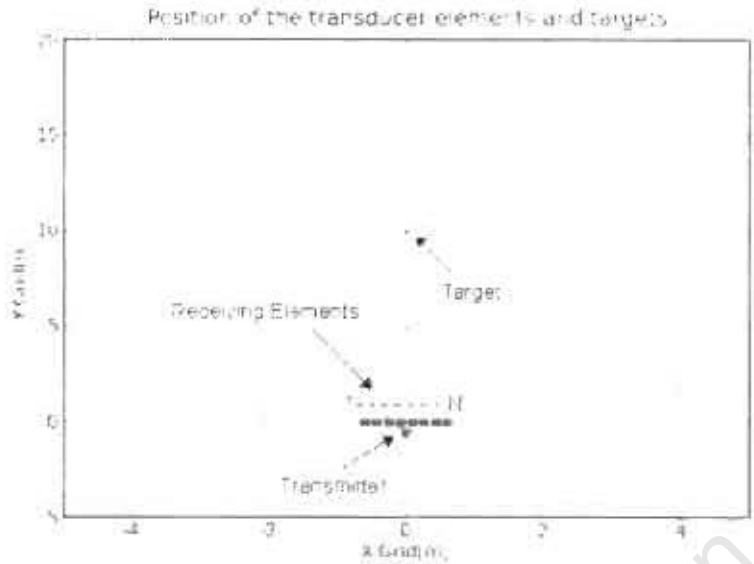

Figure 6.2: Position of the transducer elements and target.

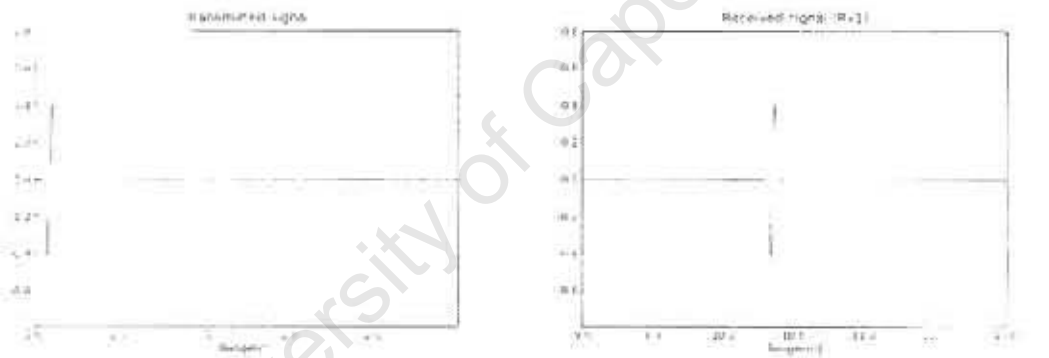

(a) Transmitted waveform (b) Received waveform at the first received element

Figure 6.3: Transmitted and received waveform.

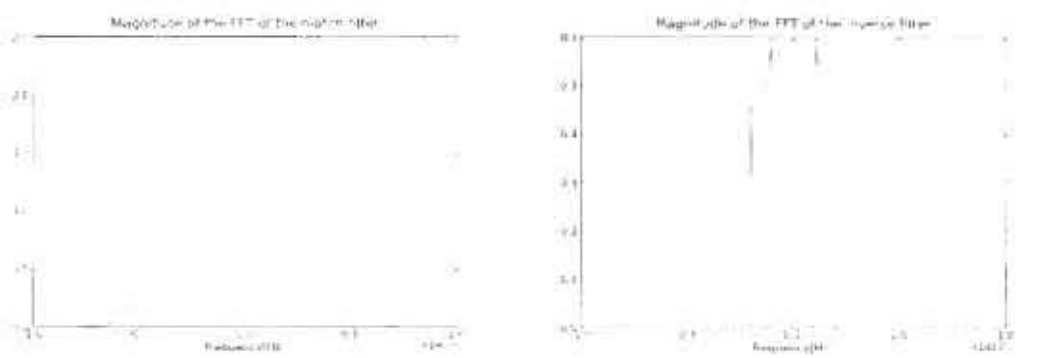

(a) Matched filter (b) Inverse filter

Figure 6.4: The magnitude of the FFT of the (a) matched filter and (b) inverse filter.

with bandwidth of 1 GHz (frequency component from 1 GHz to 2 GHz), is used to band-limited the frequency spectrum of the signal.

Figure 6.5 and Figure 6.6 show the analytic representation of the the matched filtered and inverse filtered signal respectively.

Any real signal has a two-side Fourier transform that are in symmetry. A real signal $x(t)$ has a spectrum where $X(-f) = X^*(f)$ [22]. The analytic representation of a real signal $x(t)$ is defined as having only the positive frequency components [22].

$$X_{\text{analytic}}(f) = \begin{cases} 2X(f) & f \geq 0 \\ 0 & f < 0 \end{cases}$$

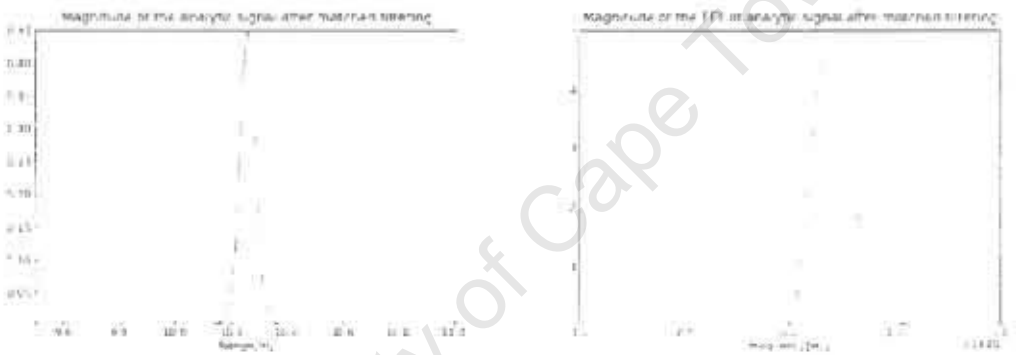

(a) Time domain (b) Frequency domain

Figure 6.5: The envelop of the matched filtered signal.

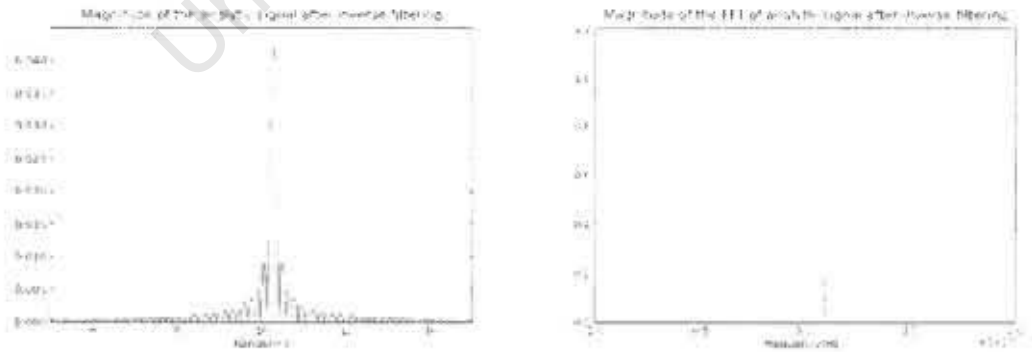

(a) Time domain (b) Frequency domain

Figure 6.6: The envelop of the inverse filtered signal.

The magnitude of the frequency spectrum of the inverse filtered signal (from a point target) is a *rect* function. Hence, in time domain, this is transformed to a $\frac{\sin(x)}{x}$ function.

The high side-lobes observed from Figure 6.6(a) can be reduced by reshaping the frequency spectrum of the inverse filtered signal [22]. A window function, such as Hanning window and Blackman window, can be used for this purpose. The result is shown in Figure 6.7. Comparing to Figure 6.6(a), the side-lobes in Figure 6.7(a) are significantly reduced.

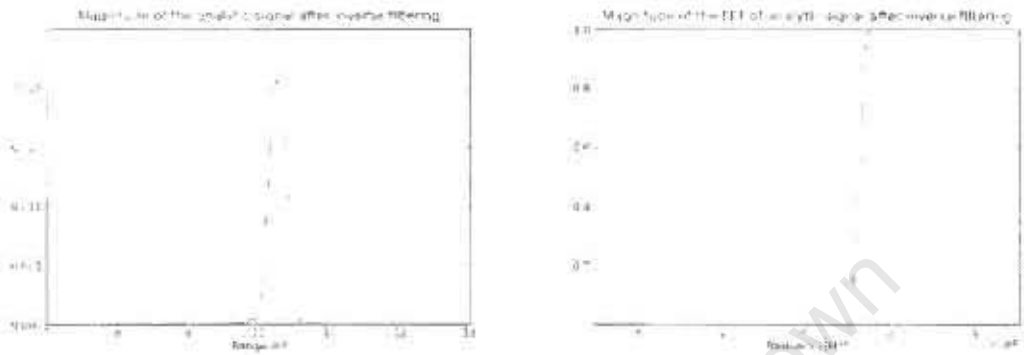

(a) Time domain (b) Frequency domain

Figure 6.7: The envelop of the inverse filtered signal when Hanning window is applied.

The spectral components of the filtered signal is then basebanded by multiplying the signal with $e^{-j2\pi f_c t}$ in the time domain [22]. Figure 6.8 shows the basebanded signal after using matched filtering and inverse filtering. The centre frequency is chosen as $fc = 1.5$ GHz. Unlike the inverse filtered signal, the matched filtered signal is not bandlimited. Hence, the basebanded matched filtered signal has a two-side Fourier transform that are not symmetrical. Thereafter, the beamforming algorithm, which is described in Section 3.4.3, is applied on the basebanded signal (for both matched filtered and inverse filtered signal) to produce an image which reveals the range and angular position of the target. Figure 6.9 shows the beamformed image in the case of matched filtering and inverse filtering, which is applied to the range profiles, respectively.

The beamformed images observed in Figure 6.9 have large side-lobes in the azimuth direction. The side-lobes can be reduced by applying a Hanning aperture weighting to each of the receiving elements when summing the signals for a focused point. Figure 6.10 shows the beamformed image of the inverse filtered (with Hanning window) range profiles, with a Hanning aperture weighting applied. In general, the side-lobes are reduced through window functions in range and azimuth direction. However, the main-lobe is widened in the process. Figure 6.10(b) is the beamformed image display in a fan-beam formation. This is obtained by mapping the result from Figure 6.10(a) into Cartesian coordinates.

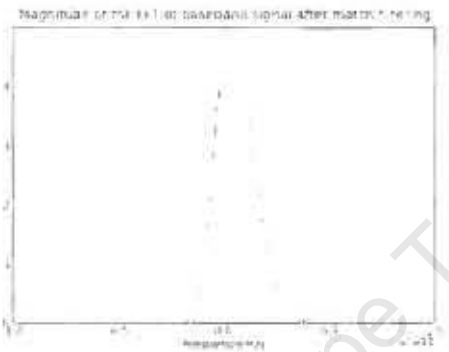

(a) Matched filtering

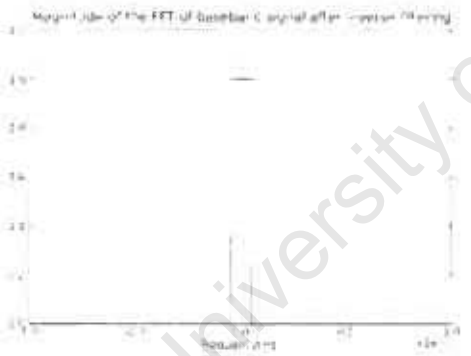

(b) Inverse filtering with rect window

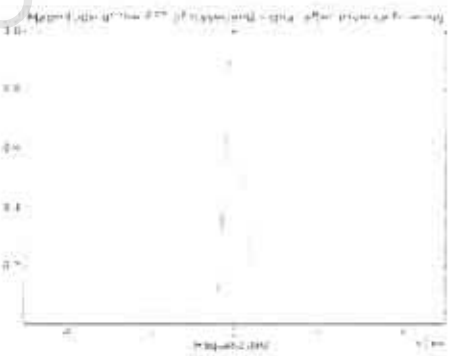

(c) Inverse filtering with hanning window

Figure 6.8: The magnitude of the basebanded signal, after (a) matched filtering, (b) inverse filtering with application of rect window, and (c) inverse filtering with application of Hanning window.

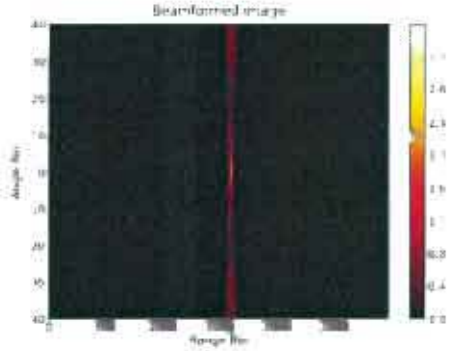

(a) Result from matched filtered range profiles

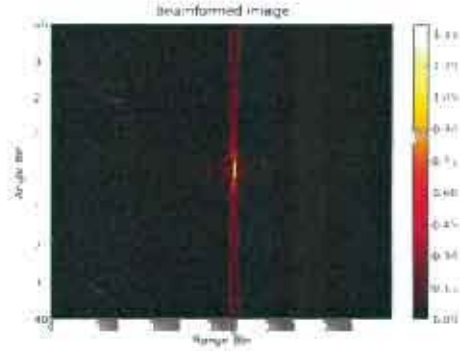

(b) Result from matched filtered, with rect window applied, range profiles

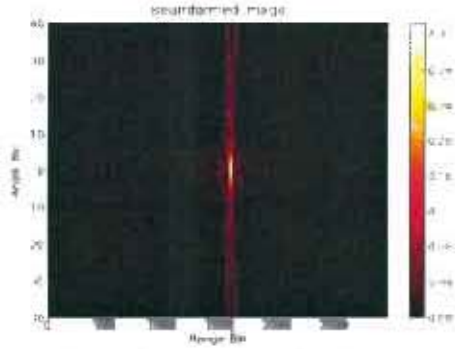

(c) Result from inverse filtered, with rect window applied, range profiles

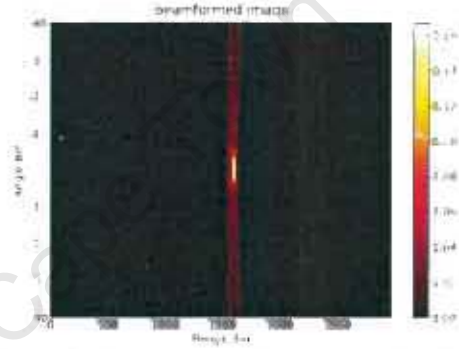

(d) Result from inverse filtered, with Hanning window applied, range profiles

Figure 6.9: Beamformed image in the case of matched filtering and inverse filtering, with no aperture weighting.

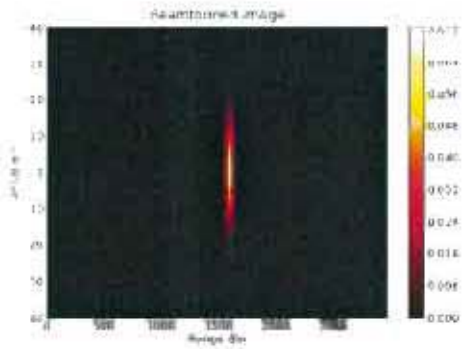

(a) Beamformed image

(b) Fan-beam image

Figure 6.10: Beamformed image when Hanning aperture weighting is applied to the Hanning-windowed, inverse filtered signal.

6.2 Multiple Targets Detection

In this simulation, six targets are placed in front of the radar, with target 1 and target 2 spaced 15 cm away from each other. Inverse filtering, with Hanning window, is applied to each of the 8 range profiles (as there are 8 receiving elements), and a Hanning aperture weighting is used to focus the basebanded inverse filtered signals. Figure 6.11 shows the comparison between the actual location of the targets, and the focused fan-beam image of the processed result. The result from the fan-beam image gives a close approximation to the location of the targets. The angular resolution can be improved by increasing the length of the array, which requires introducing additional elements if the angular ambiguities (grating lobes) are not to be affected.

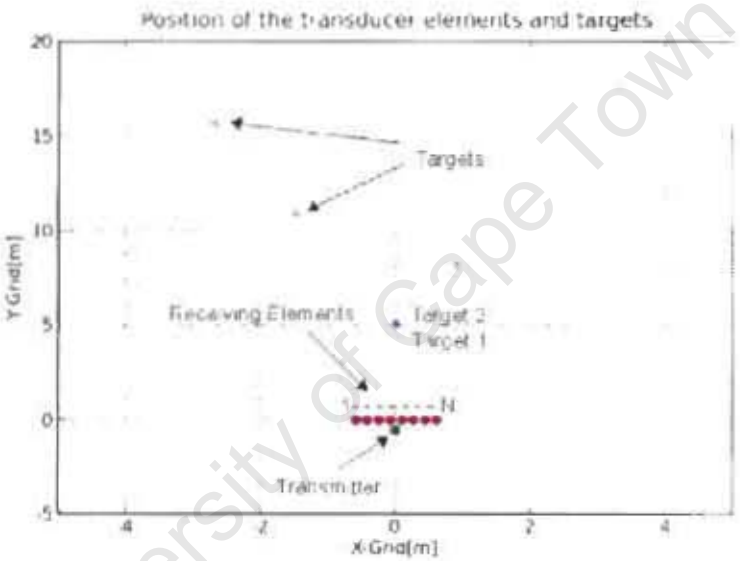

(a) Location of targets

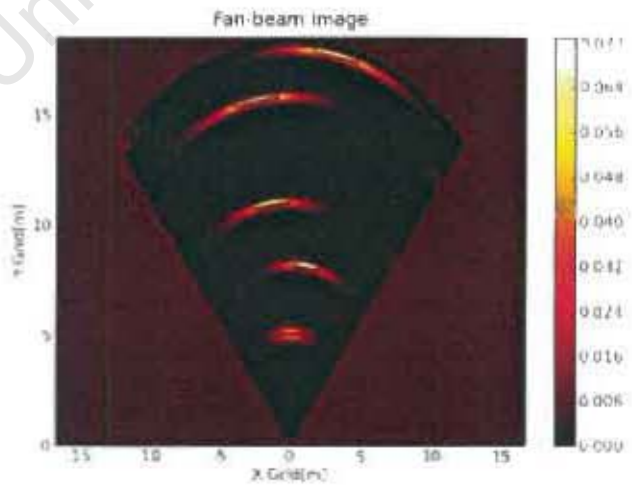

(b) Fan-beam image

Figure 6.11: Comparing the processed result with the position of the target specified initially

Chapter 7

Results

In this chapter, the performance of the UWB system hardware is examined and various target detection scenarios are investigated.

The system hardware performance is examined from three aspects:

- Noise characteristics along the various points in the receiver circuit.
- Stability over time
- Signal-to-noise ratio of the system, before and after signal processing.

In the target detection section, the ability of the UWB radar for detecting targets with different types of material and for resolving close-by positioned targets is examined. Later, imaging is performed using a four element UWB receiver array. Table 7.1 shows the target objects that are used in the experiments.

7.1 UWB antennas

Two types of antenna are used in this thesis. The first type of antenna is the bow-tie antenna. Figure 7.1 shows the two bow-tie antennas that were built by an undergraduate thesis student in 2004. These antennas are designed to operate between 1 and 2 GHz [38, 57].

In order to examine the antenna's frequency response, S11 and S21 measurement, using network analyzer, were performed on the bow-tie antenna, which are shown in Figure 7.2. The two bow-tie antenna are held 2 m apart. Figure 7.2 shows that, in the operating frequency range of 1 to 2 GHz, the return loss of the bow-tie antenna is between -5 dB and -20 dB. The transmission gain is approximately -22.5 dB. However, the gain is not constant between 1 and 2 GHz, where the gain starts to decrease at 1.6 GHz. The 3 dB

Target	Photo	Dimension(mm)
Small Metal Grid	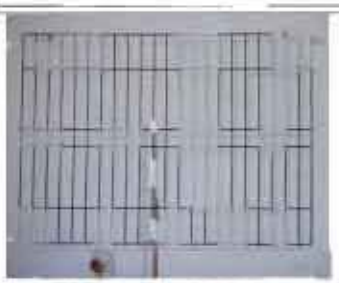	550x390
Large Metal Grid	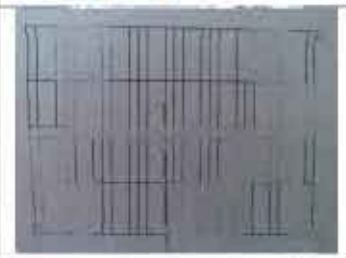	830x590
Corner Reflector		500 per side

Table 7.1: Metal objects used in the experiments.

bandwidth of the antenna is approximately 1 GHz.

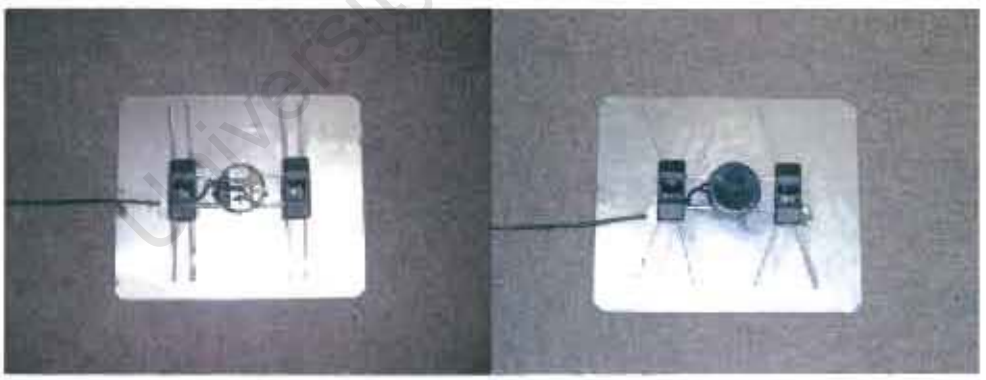

(a) Flare angle smaller than 40 degree (b) Flare angle greater than 40 degree

Figure 7.1: Two bow-tie antennas made by [38]. Photograph reproduced from [57].

The second type of antenna is the Vivaldi antenna. It is a special case of a tapered slot antenna with an exponential taper profile [44]. The Vivaldi antennas have large bandwidth. In addition, the Vivaldi antennas are light weighted and can be easily fabricated using printed circuit board technology. These key factors make Vivaldi antenna a desirable antenna to use in this thesis. Several Vivaldi antennas were acquired from a previous project carried out within our department. These could be used to form an array.

(a) S11 (b) S21

Figure 7.2: (a) S11 and (b) S21 measurements of two bow-tie antennas facing each other at 2 m apart. The two markers in (b) are located at 1 GHz and 2 GHz.
Frequency range (x-axis): 300 kHz to 8.5 GHz
Vertical axis (a): -50 to 50 dB (10 dB/div)
Vertical axis (b): -70 to 30 dB (10 dB/div)

Figure 7.3 shows the Vivaldi antenna used in this thesis and Figure 7.4 shows the S11 and S21 measurement performed by using two Vivaldi antenna aiming at each other, which is placed at 2 m apart. Figure 7.4 shows that the transmission gain is approximately -30 dB, in the frequency band of 800 MHz to 1600 MHz, and approximately -40 dB transmission gain in the frequency band of 2 GHz to 7 GHz. The Vivaldi antenna has a return loss of better than 10 dB for all frequency above 1 GHz, showing that it is well matched to 50 Ω over its working range.

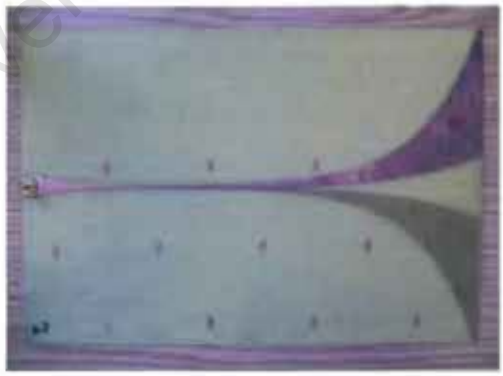

Figure 7.3: A Vivaldi antenna.

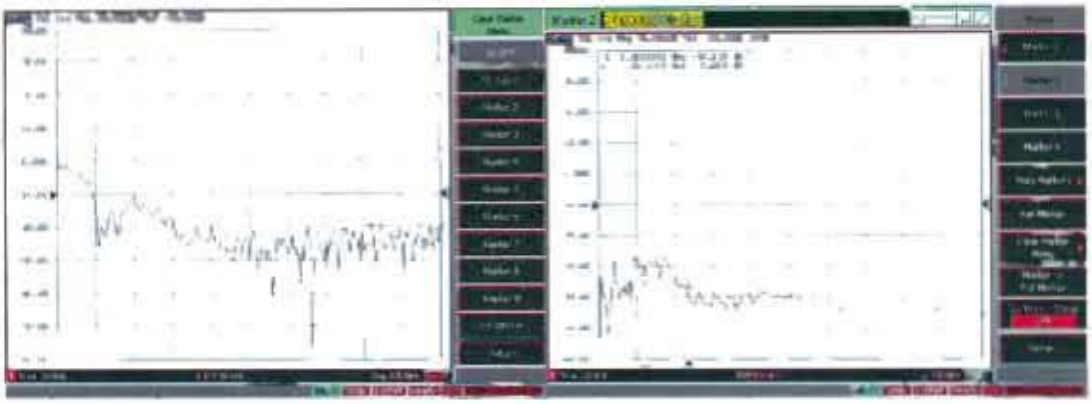

(a) S11 (b) S21

Figure 7.4: (a) S11 and (b) S21 measurements of two Vivaldi antennas facing each other at 2 m apart. The two markers in (b) are located at 1 GHz and 2 GHz.
Frequency range (x-axis): 300 kHz to 8.5 GHz
Vertical axis (a): -60 to 40 dB (10 dB/div)
Vertical axis (b): -60 to 40 dB (10 dB/div)

7.2 System Performance Measurements

7.2.1 Noise Measurement of the UWB Receiver

In the UWB radar system, the echo from a target is often buried inside the thermally radiated noise from the scene. Hence, it is important to minimize the noise within the receiver circuit at least to a level below the thermally radiated noise from the scene. For most indoor imaging applications, the receiving antennas observe objects at room temperature, around 300 kelvin.

Noise measurements are performed along the various points in the UWB receiver circuit. The test points are illustrate in Figure 7.5. This experiment is aimed to identify the dominant noise factor within the receiver, which is useful for future development.

At each stage of the experiment, a different condition is placed on the test points shown in Figure 7.5. The result from each stage is obtained by measuring the output of the ADC module. The output of the ADC is recorded in a frame-style, where each frame consists of 240 sample points, and each sample point corresponds to a 0.15 ns time step. This is equivalent to a range profile of $\frac{c \times 240 \times 0.15 \times 10^{-9}}{2} = 5.4\,\text{m}$. The output of ADC is recorded at a rate of two frames per second, and a total of 500 frames are recorded per each stage of experiment for each test point.

In the first stage of the experiment, test point 1 (input of the ADC module) is connected to a 2.2 V DC supply. The DC supply is decoupled with 150 nF and 15 nF capacitors to remove any possible oscillation and noise in the supply. Figure 7.6 shows the mean and

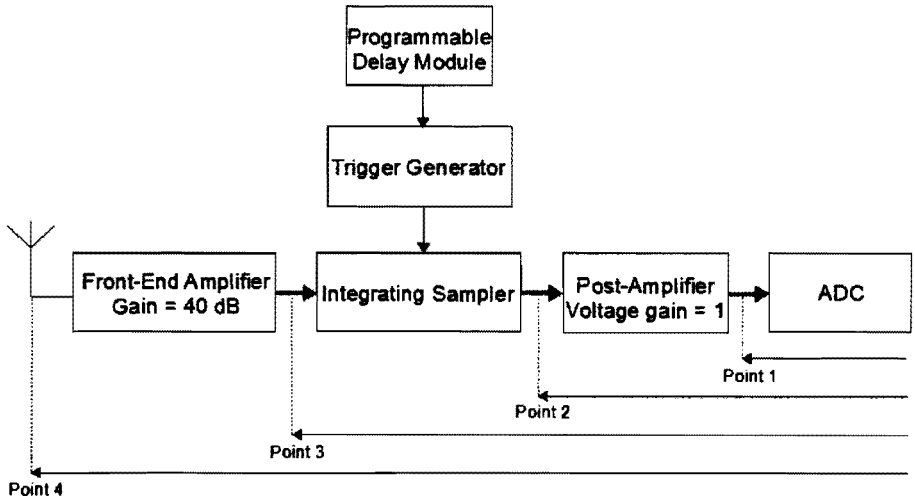

Figure 7.5: The test points in the UWB receiver circuit, which are used for the noise measurements.

the standard deviation of the ADC output voltage, calculated using 500 frames.

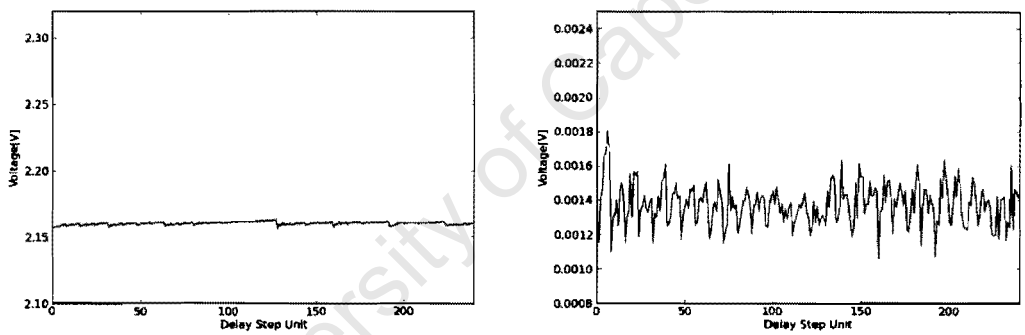

(a) (b)

Figure 7.6: The (a) mean and (b) standard deviation of the ADC output voltage, where the input of the ADC module (test point 1) is connected to a 2.2 V DC supply.

In the second stage of the experiment, the post-amplifier module is connected in front of the ADC, with an offset of 2.5 V added to the ADC. The inputs of the amplifier (test point 2) are connected to the ground. The effective gain of the post-amplifier module is set to one. Figure 7.7 shows the averaged and standard deviation result.

In the third stage of the experiment, the sampler module is connected in front of the post-amplifier module. While the input of the reference sampler is connected to the ground via a 50 Ω resistor, the input of the integrating sampler (test point 3) is connected to (1) the ground via a 50 Ω resistor, or (2) a bow-tie antenna, which operates between 1-2 GHz. The antenna is aimed at a brick wall indoors. The waveform recorded at the output of the ADC module represents the response of the input device connected to the integrating sampler. The mean and standard deviation of the recorded waveform are shown in Fig-

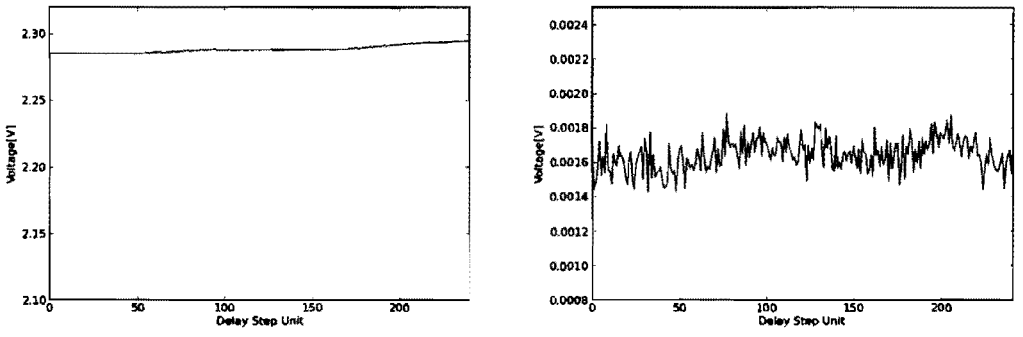

(a) (b)

Figure 7.7: The (a) mean and (b) standard deviation of the ADC output voltage, where the post-amplifier module is attached in front of the ADC, with a 2.5 V offset added to the ADC. The inputs of the post detection amplifier (test point 2) are connected to ground.

ure 7.8 (for the 50Ω resistor) and Figure 7.9 (for the bow-tie antenna) respectively.

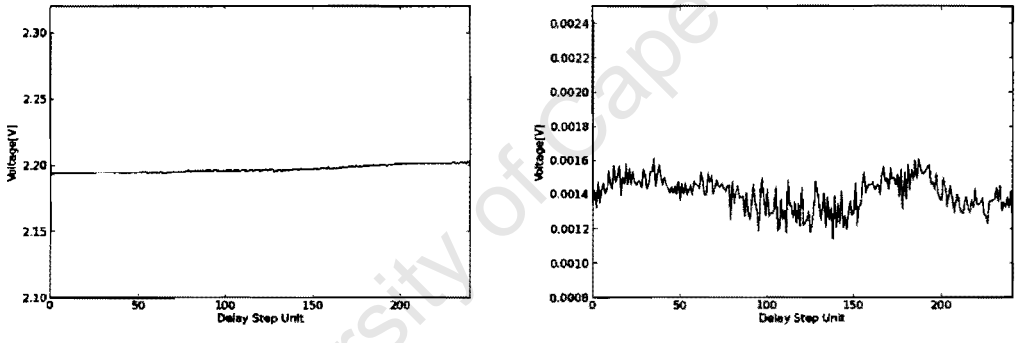

(a) (b)

Figure 7.8: The (a) mean and (b) standard deviation of the waveform recorded at the output of ADC. The sampler module is connected to the post-amplifier, where the input of the sampler module (test point 3) is connected to a 50 Ω resistor.

The noise standard deviations shown in Figure 7.8 and Figure 7.9 have similar value, indicating that the antenna's received noise is similar to that from the 50 Ω resistor.

In the final stage of this experiment, the front-end amplifier module is attached to the sampler module. The input of the front-end amplifier (test point 4) is connected to the bow-tie antenna that is used at the previous stage of the experiment. A total of 40 dB gain is provided by the front-end amplifiers. Hence, the recorded waveform contains the amplified response of the scene (received by the bow-tie antenna) and the noise generated from all the module in the receiver circuit. Figure 7.10 shows averaged and standard deviation of the output waveform. Note that in all these experiments, the transmitter was off.

Table 7.2 summarizes the results obtained at each stage of the experiment (at each of the

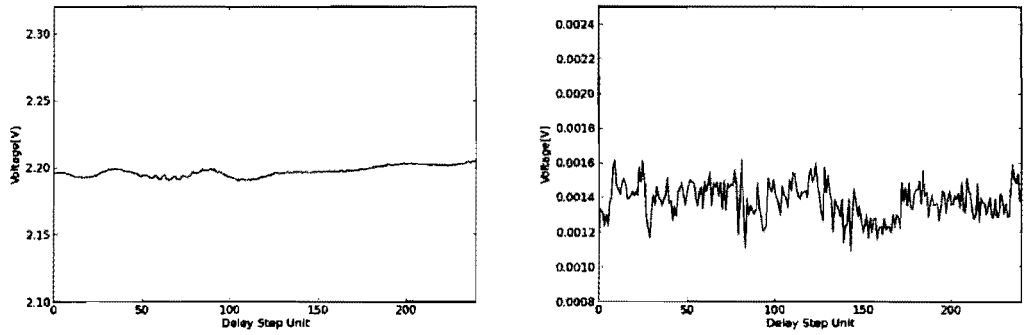

(a) (b)

Figure 7.9: The (a) mean and (b) standard deviation of the waveform recorded at the output of ADC. The sampler module is connected to the post-amplifier, where the input of the sampler module (test point 3) is connected to a bow-tie antenna, which operates between 1-2 GHz.

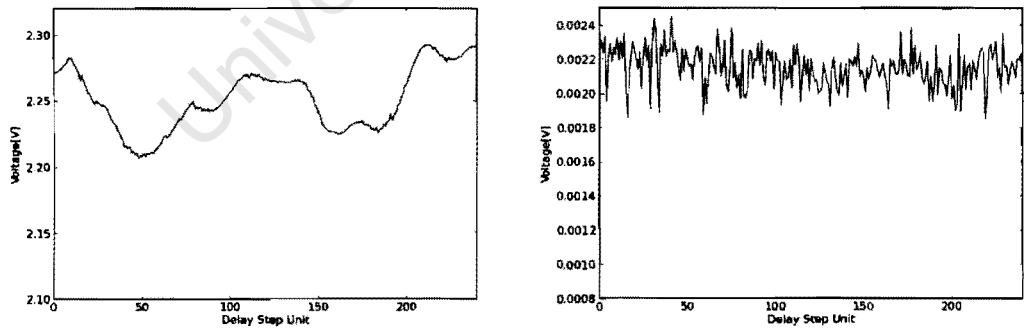

(a) (b)

Figure 7.10: The (a) mean and (b) standard deviation of the waveform recorded at the output of ADC. The front-end amplifiers are connect to the sampler module, where the input of the front-end amplifier (test point 4) is connected to a bow-tie antenna, which operates between 1-2 GHz.

4 points shown in Figure 7.5). $\sigma_{average}$ is the averaged standard deviation measured at each of the 4 points. These results have shown that the front-end amplifier module is the dominant noise factor in the receiver. Furthermore, the front-end amplifier increases the amplitude of the received signal, which makes the distortion caused by the noise in the receiver circuit, less significant. The second dominant noise factor in the receiver is the post-amplifier. However, by adding the sampler module, the noise is significantly reduced. This shows that the sampler can effectively remove the thermally radiated noise presented to the receiver, which otherwise could be amplified by the post-amplifier.

Stage	Stage description	$\sigma_{average}$
First Stage	ADC only	1.38 mV
Second Stage	ADC + post-amplifier	1.64 mV
Third Stage (1)	ADC + post amplifier + sampler (connected to 50Ω resistor)	1.40 mV
Third Stage (2)	ADC + post amplifier + sampler (connected to bow-tie antenna)	1.38 mV
Fourth Stage	ADC + post amplifier + sampler + front-end amplifier	2.16 mV

Table 7.2: Summary of the noise performance at various points in the receiver circuit.

7.2.2 Stability vs Time

This experiment was conducted to examine the drift in the UWB radar system over time. Knowledge about the stability of the system is important, as during the radar operation, a snapshot is taken prior to estimating the background clutter in a testing environment. This background profile is used later to remove the background clutter from the raw target response. If the system drifts significantly over time, the subtraction of background profile taken before the experiment would be unable to remove the background clutter from the raw target response effectively. Details about this operation will be discussed in Section 7.3.

In this experiment, two bow-tie antennas were placed at 30 cm apart, and were attached to the UWB transmitter and the receiver circuit board respectively. The response of the scene was recorded at the rate of one frame (i.e. one range profile) per second. Figure 7.11 shows the system setup for this experiment.

In the first stage of this experiment, the measurement of the scene profile started immediately after the circuits were switched-on, i.e a cold start. Two pre-amplifiers were used, in cascade, in front of the sampler module to provide a total of 40 dB gain. The post-amplifier voltage gain is set to 16. A total of 900 frames are recorded, which corresponds to a measuring period of 15 minutes. Figure 7.12 shows the voltage recorded at the 50^{th} sample point in the scene profile, over a 15 minutes period. From the result shown in Figure 7.12, a temperature related drift is evident over the first 5 minuted period. Hence,

Figure 7.11: UWB radar system with two bow-tie antennas used.

for the target detection experiment, a warm-up period of 5 minutes is required.

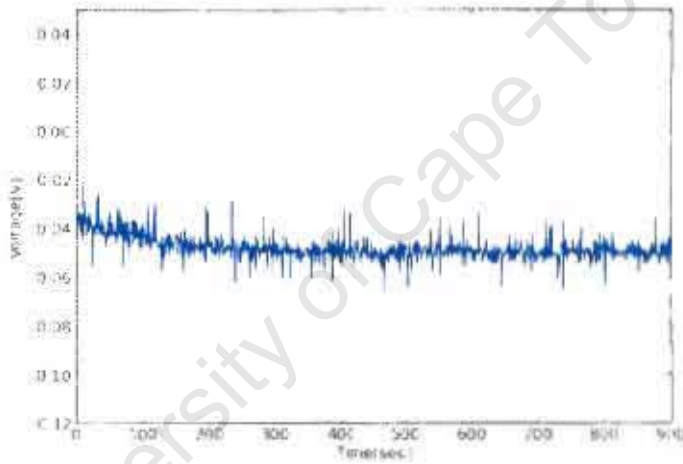

Figure 7.12: The measured voltage at the 50th sample point in the scene profile over a period of 15 minutes. The measurement started immediately after the circuits are switched-on.

In the second stage of this experiment, 900 frames of the scene profile were recorded after a warm-up period, for the electronic circuit, of 30 minutes. The variation of the scene profile over the period of 15 minutes is displayed in Figure 7.13. Figure 7.13 shows only seven of the recorded profiles superimposed, recorded at 3 minute intervals. The drift on this scale is barely visible. The standard deviation of the scene profile was calculated using all 900 profiles and the result is shown in Figure 7.14. The deviation in the signal observed in Figure 7.14 is the thermally radiated noise received by the receiver, as well as the noise of the receiver circuit.

The results, obtained from both figures, show that the recorded profiles remained relatively stable after the electronic circuits have been warmed-up. The calculated standard deviation at the output of receiver is around 5 mV, which is acceptable, considering that

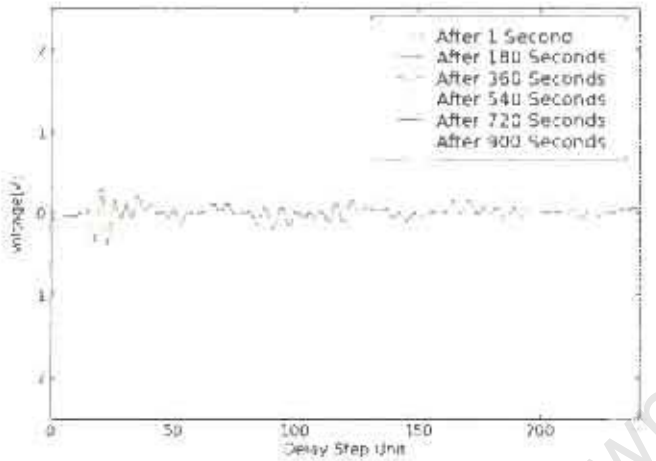

Figure 7.13: This graph shows seven profiles superimposed. The profiles were recorded at every 3 minutes. The responses were recorded after the electronic circuits had warmed-up for 30 minutes.

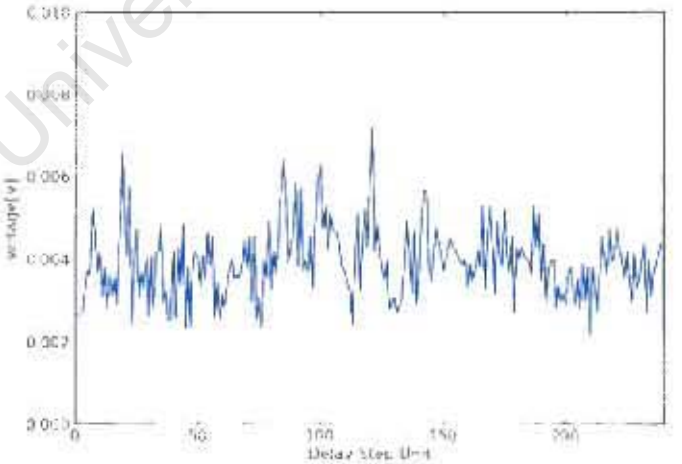

Figure 7.14: The standard deviation of the scene profile over 900 frames, which is captured at one frame per second. The scene profiles are recorded after the electronic circuits have been warm-up for 30 minutes

the test target gave peak-to-peak responses of around 1000 mV, as will be shown in the following sections.

7.2.3 Signal-to-Noise Ratio Measurement

The aim of this experiment is to determine the SNR of the UWB system for typical short range detection applications, before and after signal processing is performed. The SNR can be calculate with

$$SNR = \frac{(V_{\text{rx(pk)}})^2}{(\sigma_{\text{noise}})^2}$$

where $V_{\text{rx(pk)}}$ is the peak voltage of the received signal from a target, and σ_{noise} is the standard deviation of the noise.

In this experiment, two bow-tie antennas were used as the transmitting and receiving antennas (Figure 7.11). At first, a background snapshot of the test scene was recorded. The experiment took place inside a laboratory, where the length of the laboratory is approximately 6 m. Office tables and chairs were situated inside the laboratory in rows. This background profile contains the echoes from the stationary objects, i.e. furniture in the room, as well as random noise. 500 frames of background profile were recorded and averaged. Thereafter, a corner reflector (see Table 7.1) is placed 1.6 m away from the radar, and 500 frames of raw target response are recorded at the rate of 2 frames per second. Figure 7.15 shows the mean and standard deviation of the raw target response and the background profile that was recorded at the start of the experiment.

From Figure 7.15 it shows that the standard deviation peaks at the distance where the corner reflector is situated. Although the corner reflector was placed on a flat stable surface to minimize movement during the experiment, however, the wind blowing into the laboratory and other vibration probably caused it to change its position, hence explaining the peak.

When the background profile is subtracted from the raw target response, the true echo of the target is revealed. This is stored as the reference signal, which will be used in the signal processing in the later stages, as explained in Section 3.4.2. Figure 7.16 shows the reference signal, in time and frequency domain, that will be used in this section. This is the echo of the corner reflector that is placed 1.6 m away from the radar. The spectrum of the reference signal is band-limited by the bow-tie antenna used in the experiment. Hence, the spectral components between 1 GHz and 2 GHz are stronger than the rest of the spectral components.

The peak voltage of the received signal, $V_{rx(pk)}$, measured from Figure 7.16(a), is approximately 0.4 V. The standard deviation of the noise, σ_{noise}, which is measured from

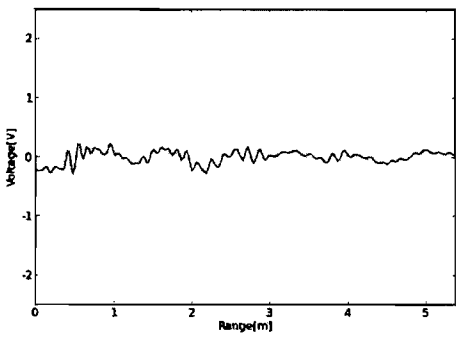

(a) Averaged background profile

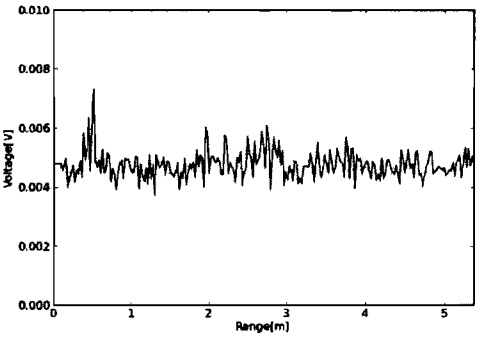

(b) Standard deviation of background profiles

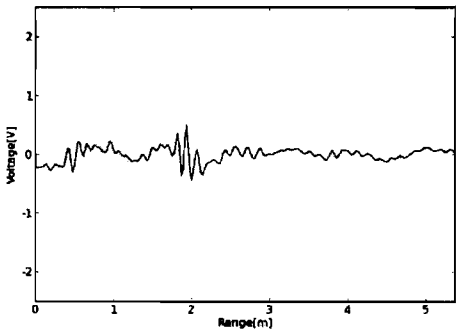

(c) Average waveform of raw target response

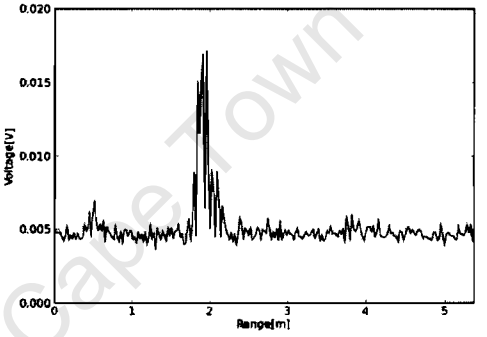

(d) Standard deviation of raw target response

Figure 7.15: The (a) (b) background profile, and (c) (d) the raw target response of a corner reflector that is placed 1.6 m away from the radar.

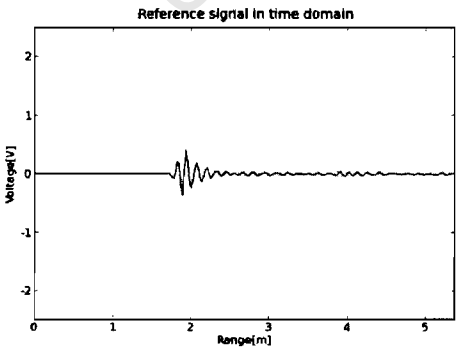

(a) Time domain

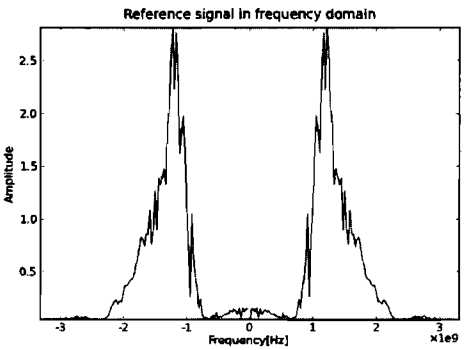

(b) Frequency domain

Figure 7.16: The reference signal, which is a target response of a corner reflector (see Table 7.1) that is placed at 1.6 m away from the radar.

Figure 7.15(d), is approximately 0.005 V. Hence the peak SNR of the target response in Figure 7.16(a) is

$$SNR \approx (\frac{0.4}{0.005})^2 \approx (80)^2 = 6400$$

Signal processing is performed in the following steps:

1. Subtracting the background profile recorded at the start of the experiment, from the raw target response.

2. The spectrum is converted to an 'analytic' form zeroing out the negative part of the spectrum.

3. The background-removed target response is them processed using an linear filter constructed from the reference signal (shown in Figure 7.16(a)).

Two types of linear filters were investigated: a matched filter (equivalent to correlation in the time domain), and an inverse filter. These were described in Section 3.4. Furthermore, a *rect* window is used to band-limit the filtered signal to a 1 GHz bandwidth, centred on 1.5 GHz, for both matched filtering and inverse filtering. Figure 7.17 and Figure 7.18 show the results from matched filtering and inverse filtering respectively. Since the signal is in analytic form, the time domain is a complex signal. Figure 7.17 and Figure 7.18 shows the magnitude of the waveform in (a), the positive frequency spectrum in (b), and standard deviation of the magnitude in (c).

It was noted that in Figure 7.17(c), the standard deviation has smaller peak than in Figure 7.15. It is suspected that the frequency component of the peak noise in Figure 7.15 is higher than 2 GHz. Hence, in the case of Figure 7.17(c), the high frequency noise is suppressed by the filtering.

Table 7.3 was constructed to compare the SNR performance before and after the signal processing was carried out. The results shown in Table 7.3, were extracted from Figure 7.16(a), 7.15(d), 7.17(a) and Figure 7.18(a). The table shows that with the usage of signal processing with a filtering technique, the peak SNR is improved from the unfiltered result. Of the three cases, the matched filtering give the best SNR performance (an improvement of 4.8 dB ($10log\frac{19600}{6400}$)). However, the matched filtered output signal has a wider pulse width and irregular shape compared to the inverse filtered signal, which is a $\frac{sin(x)}{x}$ function. This is due to the fact that the frequency spectrum of the inverse filtered signal (Figure 7.18(b)) is a *rect* function. When transformed into time domain, the inverse filtered signal has a $\frac{sin(x)}{x}$ shape, which has narrow mainlobe. The improvement in SNR for the inverse filter over unfiltered was only 1.5 dB ($10log\frac{9132}{6400}$). Based on the above mentioned observation, inverse filtering was chosen as the signal processing tool for the later experiment, as it provides a better peak SNR than the unfiltered method, and has narrower main-lobe than matched filtering, which is importance when ones tries to resolve

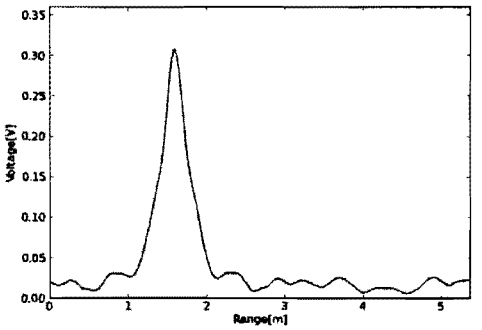

(a) Magnitude of the averaged waveform in time domain

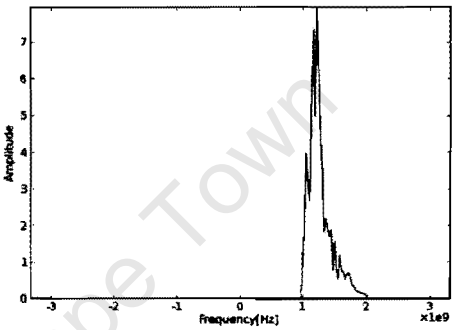

(b) Magnitude of the averaged waveform in frequency domain

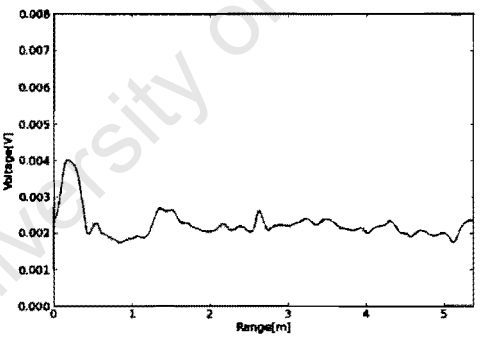

(c) Standard deviation

Figure 7.17: The results from matched filtering the background-removed target response.

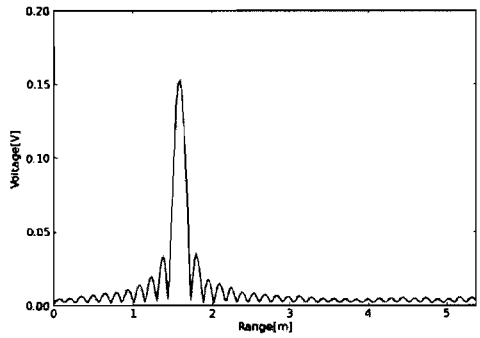

(a) Magnitude of the averaged waveform in time do-main

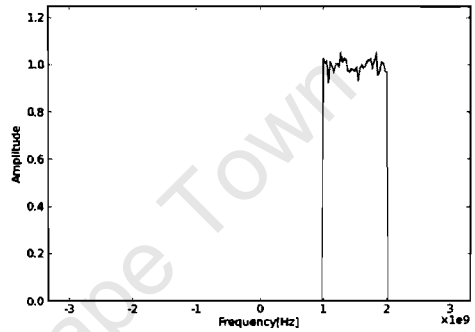

(b) Magnitude of the averaged waveform in frequency domain

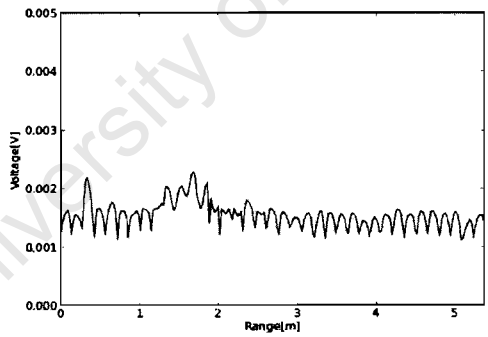

(c) Standard deviation

Figure 7.18: The results from inverse filtering the background-removed target response.

targets that are placed closely. The sidelobes shown in Figure 7.18(a) can be reduced by applying appropriate window function, such as Hanning window.

	$V_{rx(pk)}$	σ_{noise}	$\frac{V_{rx(pk)}}{\sigma_{noise}}$	Peak SNR
Unfiltered	0.4 V	0.005 V	80	6400
Matched filtering	0.3075 V	0.0022 V	140	19600
Inverse filtering	0.1529 V	0.0016 V	95	9132

Table 7.3: The SNR of the received signal when signal processing is used for the case of the corner reflector positioned at a range of 1.6 m.

7.3 Target Detection

The UWB radar is operated with the following steps during target detection:

1. System setup:
   The user must input the parameters of the radar system that are used in the experiment. The parameters include the number of receivers used in the experiment, spacing between the transducer and the data acquisition interval, i.e. the time between each caption.

2. Background clutter acquisition:
   The noise and the information about the stationary objects in the scene is captured at the start of the every experiment. 30 range profiles are recorded and averaged. The background profile is then stored and can be used to remove the background clutter from the raw target response.

3. Reference signal acquisition:
   The echo (signature) of the target is required for the signal filtering process. Since the echoes from different targets possess different shapes, therefore, range profiles are recorded for all objects shown in Table 7.1. 30 raw target response are recorded and averaged for each target. The averaged raw target response is then processed by subtracting the background clutter from the profile. The background-removed target response for each target is then stored.

4. Setup the frequency band of interest:
   The inverse filtering method is used by the GUI to process target responses. Since the inverse filter is only defined over a bandwidth, hence, the user is required to specify a frequency band for signal processing. The default value for the frequency band is set to between 1000 MHz and 2000 MHz.

This section is divided into two sub-sections. In the first sub-section, experiments are conducted for detecting objects using a single transmitter and a single receiver system. The

antennas used in this sub-section are the two bow-tie antenna shown in Figure 7.11. In the second sub-section, the experiments conducted are aimed at obtaining beamformed images and detecting objects through a brick wall. The radar system used in this sub-section consists of four Vivaldi PCB antennas, which were used as the receiving antennas, and a bow-tie antenna, which were used as the transmitting antenna.

The Vivaldi PCB antennas are held in place by a wooden base, which has slots cut-in to fit the antennas. Each slot is 5 cm apart. The receiver circuit board is connected directly to the antenna via a 50 Ω SMA connector. Figure 7.19 shows the UWB array radar setup. The distance between the adjacent PCB antennas is approximately 15 cm, which is limited by the spacing required for the receiver board when connected to the antenna.

Figure 7.19: UWB array system using four Vivaldi PCB antennas and a bow-tie antenna. The transmitter PCB is visible on the left side and the receiver PCB's are visible, attached to the four Vivaldi antennas. The ADC microcontroller and delay line PCB are not visible in this picture.

7.3.1 Maximum Range Detection For A Small (550x390 mm) Metal Grid

This experiment is aimed at determining the maximum range for detecting a small metal grid (550x390mm, shown in Table 7.1), without the need to increase the post-amplifier gain (the voltage gain of the post-amplifier is set to one). A background profile was captured at the start of the experiment. Then, a small metal grid was placed in front of the radar. Figure 7.20 shows the background profile and the raw target response of the small metal grid at 2 m away from the radar.

The small metal grid was then moved further away from the radar to different positions. The background profile was then used to subtract the background clutter from the raw target response. Figure 7.21 shows the background-removed target response of the metal grid, which was placed at the distance of 2 m, 3 m, 4 m and 5 m away from the radar.

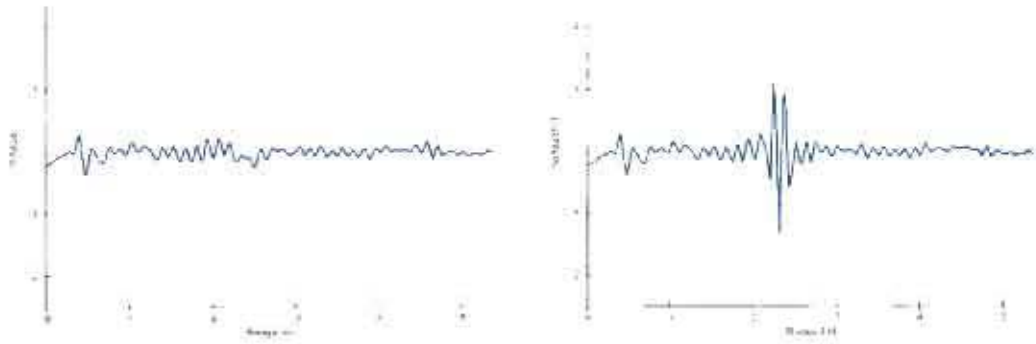

(a) Background profile (b) Raw target response

Figure 7.20: Profile shows the (a) background and the (b) raw target response of the small metal grid, which is positioned at 2 m away from the radar.

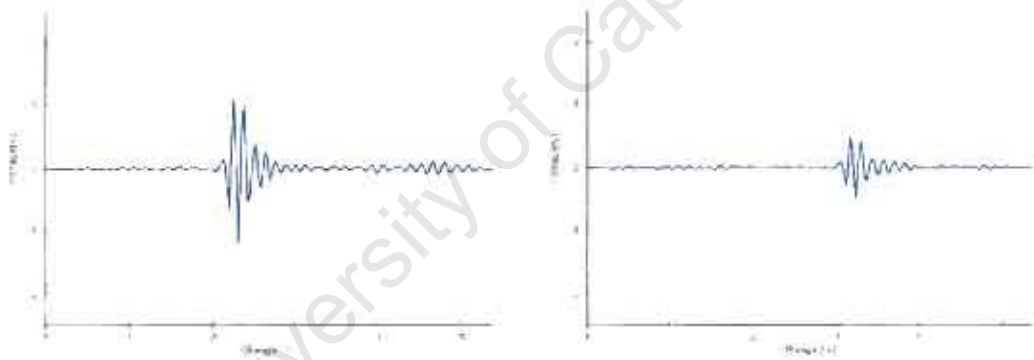

(a) Small metal grid at 2 metre (b) Small metal grid at 3 metre

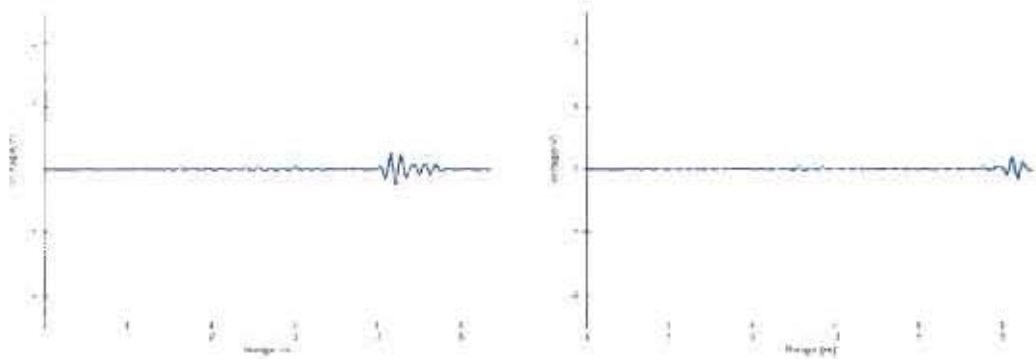

(c) Small metal grid at 4 metre (d) Small metal grid at 5 metre

Figure 7.21: Target response of a small metal grid, which is placed at various distance away from the target.

Figure 7.21 shows that the target response of a small metal grid is clearly visible at 5 m, without the need of signal processing or increase the gain of the post-amplifier.

7.3.2 Target response of various objects

In this experiment, the target responses of all the objects shown in Table 7.1 were acquired and investigated. Although target classification is not addressed in this thesis, these target responses, which contain the signatures of the targets, can be used for future research. Figure 7.22 shows the background-removed target responses of these objects, which were positioned at 2.2 m. The standard deviation of the noise, which was recorded in the previous experiment, is approximately 5 mV on the raw signal.

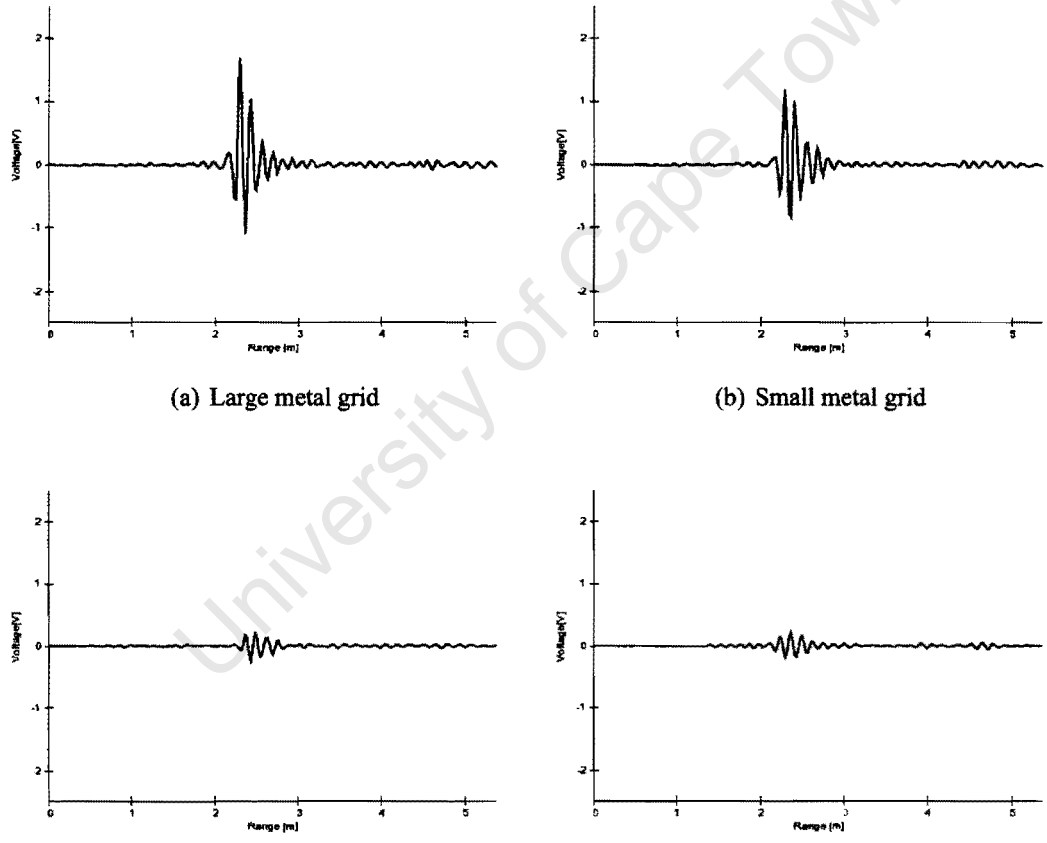

(a) Large metal grid

(b) Small metal grid

(c) Corner reflector

(d) Human

Figure 7.22: The target response of different targets. The target is located 2.2 metres away from the radar.

Figure 7.22 shows that the target response from the metal grids have similar shape. Furthermore, the target response of a human is more elongated. Table 7.4 shows the peak amplitude of the target responses. Assuming the peak voltage decays proportional to $\frac{1}{R^2}$, then $V_{\text{pk}}(R) = V_{\text{pk}}(2.2\,\text{m}) \times \frac{2.2^2}{R^2}$. The range R_{max} at which the SNR=1, i.e. $V_{\text{pk}}(R) = \sigma_n = 5\,\text{mV}$,

is

$$R_{\max(\mathrm{SNR}=1)} = \sqrt{V_{\mathrm{pk(2.2\ m)}}} \times \frac{2.2}{\sqrt{\sigma_n}}$$
$$= \sqrt{(V_{\mathrm{pk(2.2\ m)}}} \times 31.1\,\mathrm{m}$$

The range $R_{\max}$ at which the SNR=10 is

$$R_{\max(\mathrm{SNR}=10)} = \sqrt{V_{\mathrm{pk(2.2\ m)}}} \times \frac{2.2}{\sqrt{\sqrt{10}\sigma_n}}$$
$$= \sqrt{V_{\mathrm{pk(2.2\ m)}}} \times 17.5\,\mathrm{m}$$

Table 7.4 shows the calculated maximum range of detection for various objects, in the case of SNR=1 and SNR=10.

Target	V_{pk} of the target response (positioned at 2.2 m)	Maximum R (SNR=1)	Maximum R (SNR=10)
Large metal grid	1.62 V	39.6 m	22.3 m
Small metal grid	1.12 V	32.9 m	18.5 m
Corner reflector	0.21 V	14.3 m	8.0 m
Human	0.21 V	14.3 m	8.0 m

Table 7.4: Amplitude of the target response of different target and calculated range for $V(R) = \sigma_n$ (SNR=1) and $V(R) = \sqrt{10}\sigma_n$ (SNR=10).

7.3.3 Range Resolution Test

The range resolution experiment is conducted to verify the range resolution of the system when a 1 GHz bandwidth pulse is processed, occupying the spectrum range from 1 GHz to 2 GHz. Two targets, a small metal grid and a large metal grid, are located in the scene. The two targets are placed 15 cm apart, with the small metal grid closer to the radar. Figure 7.23 shows the background-removed target response of the two targets.

It is difficult to distinguish the two targets from the range profile shown in Figure 7.23. Hence, the target response is processed, using the inverse filtering method, with a pre-recorded reference signal used to form the inverse filter. The reference signal used in this experiment is the target response of the small metal grid. Figure 7.24 shows the inverse filtered target response. Two windowing functions, *rect* and the Hanning window, are used to band-limit the signal, which is required for the inverse filtering and shape the spectrum. Both windows are centred on 1.5 GHz and the bandwidth of the window is 1 GHz. The results shown in Figure 7.24 confirm that a radar system using a 1 GHz bandwidth band, has a range resolution of about 15 cm. One is able to visually resolve the two targets in Figure 7.24(a) but with undesirable sidelobes. The Hanning window suppresses the sidelobes, but broaden the mainlobe by 50%, causing the mainlobes to overlap.

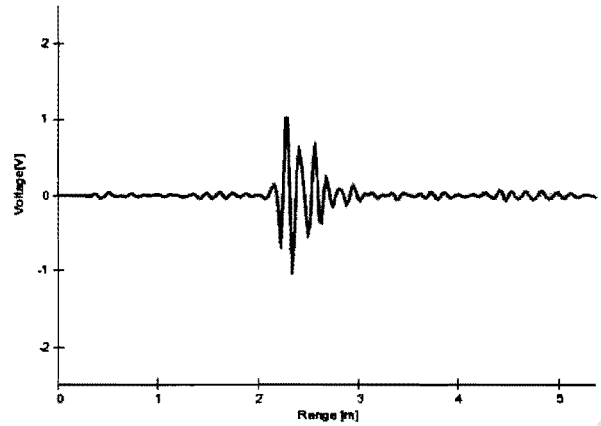

Figure 7.23: Target response of the two metal grid targets, being the small and larger grid reflector, spaced 15 cm apart in range.

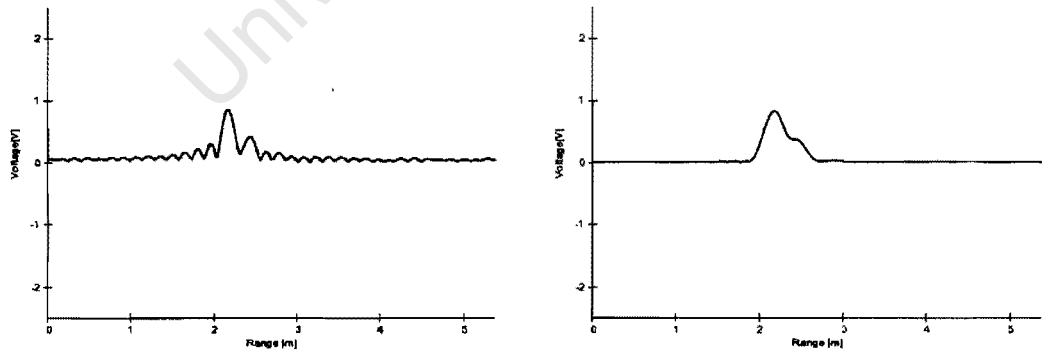

(a) (b)

Figure 7.24: The processed target response using inverse filtering with (a) *rect* window (b) Hanning window. Two targets are in the scene, placed 15 cm apart in range.

7.3.4 UWB Phased Array Beamforming

As mentioned in Section 7.3, four Vivaldi PCB antennas, spaced at 15 cm, are used as the receiving antennas in the UWB array radar. The background profiles and reference signal profiles were captured at the start of the experiment. Since each receiving antenna has a slightly different antenna characteristic, therefore, each antenna has a different set of background profile and reference signal profile. Thereafter, the two metal grid targets were placed in the scene. Figure 7.25 shows the position of the antennas and the targets. Target 1 and Target 2 labeled on Figure 7.25 are the small metal grid and the large metal grid respectively (descriptions in Table 7.1).

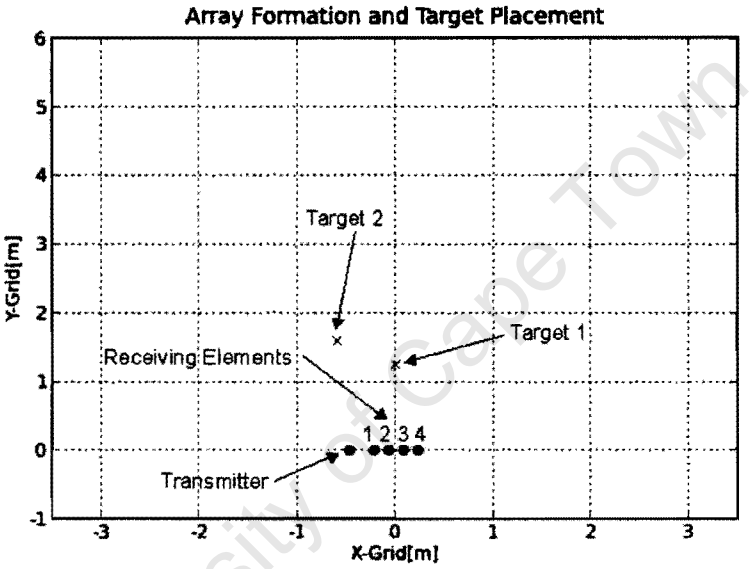

Figure 7.25: Position of the radar and the targets.

Inverse filtering with a Hanning window was used to process the raw target responses. Figure 7.26 shows the processed target responses for all the four receiving channels.

Thereafter, the filtered responses were basebanded, and beamforming process with Hanning aperture weighting was performed. Figure 7.27 compares the fan-beam images, which are generated using (a) simulation and (b) captured data set. Although the image is smeared due to the noise from the scene and receiving circuit and the limitations of the calibration process, the location of the targets shown in the image is close to the actual position of the target.

7.3.5 Through Wall Detection - Wall thickness

When an electromagnetic wave enters a medium of a different reflectivity, some of the signal is reflected. Hence, when a UWB signal travels through a wall, two reflections oc-

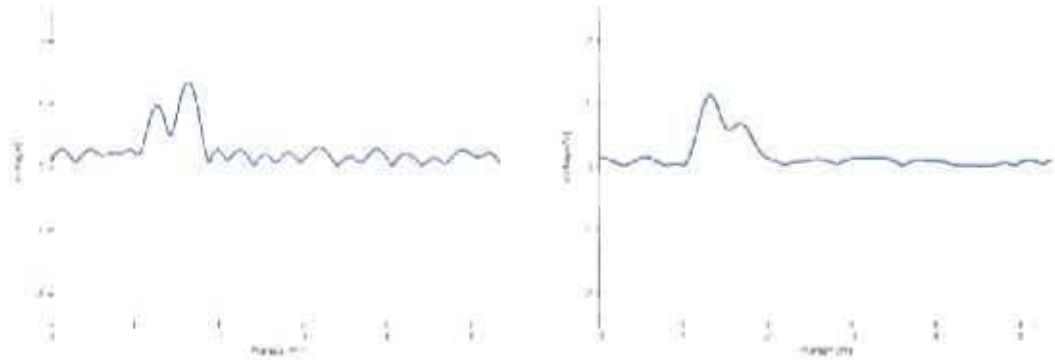

(a) Receiving channel 1 (b) Receiving channel 2

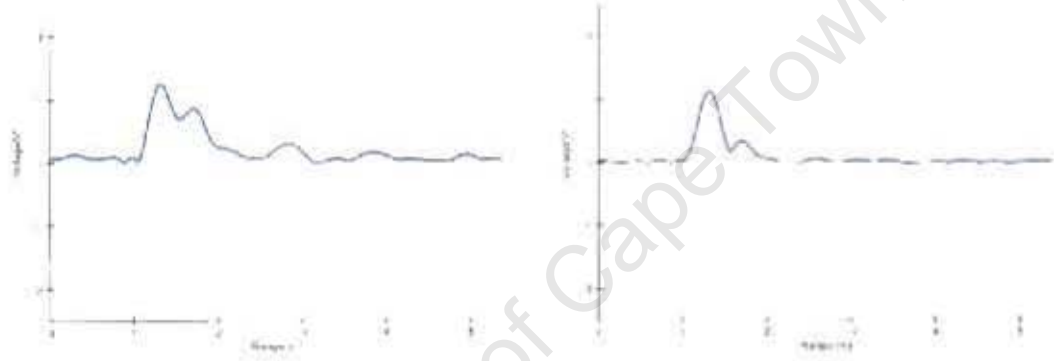

(c) Receiving channel 3 (d) Receiving channel 4

Figure 7.26: The processed target response of two metal grids, from all receiving channel. Inverse filtering with Hanning window is used for signal processing.

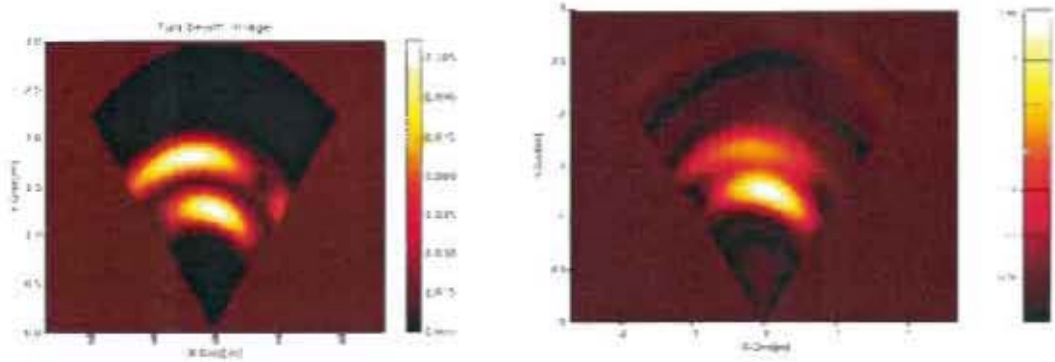

(a) Simulation (b) Actual data

Figure 7.27: Fan-beam image of the scene generated using (a) simulation (b) captured data set. The scene consists of two metal grid. Field of view – 84°.

cur; as the signal enters the wall and as the signal exits the wall. By finding the distance between the two reflection, the thickness of the wall can be obtained.

In the previous experiment, a background profile, which is free of the target, is captured at the start of the experiment. It is subtracted from the raw target response to reveal the target signature from background clutters. However, the target-under-detection for this experiment is the brick wall, which can not be remove from the scene. Hence, the raw target response of the brick wall, without removing the background clutter, is processed directly with a reference signal.

The reference signal used in this experiment is the echo of the small metal grid. The thickness of the wall under examination is approximately 31.5 cm. Figure 7.28 shows a picture of the brick wall and the processed target response of the wall, using inverse filtering with Hanning window.

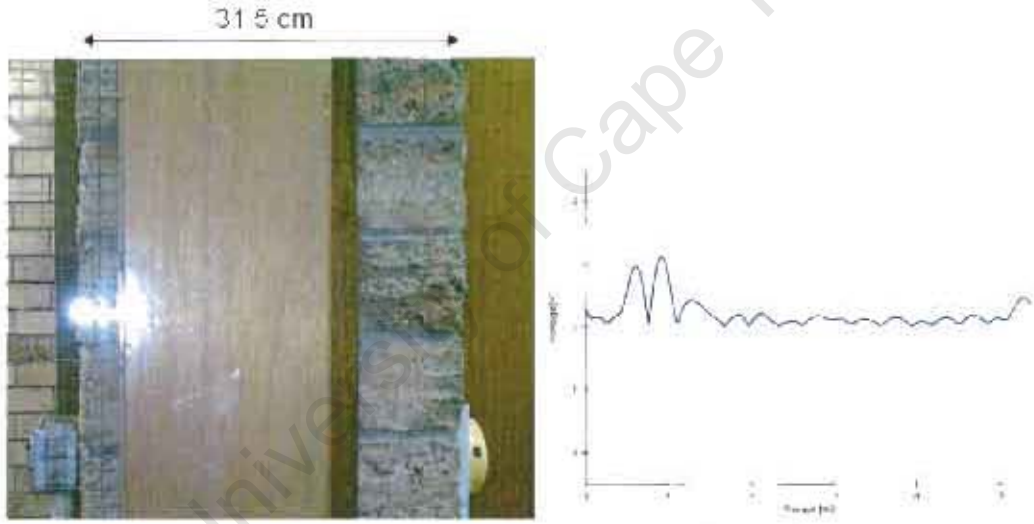

(a) (b) Hanning window

Figure 7.28: (a) Picture of the brick wall (b) processed target response of the wall. Inverse filtering with Hanning window is used to process the target response.

From Figure 7.28(b), the distance measured between the two peaks is ≈ 27 cm. The error between the measured and detected thickness of the wall, is due to the speed of propagation in brick wall being slower than the speed of propagation in the air. Presently, the distance-conversion algorithm used in this thesis, has not yet accounted for this transition.

7.3.6 Through Wall Detection - Moving Target

This experiment was conducted to illustrate an application of UWB radar involving motion detection.

The UWB array radar is placed in front of 10.5 cm thick wall, where a walking passage is behind the wall. A background profile of the scene was recorded at the start of the experiment. Afterwards, a person was asked to walk through the passage repeatedly, while the response of the scene was being recorded. Figure 7.29 illustrates the geometry and operation involved in this experiment.

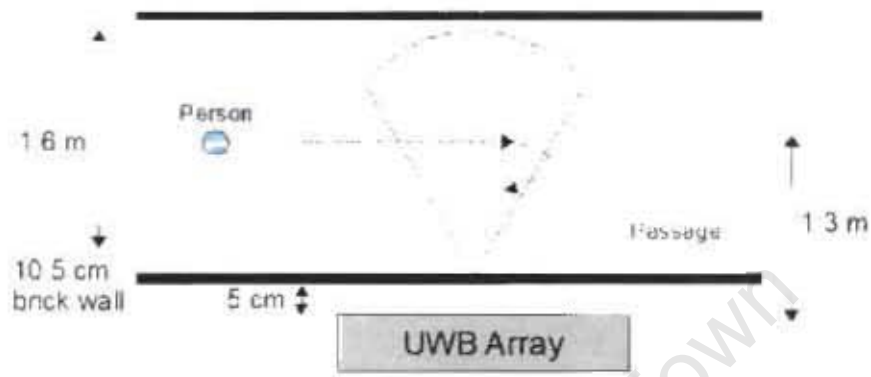

Figure 7.29: The setup of the experiment for detecting motion through a 10.5 cm brick wall.

The target response was obtained by removing the background clutter from the response of the scene recorded. Thereafter, signal processing using inverse filtering with Hanning window, and beamforming process with aperture weighting was used to process the target response. Figure 7.30 shows 5 consecutive fan-beam images that were recorded.

The scene is captured every two seconds. The main limitation in image update rate is due to the slow transmission rate between microcontroller and PC, via the serial port. Future improvement can be made using a USB port for data transmission. Figure 7.30 shows that the position and movements of a person can be detected. However, the speed of the system is not fast enough to demonstrate smooth motion sensing of a person walking.

Figure shows the same data but with background profile included. Three targets are identified in each frame:

- First brick wall, which is 5 cm away from the radar.
- A person walking forward, stopping and backward through the passage.
- Second brick wall, which is 1.7 m away from the radar.

Figure 7.31 shows that the reflection off a person and the reflection off the second brick wall is much smaller than the reflection off the first brick wall, hence in most cases of Figure 7.31, the actual target (the person) can not be clearly identified. This illustrates the importance of background-subtraction-algorithm used in this thesis.

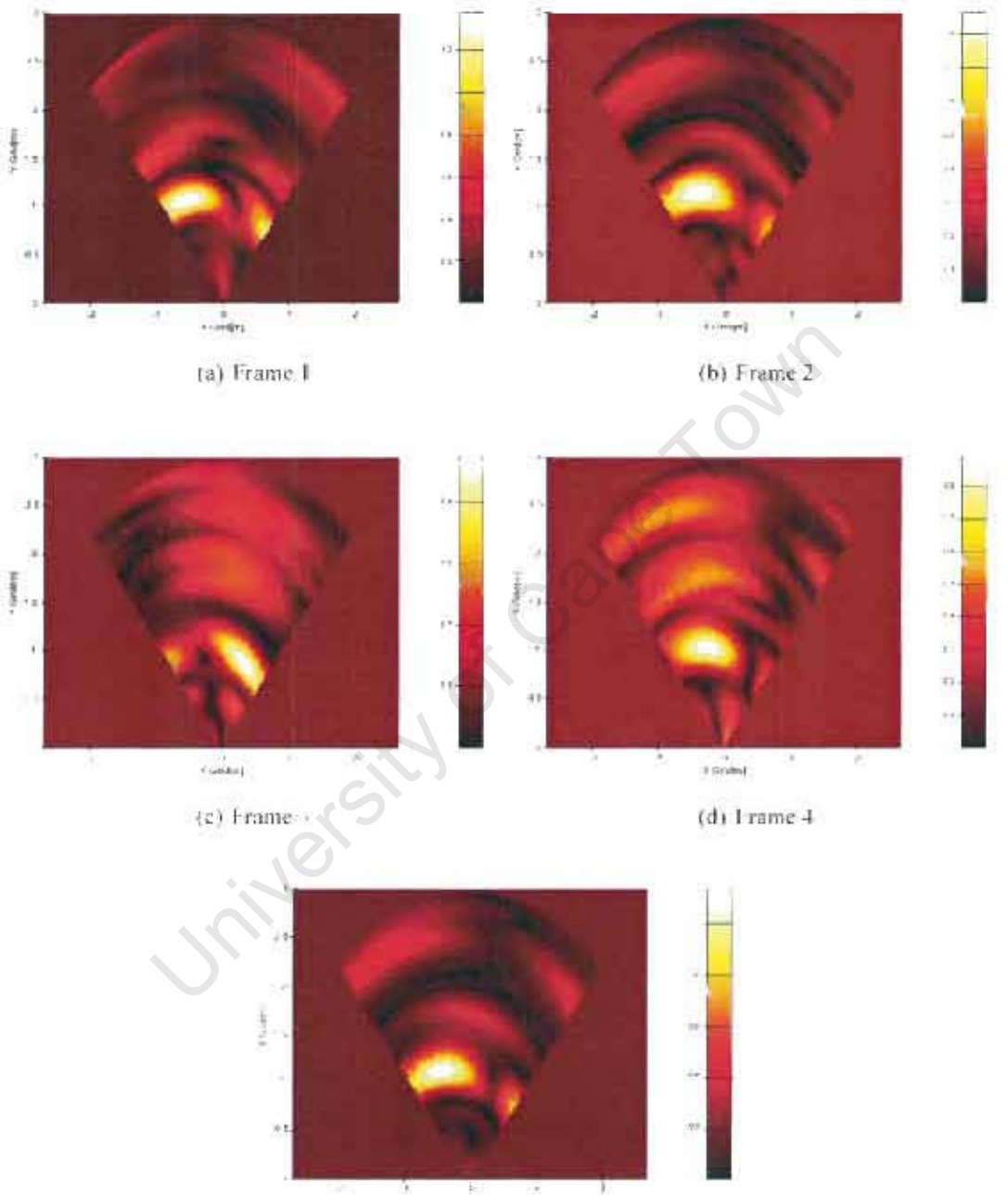

(a) Frame 1

(b) Frame 2

(c) Frame 3

(d) Frame 4

(e) Frame 5

Figure 7.30: Fan-beam images showing a person walking forward through a passage (frames 1, 2 and 3), then turning around in the middle of beam and walking back (frames 4 and 5). Field of view = 84°.

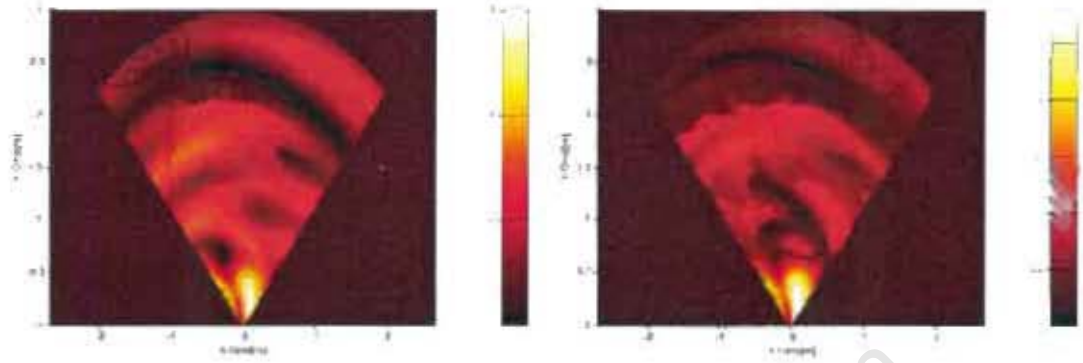

(a) Frame 1

(b) Frame 2

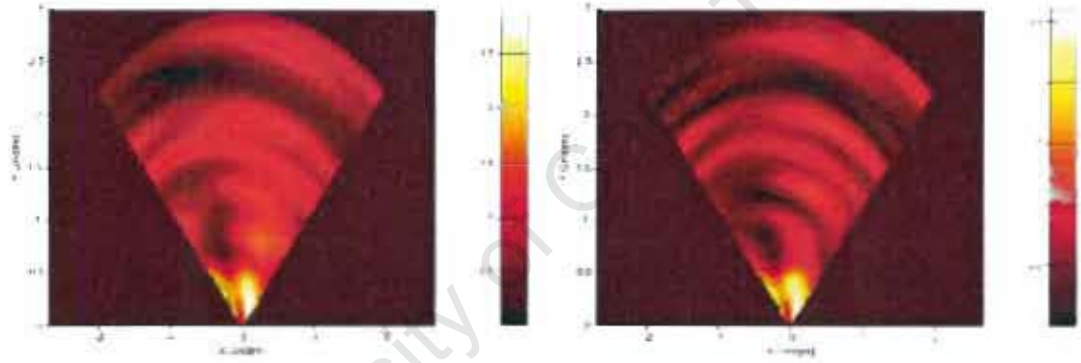

(c) Frame 3

(d) Frame 4

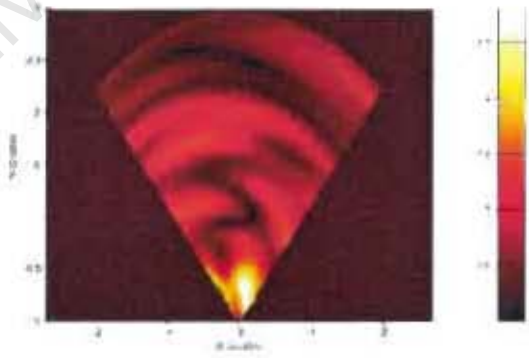

(e) Frame 5

Figure 7.31: Fan-beam images showing a person walking forward through a passage (frames 1, 2 and 3), then turning around in the middle of beam and walking back (frames 4 and 5). Background profile is not subtracted from the raw data. Field of view = 84°.

Chapter 8

Conclusions and Recommendations

A four channel phased array UWB radar was developed in this thesis. The multi-channel design made use of optimized sub-system circuits from previous works. Several improvements were made:

- The amplitude of the transmitted signal is increased by using an interdigital capacitor as the charging capacitor. The interdigital capacitor that was built in this thesis, has a better high frequency response than the chip capacitor, i.e. a flatter frequency response between 1 GHz and 4 GHz with 4.36 dB loss.
- The usage of a programmable delay line enhanced the delay control and accuracy used in the integrating sampler.
- Two analog switches are used to discharge the integrating capacitors that are used in the integrating sampler. The analog switches can discharge the integrating capacitor more efficiently than the previous design. This increases the maximum sweep rate of the system by a factor of 10.
- The usage of a low-noise microwave amplifier improved the SNR of the receiver system.
- The usage of a microcontroller integrated the radar system, which is now a step closer to a portable system.
- A GUI was developed using the Python programming language, which allows the user to control the system.

The system performance of the new UWB radar was measured and analyzed. From the results presented in Section 7.2, it can be concluded that the new system has an improved performance in terms of stability and SNR.

Experiments were conducted to illustrate the possible applications for UWB array radar. These include

- Detecting various targets with a different geometry.
- Detecting objects through an obstruction.
- Movement detection through an obstruction.

From the result shown in Section 7.3, it can be concluded that UWB radar system is ideal for detecting objects in short range applications, as the fine range resolution enables the radar to resolve closely-positioned targets. Furthermore, this UWB radar has shown its ability to perform through-wall imaging and detect a human walking behind a brick wall.

Overall, an integrated UWB phased radar has been developed. It can be used to detect objects and movement of metallic and non-metallic targets.

Future work should include

- Develop a battery power supply for the UWB radar system. This would allow a true portability of the radar system.
- Additional research into methods of increasing the pulse amplitude to further improve the detection of weak targets.
- A full investigation on UWB beamforming algorithm should conducted. This simulation should demonstrate the differences in beam pattern and grating lobe effects between a UWB and a narrow-band system.
- Develop a USB interface for higher data rate transmission between the microcontroller and computer.
- If a longer range profile is required, the potentiometer that is used to control the second post gain stage (TL092), can be replaced by a programmable potentiometer for a better user control.
- Investigating of the system in various applications (GPR, through-wall etc.)

Appendix A

Ultra-Wideband Circuit Schematics

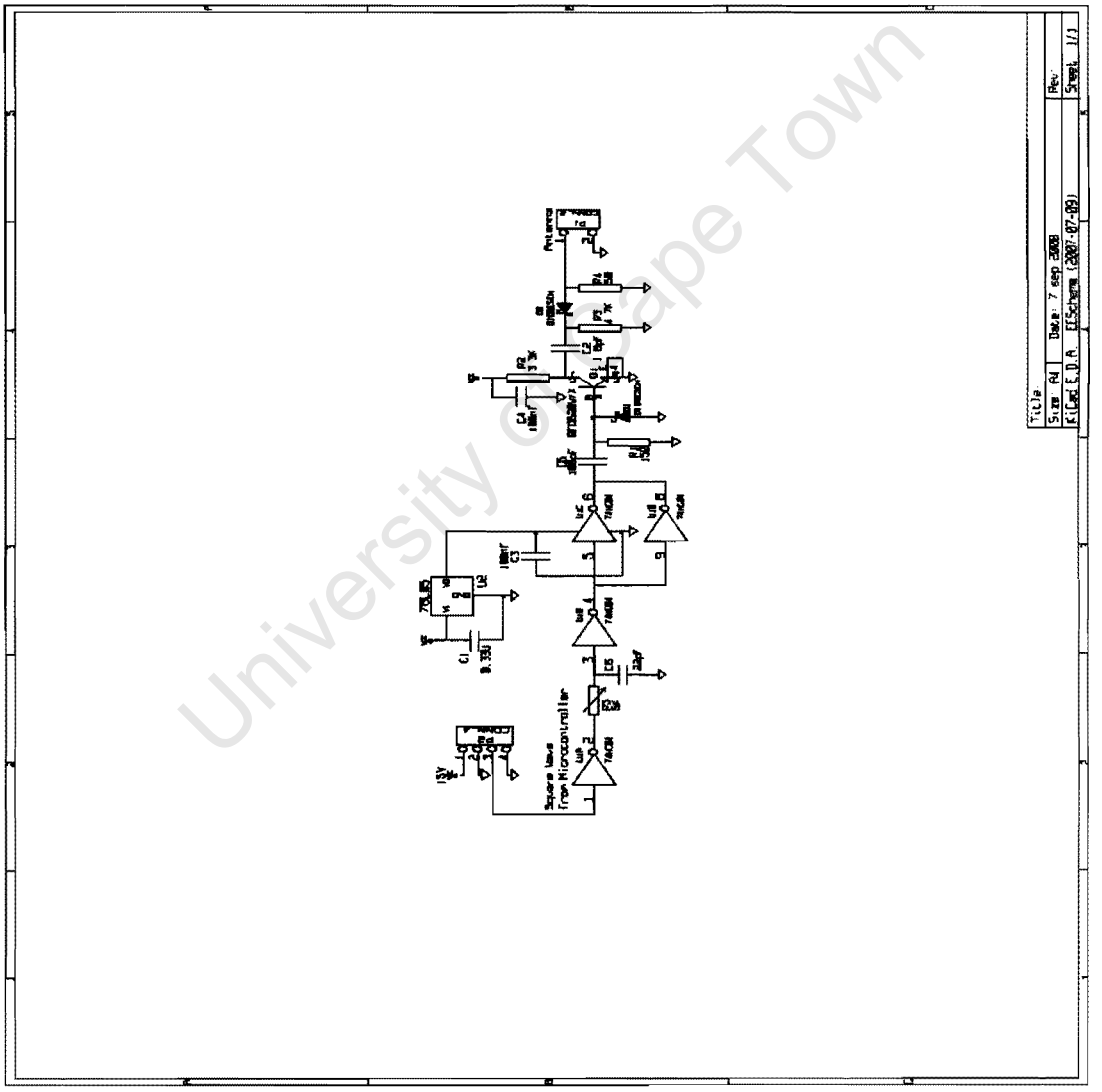

Figure A.1: UWB transmitter circuit diagram

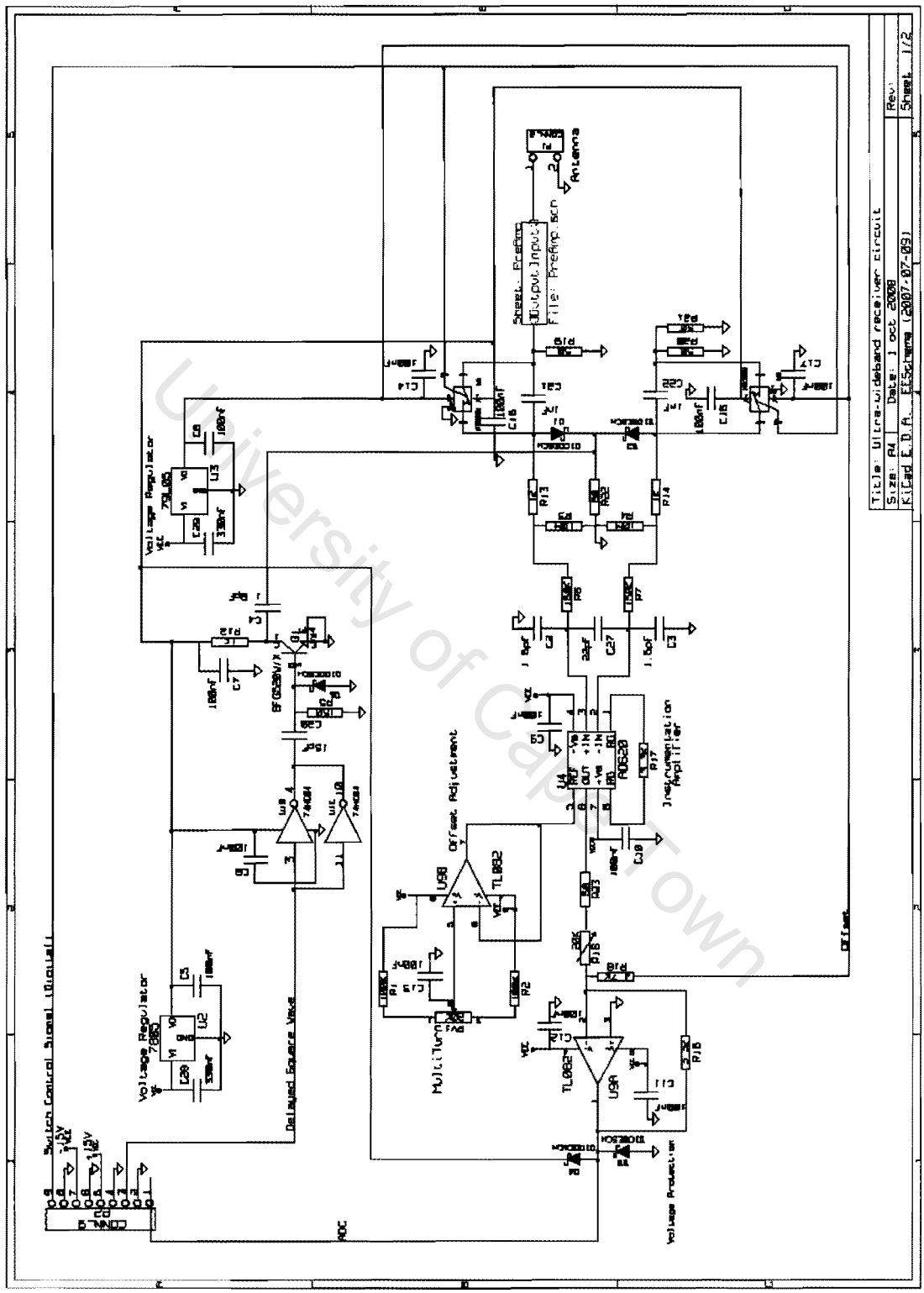

Figure A.2: UWB receiver circuit diagram

Appendix B

Nyquist Theorem for Bandpass Signal

The material presented in this appendix was adopted from [21].

Consider a signal of bandwidth B, centred on $f_0 = 1.5B$, as shown on the left of Figure B.1(a). If the signal is sampled at Nyquist sampling frequency for low-pass signal, which is $f_s = 2f_{max} = 2 \times (2B) = 4B$, the spectrum of the sampled signal will have some unoccupied space, as depicted on the right of Figure B.1(a).

In the case of reducing the sampling frequency to $f_s = 2B$, the result indicates that there is no overlap in the spectrum of the sampled signal, as depicted on the right of Figure B.1(b), which suggested that the original signal could be recovered from it.

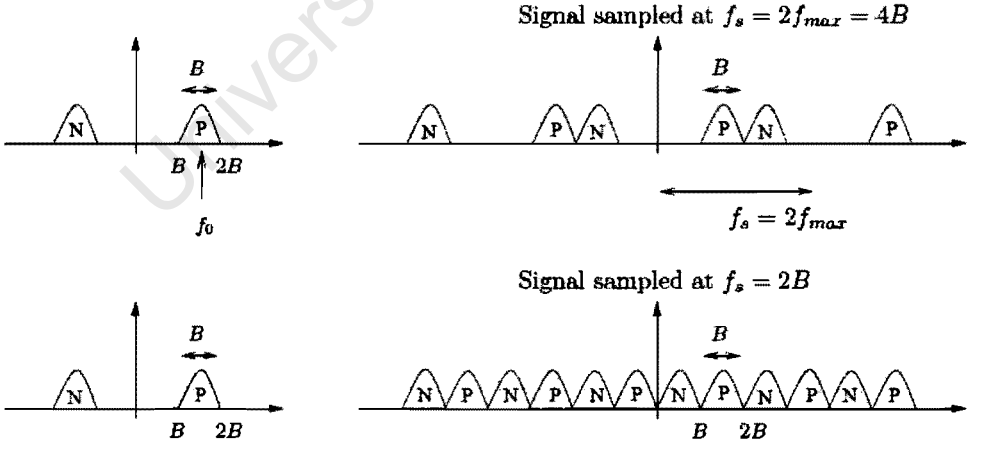

Figure B.1: Frequency domain representation of sampled bandpass signals [21].

However, if the centre frequency of the signal is reduced slightly, the sampling frequency of $fs = 2B$ will not be sufficient as the replicas of the signal spectrum will not fit the gaps without overlapping with each other. In this case, the signal is required to be sampled at twice of the highest frequency component of the signal.

For a bandlimited signal, the Nyquist sampling frequency $f_{Nyquist}$ changes as the lowest frequency component of the signal f_L increase. Figure B.2 shows the relationship between them (both expressed in terms of B).

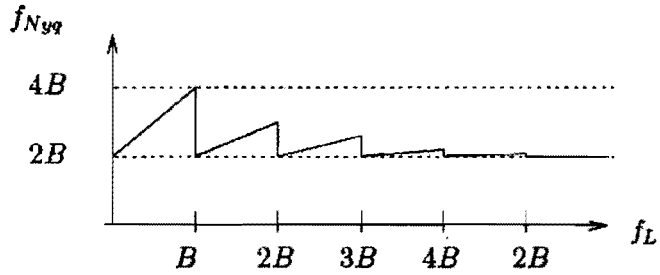

Figure B.2: Graph showing the relationship between the Nyquist frequency and the lowest frequency component of a bandlimited signal. Both frequency are expressed in terms of B, which is the bandwidth of the signal [21].

Bibliography

[1] DS1020 - Programmable 8-bit silicon delay line. Technical report, Maxim Integrated Products, Dallas Semiconductor.

[2] Federal Communication Commission (FCC) - Rules & Regulations. URL: http://www.fcc.gov/oet/info/rules/.

[3] PIC18F2423/2523/4423/4523 Data sheet - 28/40/44-pin, enhanced flash microcontrollers with 12-bit A/D and nanoWatt technology. Technical report, Microchip Technology Inc.

[4] Xaver 800 through wall vision. URL: http://www.camero-tech.com/xaver800.shtml.

[5] Prism 200 through-wall radar - covert intelligence at the touch of a button, November 2006.

[6] PDH – 4 bit & 6-bit HS Programmable Delay Lines. Technical report, ELMEC Technology, 2008.

[7] Application note : DS1020/DS1021 8 bit programmable delay lines. Technical report, Maxim Integrated Products, Dallas Semiconductor, March 2001.

[8] Chip inductors - 0603CS series (1608). Technical report, Coilcraft, Inc., March 2008.

[9] BAT81S - Small signal Schottky diodes. Technical report, Vishay, Rev. 1.7, February 2007.

[10] Suggested mounting configuration for DF782 case style, "mz" pin connection. Technical report, Mini-Circuits, Rev. D, November 2006.

[11] AD620 - Low cost low power instrumentation amplifier. Technical report, Analog Devices, Inc., Rev. G, January 2004.

[12] Gali-39+ - Surface mount monolithic amplifier. Technical report, Mini-Circuits, Rev. G, May 2007.

[13] Evaluation Board and Circuit. Technical report, Mini-Circuits, Rev: OR.

[14] MMIC Amplifier Gali-39+ - Typical Performace Curves. Technical report, Mini-Circuits, Rev. X1, August 2007.

[15] BFG520W/X - NPN 9 GHz wideband transistors. Technical report, NXP Semiconductors, Rev.04, November 2007.

[16] BFR91A - Silicon NPN planar RF transistor. Technical report, Vishay, Rev.3, January 1999.

[17] ADG601/ADG602 - 2 ohm, CMOS, +-5V/+5v SPST switches. Technical report, Analog Devices, Inc., Rev.C, March 2007.

[18] Interdigital capacitor design. Technical report, Agilent, September 2001.

[19] Ultra-Wideband / a Disruptive RF Technology? Technical report, Intel Research & Development, Version 1.3, September, 2002.

[20] A. Kilpela and J. Kostamovaara. A laser pulser for a tof laser radar. Technical report, University of Oulu.

[21] A.J. Wilkinson. Notes on radar/sonar signal processing: Fundamentals (ver: 0.83). University of Cape Town, 2008.

[22] A.J. Wilkinson. Signal processing and system design considerations for a broadband imaging sonar. Technical report, University of Cape Town, August 2007.

[23] A.J. Wilkinson, R.T. Lord and M.R. Inggs. Stepped-frequency processing by reconstruction of targetreflectivity spectrum. *COMSIG*, pages 101–104, 1998.

[24] B. Allen, M. Dohler, E.E. Okon, W.Q. Malik, A.K. Brown and D.J. Edwards, editor. *Ultra-wideband Antennas and Propagation for Communications, Radar and Imaging*. John Wiley & Sons, Ltd, 2007.

[25] B. Forssell. High-resolution radar (hrr) waveforms. In *Lecture Notes in Navigation Systems, Norwegian University of Science and Technology*. 2005.

[26] D. Barras, F. Ellinger and H. Jackel. A comparison between ultra-wideband and narrowband transceivers. Technical report, Laboratory for Electronics, Swiss Federal Institute of Technology (ETH), Zurich, Switzerland, November 2004.

[27] D.R. Wehner. *High-Resolution Radar, Second Edition*. Artech House, 1994.

[28] E. Engin, B. Ciftcioglu, M. Ozcan and I. Tekin. A high resolution ultrawideband wall penetrating radar. Technical report, Sabanci University, Turkey, 2007.

[29] E.J. Baranoski. Through-wall imaging: Historical perspective and future directions. *ScienceDirect*, January 2008.

[30] E.M. Staderini. Everything you always wanted to know about uwb radar... : a practical introduction to the ultra wideband technology. *Online Symposium for Electronics Engineers (OSEE)*, December 2001.

[31] F. Anderson, W. Christensen, L. Fullerton and B. Kortegaard. Ultra-wideband beamforming in sparse arrays. *IEE Proceedings-H*, 138, No 4, August 1991.

[32] F. Nekoogar. *Ultra-Wideband Communications: Fundamentals and Applications.* Prentice Hall, August 2005.

[33] M. Hussain. Principles of space - time array processing for ultrawide-band impulse radar and radio communications. *IEEE Transactions on Vehicular Technology*, 51, NO.3, May 2002.

[34] J. Silverstrim. Ieee ultra wideband presentation. Technical report, Innovative Wireless Technologies, October 2003.

[35] J. Warhus, S. Nelson, J. Mast and E. Johansson. Advanced ground-penetrating, imaging radar for bridge inspection. Technical report, Lawrence Livermore National Laboratory, September 1994.

[36] J.D. Taylor, editor. *Introduction to Ultra-Wideband Radar Systems.* CRC Press LLC, 1995.

[37] J.D. Taylor, editor. *Ultra-Wideband Radar Technology.* CRC Press LLC, 2001.

[38] L.N. Shuuya. Design and construction of a twin bowtie antenna for the frequency range 1-2 gigahertz. Thesis, University of Cape Town, October 2004.

[39] L.W. Fullerton. Full duplex ultrawide-band communication system and method. US Patent 6549567B1, April 2003.

[40] M. Ciattaglia and G. Marrocco. Time-domain beam shaping of pulsed arrays. Technical report, International Union of Radio Science, 2008.

[41] M. Ciattaglia and G. Marrocco. Investigation on antenna coupling in pulsed arrays. *IEEE Transactions on Antennas and Propagation*, 54, NO.3, March 2006.

[42] M. Tajima. DC block circuit and communication equipment. US Patent 20020105395 A1, August 2002.

[43] M.G.M. Hussain. Ultra-wideband impulse radar - an overview of the principles. *IEEE AES Systems Magazine*, September 1998.

[44] S. Phetla. Ultra wideband antennas for radar imaging applications. Thesis, University of Cape Town, November 2008.

[45] S. Ries and T. Kaiser. Ultra wideband impulse beamforming: It is a different world. *Signal Processing*, 86, 2006.

[46] S. Azevedo and T.E. McEwan. Micropower impulse radar. *Science & Technology Review*, January / February 1996.

[47] S.P. Lohmeier, R. Rajaraman and V.C. Ramasami. Development of an ultra-wideband radar system for vehicle detection at railway crossings. *IGARSS 2002 Digest*, June 2002.

[48] Spectrum Software, URL: http://www.spectrum-soft.com. *Micro-Cap 9 Evaluation Version*.

[49] T. Tibebe. Simulation study of ultra-wideband communication systems. *London Communications Symposium*, 2001.

[50] T.E. McEwan. Ultra-short pulse generator. US Patent 5274271, December 1993.

[51] T.E. McEwan. Ultra-wideband radar motion sensor. US Patent 5361070, November 1994.

[52] T.E. McEwan. Ultra-wideband receiver. US Patent 5345471, September 1994.

[53] T.W. Barrett. History of ultra wideband communications and radar: Part II, uwb radars and sensors. *Microwave Journal*, February 2001.

[54] T.W. Barrett. History of ultra wideband communications and radar: Part I, uwb communications. *Microwave Journal*, January 2001.

[55] V. Lakkundi. Ultra wideband communications: History, evolution and emergence. *Acta Polytechnica*, 46, 2006.

[56] W. Nel, J. Tait, R. Lord and A. Wilkinson. The use of a frequency domain stepped frequency technique to obtain high range resolution on the csir x-band sar system. *Proceeding 6th IEEE AFRICON, Africon Conference in Africa, 2002*, 1:327–332, 2002.

[57] Y-M A. Chang. A micropower ultra-wideband radar profiling system. Master's thesis, University of Cape Town, August 2006.